INFORMATION TO USERS

This manuscript has been reproduced from the microfilm master. UMI films the text directly from the original or copy submitted. Thus, some thesis and dissertation copies are in typewriter face, while others may be from any type of computer printer.

The quality of this reproduction is dependent upon the quality of the copy submitted. Broken or indistinct print, colored or poor quality illustrations and photographs, print bleedthrough, substandard margins, and improper alignment can adversely affect reproduction.

In the unlikely event that the author did not send UMI a complete manuscript and there are missing pages, these will be noted. Also, if unauthorized copyright material had to be removed, a note will indicate the deletion.

Oversize materials (e.g., maps, drawings, charts) are reproduced by sectioning the original, beginning at the upper left-hand corner and continuing from left to right in equal sections with small overlaps.

Separation of static and dynamic disorder in magnetic materials

by

Johan van Lierop

Department of Physics

McGill University

Montréal, Québec

December, 2000

A thesis submitted to the Faculty of Graduate Studies and Research in partial
fulfillment of the requirements for the degree of Doctor of Philosophy

The author has granted a non-exclusive licence allowing the National Library of Canada to reproduce, loan, distribute or sell copies of this thesis in microform, paper or electronic formats.

The author retains ownership of the copyright in this thesis. Neither the thesis nor substantial extracts from it may be printed or otherwise reproduced without the author's permission.

L'auteur a accordé une licence non exclusive permettant à la Bibliothèque nationale du Canada de reproduire, prêter, distribuer ou vendre des copies de cette thèse sous la forme de microfiche/film, de reproduction sur papier ou sur format électronique.

L'auteur conserve la propriété du droit d'auteur qui protège cette thèse. Ni la thèse ni des extraits substantiels de celle-ci ne doivent être imprimés ou autrement reproduits sans son autorisation.

0-612-70171-9

Canada

voor mijn geliefde Julia

Abstract

Conventional transmission Mössbauer, selective excitation double Mössbauer (SEDM), and zero-field muon spin relaxation (ZF-μSR) spectroscopy were used to identify static and dynamic magnetic disorder. With the construction of an efficient SEDM spectrometer, a consistent description of static magnetic disorder in an amorphous alloy (a-$Fe_{80}B_{20}$) was developed using transmission Mössbauer and SEDM spectroscopy. Both methods measure the effects of the random static distribution of local magnetic environments around the Mössbauer nuclei. Magnetic fine particle systems (Fe_3O_4 ferrofluids, polysaccharide iron complex) were examined using transmission Mössbauer spectroscopy, and a model was developed that describes the entire range of dynamic magnetic behavior, from blocked moments on towards collective excitations and superparamagnetic moments. SEDM has measured $180°$ moment flips in the ferrofluids, determining a model independent relaxation rate of superparamagnetic moments. With the spectral signatures of static and dynamic magnetic phenomena identified, SEDM spectroscopy has been used to unambiguously verify the existence (a-$Fe_{92}Zr_8$) and absence ($Fe_{65}Ni_{35}$) of magnetic relaxation in chemically disordered alloys. Additionally, the static and dynamic disorder in a magnetic fine particle system (a polysaccharide iron complex) and a frustrated magnet system (a-$Fe_x Zr_{100-x}$), have been measured with ZF-μSR spectroscopy. The effects of collective excitations have been independently verified with ZF-μSR and moment fluctuation rates are in agreement with transmission Mössbauer spectra fit results. Two magnetic transitions have been identified with ZF-μSR in the a-$Fe_x Zr_{100-x}$ system, one at T_C and another at T_{xy} corresponding to transverse spin freezing, in both static and fluctuating magnetic components of μSR spectra. SEDM has been used to verify the existence of a fluctuation peak at T_{xy}, and the time-dependent hyperfine interactions due to transverse spin freezing have been identified, where SEDM fluctuation rates are in agreement with ZF-μSR results.

Résumé

La transmission conventionnelle Mössbauer, double sélectif Mössbauer (SEDM) d'excitation, et spectroscopie de la relaxation de rotation de muon de zéro-zone (ZF-μSR) ont été employées pour identifier le désordre magnétique statique et dynamique. Avec la construction d'un spectromètre efficace de SEDM, une description cohérente de désordre magnétique statique dans un alliage amorphe (a-$Fe_{80}B_{20}$) a été développée en utilisant la transmission Mössbauer et la spectroscopie de SEDM. Les deux méthodes mesurent les effets de la distribution statique aléatoire des environnements magnétiques locaux autour des noyaux de Mössbauer . On a développé des systémes magnétiques de particules fines (ferrofluids de Fe_3O_4, complexe de fer de polysaccharide) ont été examinés en utilisant la spectroscopie de la transmission Mössbauer , et un modèle qui décrit l'intervalle entier du comportement magnétique dynamique, des moments bloqués en fonction vers des excitations collectives et des moments superparamagnetic. SEDM a mesuré des chiquenaudes du moment 180° dans les ferrofluids, déterminant une cadence indépendante modèle de relaxation des moments superparamagnetic. Avec les signatures spectrales des phénomènes magnétiques statiques et dynamiques identifiés, la spectroscopie de SEDM a été employée pour vérifier clairement l'existence (a-$Fe_{92}Zr_8$) et l'absence ($Fe_{65}Ni_{35}$) de la relaxation magnétique en alliages chimiquement désordonnés. Supplémentaire, le désordre statique et dynamique dans un système magnétique de particules fines (un complexe de fer de polysaccharide) et un systéme frustré d'aimant (a-Fe_xZr_{100-x}), ont été mesurés avec la spectroscopie de ZF-μSR. Les effets des excitations collectives ont été indépendamment vérifiés avec ZF-μSR et les cadences de fluctuation de moment sont en accord avec des résultats adaptés par spectres de la transmission Mössbauer . Deux transitions magnétiques ont été identifiées avec ZF-μSR dans le système d'a-Fe_xZr_{100-x}, un à T_C et des autres à T_{xy} correspondant à la rotation transversale gelant, dans les composants magnétiques statiques et flottants des spectres de μsr. SEDM a été employé pour vérifier l'existence d'une crête de fluctuation à T_{xy}, et les interactions hyperfines dépendant du temps dues à la congélation transversale de

rotation ont été identifiées, où les cadences de fluctuation de SEDM sont en accord avec des résultats de ZF-μSR.

Acknowledgments

First and foremost, I would like to thank my supervisor, Dr. Dominic Ryan, for his patience (it's a relative thing), guidance, and support over the past several years. I feel very lucky to have had him as a mentor. He has shown me how science should be done.

Dr. Seán Cadogan from the School of Physics at the University of New South Wales is a friend and colleague who has been a great help in improving my understanding of magnetism. His presence has made working an enjoyable and stimulating experience.

Dr. Alex Kuprin was a great help when building and testing the conversion electron detectors used for my experiments. His work in designing and building the scattering enclosure for the closed cycle refrigeration system was invaluable.

I also appreciate the help and advice that Dr. Zaven Altonian has given over the years. I would like to thank Dr. Nick deTakacsy and Dr. Martin Grant for helping me understand the effects of magnetic relaxation and frustrated magnets on Mössbauer spectra. Dr. Mark Sutton has helped improve my understanding of data fitting and numerial analysis. Dr. Syd Kreitzman and Donald Arseneau have been great to work with at TRIUMF.

Dr. Juan Gallego and Paul Mercure deserve kudos for keeping the network working and helping me solve my programming difficulties.

Frank van Gils was a great help during the design of new instruments and various technical emergencies during time in the Physics Department. Machinists Steve Kecani and Michel Champagne were kind enough to part with some of their experience during my endeavors in the shop.

For assistance in dealing with all the administrative work, I thank Lynda Corkham, Paula Domingues, Diane Koziol, and Joanne Longo. Michel Beauchamp was a great laboratory technician to work with when I taught the undergraduate laboratories.

Friends that I have made at McGill who have kept me sane, and who I have enjoyed

Contents

List of Figures

xi

List of Tables

Chapter 1

Introduction

There are two types of magnetic disorder. Static disorder is present when there is a distribution of unfluctuating magnetic moments in a material. Dynamic disorder occurs when the magnetism of a material varies during the measuring time of an experimental technique.

Substances which exhibit static magnetic disorder and their uses are Fe-Si-B amorphous alloys in transformer cores, and Fe-B based amorphous alloys for passive alarm systems. To properly characterize static magnetic disorder in a material, it is necessary to use an experimental method, such as transmission Mössbauer spectroscopy, which is sensitive to the local environment around the magnetic atoms. Static disorder affects a transmission Mössbauer spectrum in several striking ways. α-Fe is an archetypal metal with the atoms in a bcc lattice. Examining a transmission Mössbauer spectrum of α-Fe in Fig. 1.1, a single linewidth and magnetic hyperfine field describes the spectrum. No static disorder is present in this material. A transmission Mössbauer spectrum of the amorphous alloy a-$Fe_{80}B_{20}$ (a typical material with static disorder) in Fig. 1.2, shows that the sextet can no longer be described by a single linewidth, and the overall lineshape has been significantly altered. A distribution of magnetic fields is necessary to describe this spectrum. The effects of static disorder on the spectrum are quite pronounced.

Dynamic disorder occurs in single domain fine particle systems, such as ferrofluids,

1
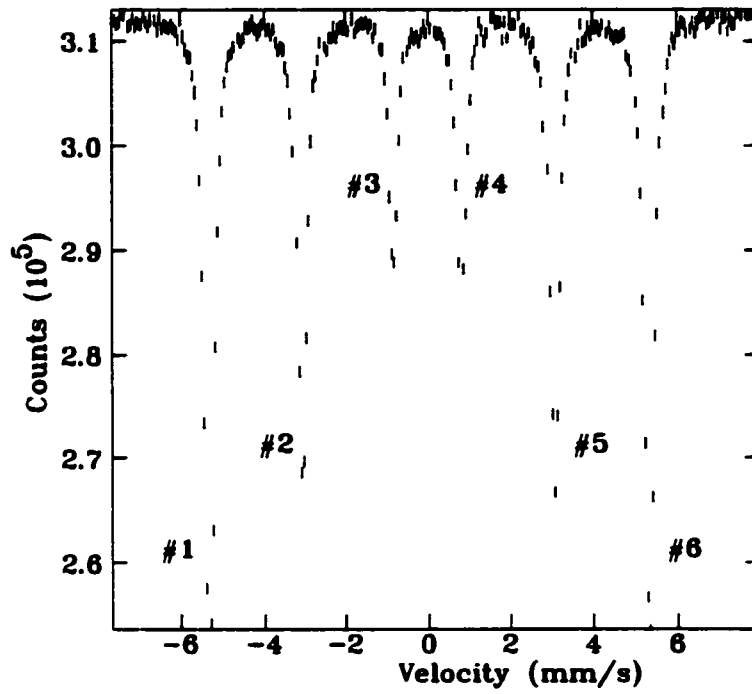
Figure 1.1: Transmission Mössbauer spectrum of α-Fe.
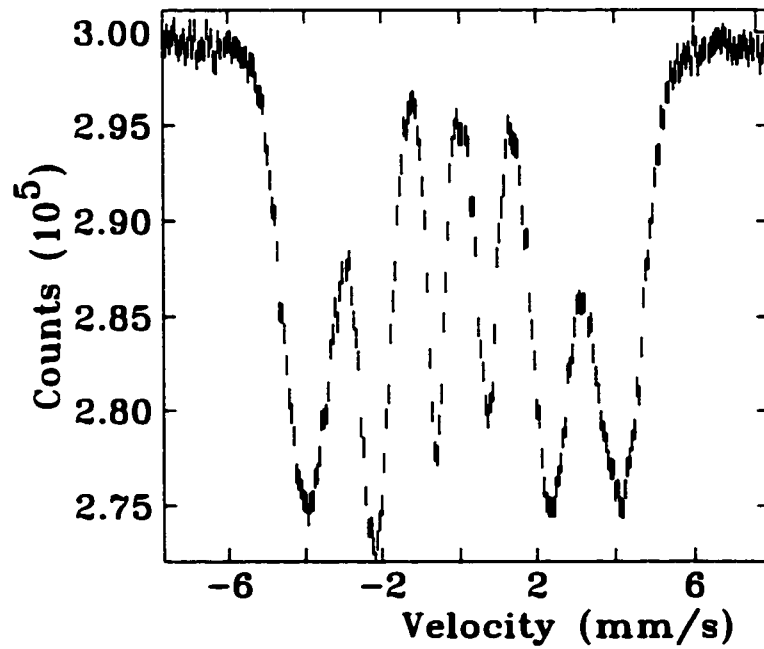
Figure 1.2: Transmission Mössbauer spectrum of a-$Fe_{80}B_{20}$. Note the difference in lineshape (e.g. broader lines) when compared with α-Fe in Fig. 1.1.

multi-layer and patterned thin films, and is a fundamental property of all magnetic recording media. A single domain particle is an ideal system with time-dependent magnetism. The magnetization of a single domain particle varies with increasing temperature. At low temperatures, the moment is fixed along its easy axis, in a blocked state. The moment will remain blocked until the thermal energy is great enough to allow it to oscillate around its easy axis. These oscillations, called collective excitations, occur until the thermal energy increases in magnitude and the onset of $180°$ moment flips is possible. At and above this temperature, the particle is superparamagnetic.

In a real magnetic fine particle sample (Fig. 1.3) there is a distribution of particle
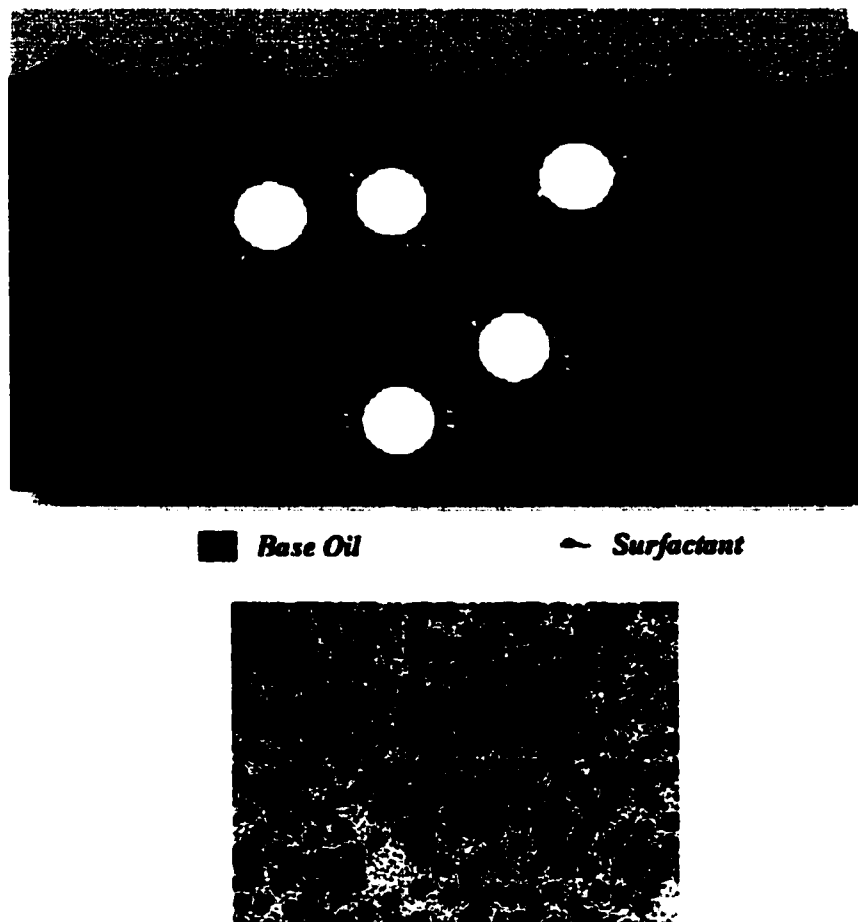
Figure 1.3: Schematic view of a Fe_3O_4 ferrofluid at room temperature (top) and a TEM of a ferrofluid with an average particle size of 10 nm (bottom)[34].

3
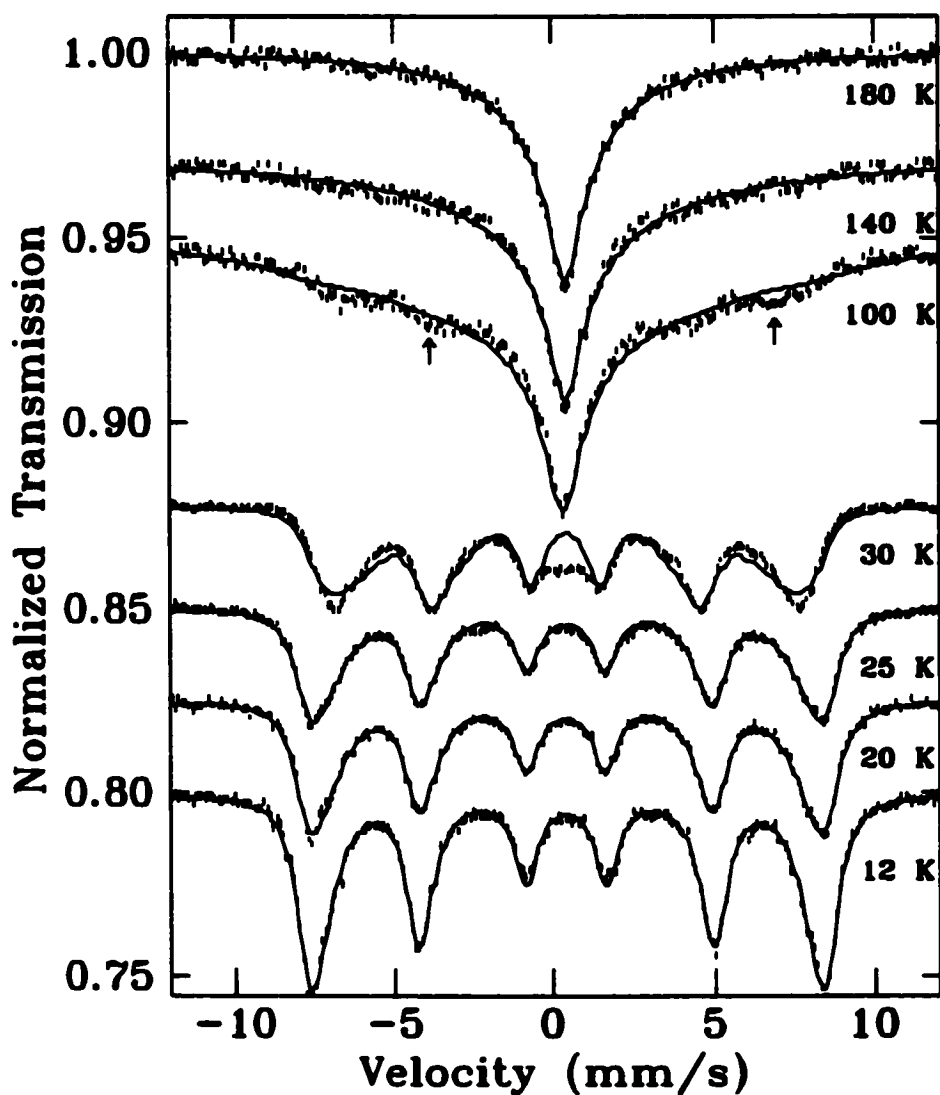
Figure 1.4: Fits to the 4.5 nm Fe_3O_4 ferrofluid using Mørup's collective excitation description for low temperature spectra and a two-level relaxation model for the high temperature spectra. These models clearly fail to predict the lineshape of the intermediate temperature spectra.

sizes. At the lowest temperatures, when all moments are blocked, Mössbauer spectra can be described with static hyperfine fields. With an increase in temperature, as moments unblock and collective excitations begin, spectra exhibit an asymmetric lineshape which becomes more pronounced as the temperature increases. This phenomena has been modeled by Mørup[1], and results in a correction to the hyperfine field which, when combined with a particle size distribution, properly describes the asymmetric

lineshape observed in the Mössbauer spectrum (bottom of Fig. 1.4). At high temperatures where the magnetic moments are all superparamagnetic, Mössbauer spectra are generally modeled using stochastic two-level lineshape formalisms, such as the one by Blume and Tjon[2]. Two-level models describe the 0° and 180° moment orientations along the easy axis and predict the spectral collapse arising from the time averaged hyperfine field (top of Fig. 1.4).

At intermediate temperatures, where there is enough thermal energy for collective excitations and moment flips to occur, the models for collective excitations and spin flipping cannot correctly predict Mössbauer spectral lineshapes (100 K and 30 K spectra in Fig. 1.4). At any given intermediate temperature, moments associated with the largest particles will be blocked, intermediate sized particle moments will experience collective excitations, while the smallest particle moments will be superparamagnetic. The blocking temperature, T_B[3], which defines the transition from collective excitations to superparamagnetism, is difficult to determine with Mössbauer spectra unless a model that can describe spectra over the entire range of temperatures is used. A further complication arises from interparticle interactions[4], due to the inevitable difficulty in controlling particle dispersal. Usually of a dipolar nature, interparticle interactions will affect the energy necessary for moment flips and change T_B.

Lineshape modeling of transmission Mössbauer spectra for the complete range of temperatures has had limited success. Only in the simplest case of a very dilute fine particle system with a narrow distribution of particle sizes, where interparticle interactions can be considered absent[4], have spectra been properly modeled. At intermediate temperatures, spectra consist of a clear magnetic sextet with collapsed components which can be fitted with a linear combination of Mørup's collective excitation model and a two-level relaxation model[5]. This procedure yields appropriate values for T_B and the anisotropy energy. When a sample contains a broad distribution of particle sizes, the above lineshape description fails. Attempts to model such spectra generally consist of combining a distribution of static hyperfine fields to describe the sextet component and a two-level relaxation model to fit the collapsed

5

component. This is incorrect, as the sextet component of spectra contains information about magnetic relaxation. Furthermore, effects from phenomena such as particle anisotropy and different particle sizes are not accounted for. Failure of these models to correctly describe spectra is exhibited by the necessity for linewidth increases with temperature[6, 7, 8], an incorrect approach as it masks a characteristic mark of magnetic relaxation. T_B cannot be correctly predicted and the typical equal area definition for T_B, which consists of determining the temperature at which spectra appear composed of equal areas of static and collapsed components, is used[3]. This definition of T_B is physically incorrect as it does not describe the magnetic moment behavior in the sample, and cannot incorporate the effects of either the particle size distributions or interparticle interactions. A more robust definition of T_B is necessary for Mössbauer spectra to permit comparisons with different measuring techniques that exhibit different sensitivities to the particle size distribution. For example, magnetization is dominated by the response of the larger, slower particles, while the majority of the susceptibility comes from particles close to their blocking temperature.

Identifying and modeling the magnetism in a fine particle system is reasonably straightforward as the dominant interaction are time-dependent. However, some materials exhibit magnetism which can be described equally well by physical models based upon static or dynamic effects. An example of such a metal is the Invar alloy, $Fe_{65}Ni_{35}$. The Fe-Ni compounds have a long history in materials science, and have gained the title, "The Invar Problem"[9]. Towards the end of the nineteenth century, while looking for a material which would make a better standard for the meter, Guillaume[10] discovered that $Fe_{65}Ni_{35}$ showed essentially no thermal expansion at room temperature, winning him the 1920 Nobel prize in physics. Understanding this property of very low thermal expansion in the Fe-Ni based alloys has attracted many researchers and resulted in various uses. Typical applications are microwave wave-guide tubes and resonance cavities, watch springs, pendulums and balances, and most impressive, the Invar membrane used to line the tanks in ships that carry oil and natural gas[9].

6
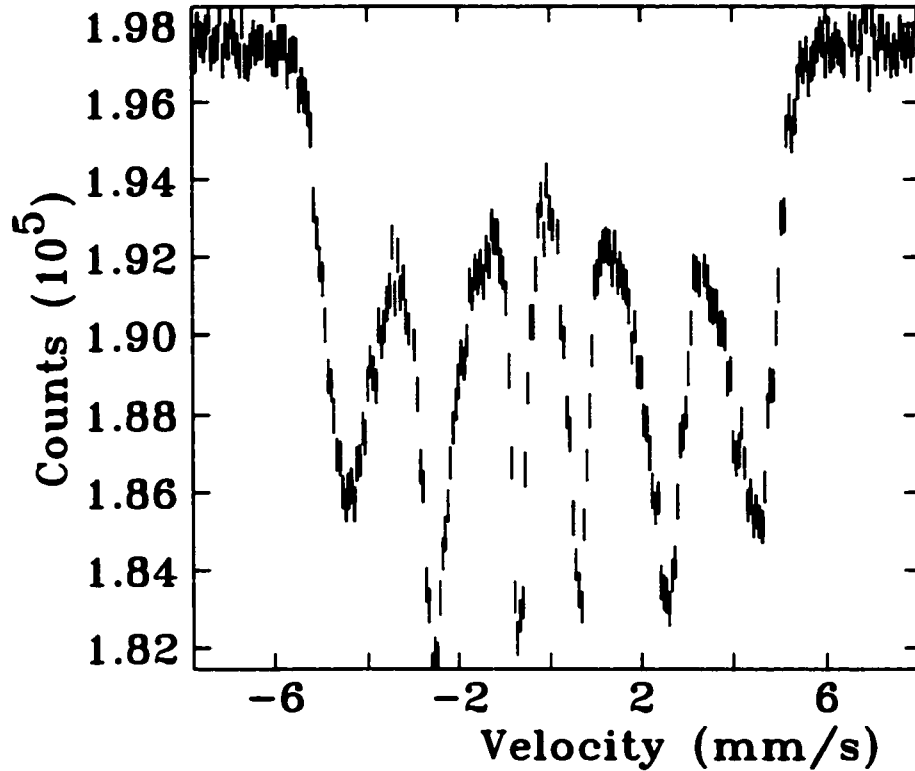
Figure 1.5: **Transmission Mössbauer spectrum of Fe$_{65}$Ni$_{35}$ at room temperature.**

The transmission Mössbauer spectrum of Fe$_{65}$Ni$_{35}$ at room temperature shown in Fig. 1.5 is very similar to the transmission Mössbauer spectrum of a-Fe$_{80}$B$_{20}$ (Fig. 1.2), so that a difficulty lies in describing the spectrum. The obvious physical interpretation of the Fe$_{65}$Ni$_{35}$ spectrum is based upon a static distribution of magnetic fields, in the same way the a-Fe$_{80}$B$_{20}$ spectrum is characterized[11, 12, 13]. Another representation assumes that time-dependent effects[14] on the Mössbauer nuclei cause the hyperfine fields to experience a perturbation on the same time scale as the Larmor precession, resulting in spectral line broadening and energy transitions not available to the nucleus in a stationary hyperfine field. This magnetic relaxation model also successfully describes the Fe$_{65}$Ni$_{35}$ transmission Mössbauer spectra. An experimental technique that can explicitly differentiate between time-independent and time-dependent hyperfine effects is needed to determined which physical description (static distribution of hyperfine fields or magnetic relaxation) is correct for modeling Fe$_{65}$Ni$_{35}$ transmission

7

Mössbauer spectra.

The difficulty of differentiating between the two possible physical pictures lies in the nature of a transmission Mössbauer experiment. Collecting a transmission Mössbauer spectrum involves driving allowed by the energy transitions from the hyperfine interactions. This results in a spectrum having a basic left-right symmetry. If this left-right symmetry could be broken, the energy transitions not available to the nucleus in a static field arising from dynamics could be explicitly detected. This problem is inherent to measuring either incoming *or* outgoing photons during transmission Mössbauer or single-drive scattering experiments. These methods detect what is essentially the absorption cross section of resonant Mössbauer nuclei.

If the effects of both incoming *and* outgoing photons are measured, the differential cross-section of resonant nuclei is determined. Resonant nuclei affected by time-dependent hyperfine interactions have differential cross-sections that are distinct from those which are affected by static perturbations. Unique spectral characteristics will be provided by time-dependent and static hyperfine interactions.

Selective excitation double Mössbauer (SEDM) spectroscopy measures the differential cross-section of resonant nuclei[15, 16, 17, 18, 19]. Two Mössbauer resonant scattering events provide a signal from resonant nuclei in the sample. The first resonant event pumps a selected transition of the hyperfine nuclear structure and populates a specific excited state. The second resonant event occurs during the de-excitation of a nucleus back into the ground state.

Time-dependent hyperfine interactions in a material allow Mössbauer nuclei to exchange energy with their surroundings. If this energy exchange occurs during the life-time of an excited nucleus, new levels will be populated and *extra* transitions will be observed. The SEDM spectra will exhibit these new lines, and will contain information about the relaxation process and its rate.

Even with the combined techniques of transmission Mössbauer and SEDM spectroscopy, it is not always possible to clearly separate static disorder and magnetic

8

relaxation. Transmission Mössbauer spectra of some disordered magnetic materials will show very small absorption hyperfine line-splittings, and disorder will essentially wash out the sextet. A SEDM experiment on a sample without clearly distinct line positions is problematic since it is not clear which transitions are driven. Additionally, since a transmission Mössbauer experiment is sensitive to relaxation effects that are about or above the Larmor frequency of the Mössbauer nuclei while SEDM is sensitive to magnetic relaxation that is about or below the Larmor frequency, detecting magnetic relaxation may be beyond the time resolution of the SEDM technique. Another experimental method that is sensitive to both time-independent and time-dependent magnetic effects is necessary to study systems that may be past the capabilities of transmission Mössbauer and SEDM spectroscopy.

The experimental method that we used to complement transmission Mössbauer and SEDM spectroscopy was muon spin relaxation (μSR) spectroscopy. The muon is a sensitive local probe of magnetism, and zero-field (ZF) μSR simultaneously provides clear indications of static and dynamic magnetism. Furthermore, the measuring times of Mössbauer effect experiments and μSR overlap, allowing direct comparison of fluctuation rates.

ZF-μSR is ideal for the study of alloys which present both static and dynamic magnetic disorder, such as frustrated magnets. A frustrated magnet is a ferromagnetic system with a concentration of antiferromagnetic moments, high enough that a portion of moments in the alloy cannot determine which orientation to choose. Initially, at high temperatures, there is a paramagnetic to ferromagnetic phase transition where the z component of the moments order collinearly. Subsequently, at a lower temperature, transverse spin freezing happens where the x and y components of the moments slow down and eventually freeze out and the system enters a state where ferromagnetic and spin-glass order coexist[20]. The phase diagram in Fig. 1.6 from Monte Carlo simulations shows this evolution from ferromagnet to spin-glass with increasing frustration, f[21].

Theoretical work has centered on the use of Monte Carlo methods with a moder-

9
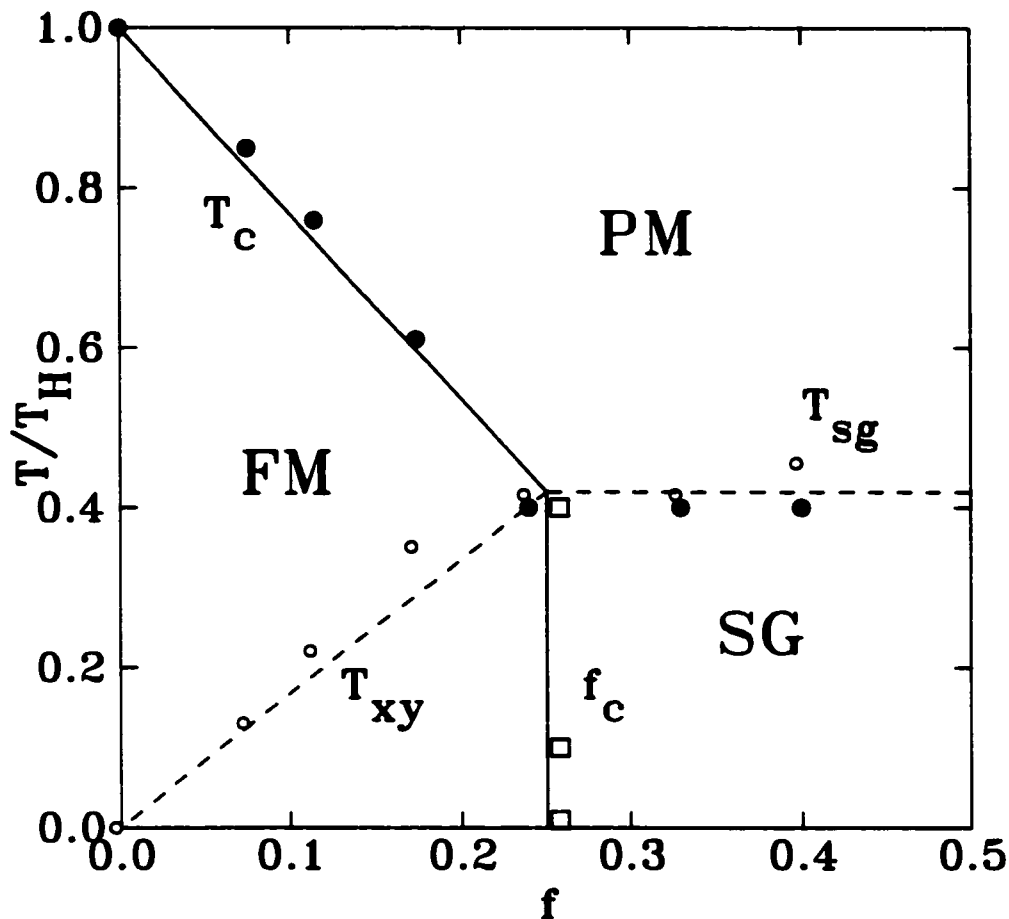
Figure 1.6: The phase diagram of a frustrated magnet showing two magnetic transitions in the concentration (frustration) region between $f = 0$ and the spin-glass phase at $f > 0.25$. f represents the fraction of interactions from antiferromagnetic bonds. At T_C, collinear order sets in, followed by the freezing of transverse spin components below T_{xy}. f_c marks the boundary between the ferromagnet and spin-glass phase. The temperature scale is normalized to the Heisenberg ferromagnetic transition temperature, T_H. From Ref. [21].

ately frustrated Heisenberg model in three dimensions[21]. This is the simplest model that could be expected to show transverse spin freezing, and is capable of reproducing all the observed features. By analysis of the fluctuations occurring at the point of freezing, the model shows transverse spin freezing is only a change in the short-range order, and not a phase transition. An example of these fluctuation results from the Monte Carlo work is shown in Fig. 1.7.

Experimentally, iron-rich amorphous alloys of the form Fe_xT_{100-x}, where T is an early transition metal such as Sc, Y, Zr or Hf[22], are ideal systems for the study of

10
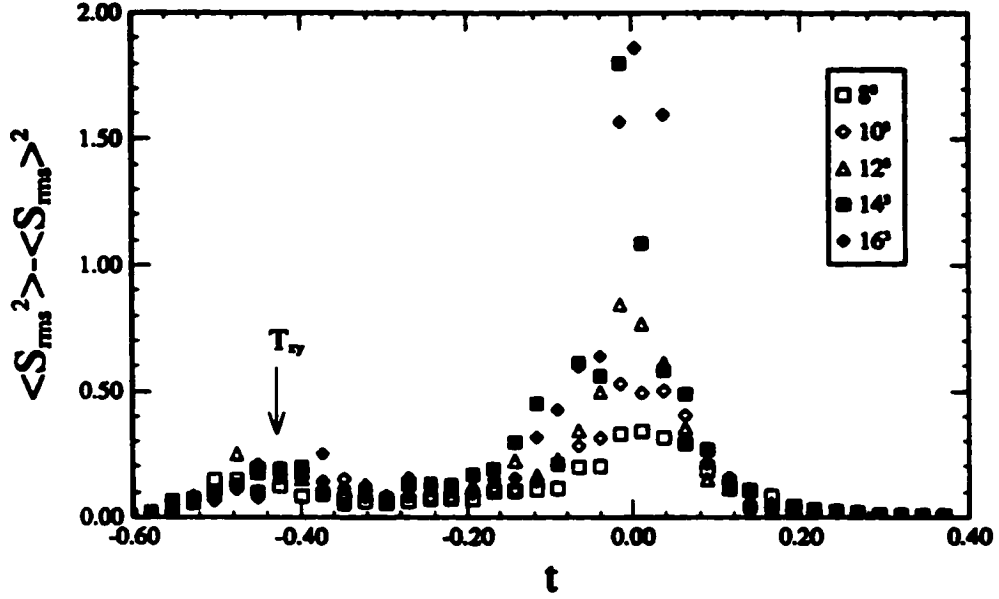
Figure 1.7: The configuration to configuration fluctuations in the average moment, S_{rms} as a function of $t=(T\text{-}T_C)/T_H$. Note the peak at T_{xy} does not grow with system size, while that at T_C grows as the system size is increased. From Ref. [21].

exchange frustration. Nonrandom substitution is avoided since these materials are quenched by melt-spinning. A high iron concentration ($\sim 90\%$) averts percolation effects and results in a high transition temperature. The exchange frustration arises from the distance dependence of the iron-iron direct exchange interaction[22], and this dominates the magnetic ordering, as shown by the large moments and strong exchange reflected in the high transition temperatures[22, 23].

We have used ZF-μSR to study a-Fe_xZr_{100-x} melt-spun metallic glasses. These materials are extremely stable and uniform[22, 23] and frustration can be tuned all of the way from ferromagnetic order to spin-glass simply by varying the iron content.

Motivation for this work

It is clear that to understand the nature of magnetism in many materials it is necessary to disentangle the effects of static and dynamic disorder. To accomplish this,

11
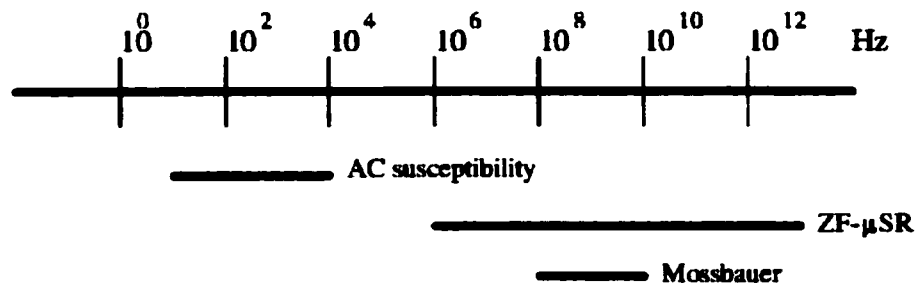
Figure 1.8: Comparison of measuring times of the experimental methods.

the zero-field experimental techniques of transmission Mössbauer, SEDM, and μSR spectroscopy were used. These methods were used to study various systems which exhibit static disorder, dynamic disorder, and both forms of magnetic disorder. Zero-field experimental methods are crucial when studying time-dependent magnetism, as an external field will perturb magnetic moments, making it much more difficult to understand the underlying magnetism. The overlap of measuring times between the experimental techniques, shown in Fig. 1.8, allows a consistent picture of the time-dependent magnetic behavior in a system to be constructed.

The main issues we will address in this thesis are the following:

- Construct the first efficient SEDM spectrometer to be used in the study of *real* magnetic materials. Samples are not enriched with ^{57}Fe and a standard 1 GBq CoRh source is used.

- Study the nature of static magnetic disorder in an amorphous alloy by establishing a consistent picture using conventional transmission Mössbauer and SEDM spectroscopy. Both methods measure the effects of the random static distribution of local magnetic environments around Mössbauer nuclei.

- Investigate the dynamic magnetic behavior in fine particle systems. Establish a model for transmission Mössbauer spectra which can describe the entire range of magnetic behavior, from blocked moments on towards collective excitations, and superparamagnetic moments. Account for the effects of interparticle interactions

and a distribution of particle sizes.

- Use SEDM to determine the *first* model independent relaxation rate of super-paramagnetic particles.

- Use SEDM spectroscopy to unambiguously demonstrate the existence ($Fe_{92}Zr_8$) and absence ($Fe_{65}Ni_{35}$) of magnetic relaxation in chemically disorder alloys.

- Identify the effect that a 180° superparamagnetic moment flip will have on the nuclear hyperfine transitions with SEDM.

- Collect and interpret the μSR spectra of a magnetic fine particle system.

- Compare the superparamagnetic relaxation rates determined from transmission Mössbauer spectra fits with results obtained with SEDM and μSR spectra.

- Establish the accuracy of the lineshape model used to characterize collective magnetic excitations in transmission Mössbauer spectra with SEDM and μSR data.

- Measure μSR spectra of a frustrated magnet, simultaneously establishing the static and dynamic disorder in the system at temperatures above T_C, on through T_{xy} and below.

- Use SEDM to verify the existence of a fluctuation peak at T_{xy} measured with μSR. Compare fluctuation rates and determine the time-dependent hyperfine interactions due to transverse spin freezing.

Chapter 2

Experimental Methods

We have used two experimental techniques based upon the Mössbauer effect: conventional transmission Mössbauer spectroscopy and selective excitation double Mössbauer (SEDM) spectroscopy. Additionally, we have used muon spin relaxation (μSR) spectroscopy, which probes similar hyperfine field effects as the Mössbauer effect with an overlapping measuring time. We describe these experimental techniques in the following sections.

2.1   Transmission Mössbauer spectroscopy

The recoil-free resonant emission and absorption of γ-rays by a nucleus is the basis of the Mössbauer effect. The unique feature of the Mössbauer effect over other resonant processes is the elimination of the destructive effects of recoil energy, a critical ingredient for nuclear resonant processes.

For the ^{57}Fe isotope (most commonly used as a source in Mössbauer spectroscopy) the 14.4 keV transition has a width, $\Gamma = 4.67 \times 10^{-9}$ eV, resulting in an energy resolution of $\sim 10^{12}$. If recoil occurs (from momentum conservation) this energy resolution is greatly decreased. For example, if a free atom emits a γ-photon, the energy of the photon is $E_\gamma = E_0 - E_R - E_T$ with E_0 representing the transition energy, E_R the recoil energy, and E_T the thermal energy of the atom. The recoil

14

energy, E_R, is proportional to the square of the γ-ray energy

$$E_R = \frac{E_\gamma^2}{2mc^2} \tag{2.1}$$

where c is the velocity of light and m the atom's mass. The thermal energy, E_T, depends on the thermal motion of the nucleus, and will have a temperature dependent average value, $\bar{E}_T$. The emitted γ-photon has an energy which is smaller than the nuclear transition energy by E_R and broadened by a full width of $2\bar{E}_T$. When a γ-photon is absorbed by a nucleus, a similar situation occurs and the energy of the photon is $E_\gamma = E_0 + E_R - E_T$. The energies of the emitted and absorbed photons are shifted apart by $2E_R$.

The above description is valid for any resonance process. Consider the resonant emission and absorption of ultra-violet (UV) radiation. In this case, the transition energies for UV-photons are much smaller than for γ-rays in nuclear resonant processes, hence E_R is smaller for UV-photons. A typical energy of a UV-photon from a 100 amu atom is 6.2 eV[24], which results in $E_R = 2.1 \times 10^{-10}$ eV, and $E_T = 3 \times 10^{-6}$ eV[24]. Since E_T is much larger then E_R, the emission and absorption profiles overlap strongly in spite of the recoil energy loss. Additionally, E_R and E_T are smaller than the width of the transition energy, and energy resolution in not affected. For the 14.4 keV transition of ^{57}Fe, $E_R \sim 2 \times 10^{-3}$ eV and $\bar{E}_T \sim 10^{-2}$ eV at 300 K[25]. Here E_R is much larger than $\Gamma \sim 10^{-9}$ eV of the transition energy, and the $2E_R$ shift will lead to no overlap between emission and absorption profiles of γ-photons. The resonant process is completely destroyed. Occasionally, thermal broadening, $\bar{E}_T$, (which is larger than E_R) will provide a condition where emission and absorption profiles may overlap, however, energy resolution is reduced by $\sim 10^7$[24].

A very different, and much more useful situation occurs, when the atom is bound to a solid matrix. The recoil energy is now transferred to the lattice and phonons are created. As phonons are quantized, a minimum energy is required to produce one. If recoil energy is less than the energy necessary to create a phonon in the lattice, the γ-photon will be emitted without energy transfer to the lattice (i.e. a zero-phonon

event). Similarly, the nuclei in a solid can absorb γ-photons in a recoil-free process. This recoil-free nuclear resonant process forms the basis of the Mössbauer effect, and can be achieved in some solid materials[24]. Thermal broadening is also eliminated when the atom is bound to the matrix, and the full extent of the extremely small natural full-width of the transition energy ($\Gamma \sim 10^{-9}$ eV) with respect to the 14.4 keV transition leads, in practice, to an energy resolution of one part in 10^{12}.

During a transmission Mössbauer spectroscopy experiment, a solid matrix containing the excited nuclei of a suitable isotope is used as the γ-ray source. A second matrix containing the same isotope in its ground state is placed in front of the source and will absorb incident γ-photons (it is the sample). The intensity of γ-rays transmitted through the sample is measured and tiny differences between the transition energies in source and sample can be measured due to the high energy resolution of the Mössbauer effect. Moving the source relative to the sample Doppler shifts the source energy, and any increase or decrease in velocity away from a transition energy in the sample will result in a reduction of absorbed γ-photons. Recording the absorption of photons as a function of Doppler velocity will show an absorption spectrum (Fig. 2.1).

Hyperfine interactions between a nucleus and its environment will affect the nuclear transition energy. This can be measured with Mössbauer effect spectroscopy. Hyperfine interactions can be time-independent (static) or time-dependent (dynamic).

2.1.1   Static hyperfine interactions

Isomer shift

The isomer shift, δ, is due to the Coulomb interaction between the nuclear charge distribution over a finite nuclear radius, and the s-electron charge density at the nucleus. This charge density will vary with the different chemical environments. The shift of the energy levels due to the Coulomb interaction will differ in source and absorber, and the absorption peak in a transmission Mössbauer spectrum will be
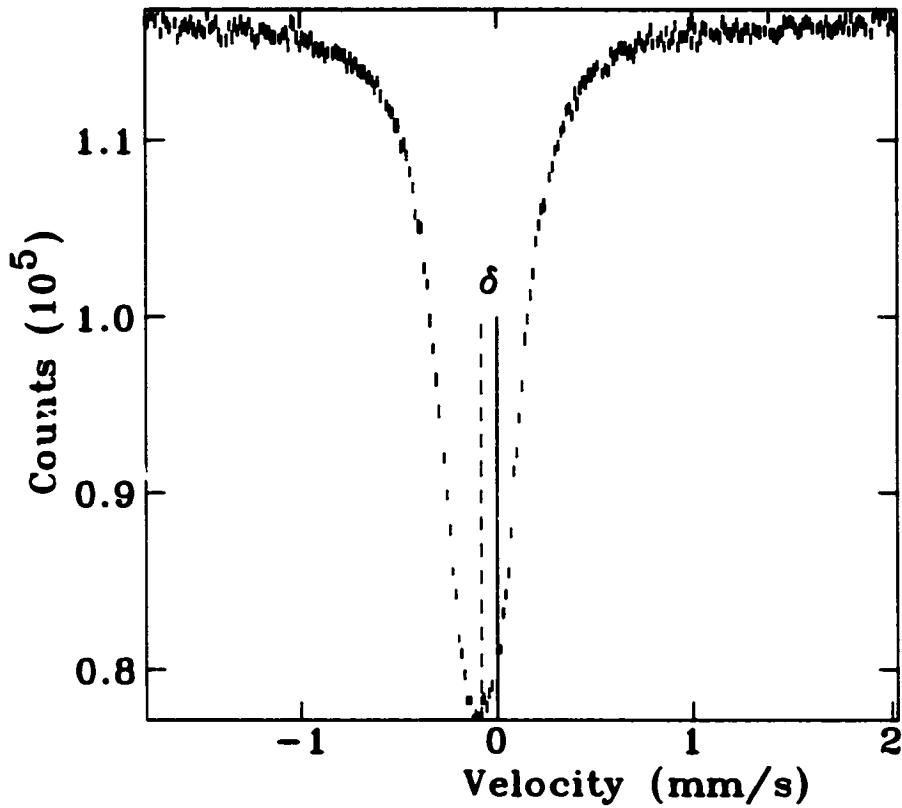
Figure 2.1: Room temperature transmission spectrum of a 10 μm thick stainless-steel foil. The isomer shift is denoted by δ.

shifted by δ (Fig. 2.1) from the center of the spectrum.

Electric quadrupole interaction

The interaction between nuclear electric quadrupole moment and electric field gradient at the nucleus results in a quadrupole splitting, Δ. The nuclear quadrupole moment is a measure of the deviation of the nuclear charge distribution from spherical symmetry[25] and the electric field gradient depends on the electrostatic potential at the nucleus[24]. For ^{57}Fe the quadrupole interaction of the ground state $(I = \frac{1}{2})$ is zero, and the quadrupole interaction splits the $I = \frac{3}{2}$ excited state into two sublevels.
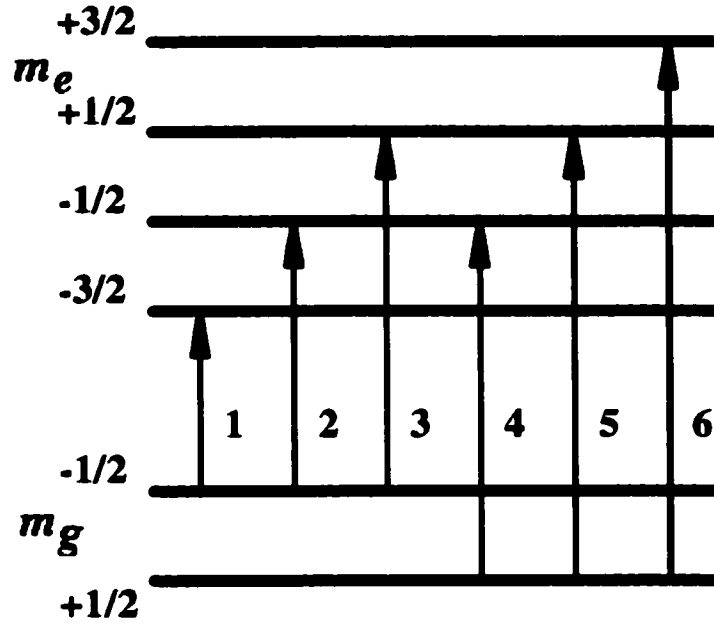
Figure 2.2: Energy level diagram of magnetic hyperfine splitting in ^{57}Fe.

Magnetic hyperfine interaction

The interaction of a nuclear magnetic moment, $\vec{\mu}$, with a magnetic field, $\vec{B}_{hf}$ at the nucleus splits the nuclear states with spin quantum numbers I into $2I + 1$ sublevels. This interaction can be described by the Hamiltonian

$$\mathcal{H} = -\vec{\mu} \cdot \vec{B}_{hf} = -g\mu_N \vec{I} \cdot \vec{B}_{hf} \tag{2.2}$$

where g is the nuclear g-factor and μ_N is the nuclear magneton. The energies of the nuclear sublevels are given by

$$\Delta E_M = -g\mu_N B_{hf} I_z \tag{2.3}$$

where I_z is the z component of the nuclear spin quantum number I.

For ^{57}Fe the excited state with $I = \frac{3}{2}$ will be split into four sublevels by the magnetic hyperfine interaction, and the ground state with $I = \frac{1}{2}$ into two sublevels (Fig. 2.2). Transitions between different sublevels can occur if $\Delta I_z = 0$ or ± 1, so a six-line spectrum occurs. A example of a magnetically split spectrum showing six well resolved absorption lines (α-Fe) is shown in Fig. 2.3. It is known that $B_{hf} = 33$ T

18
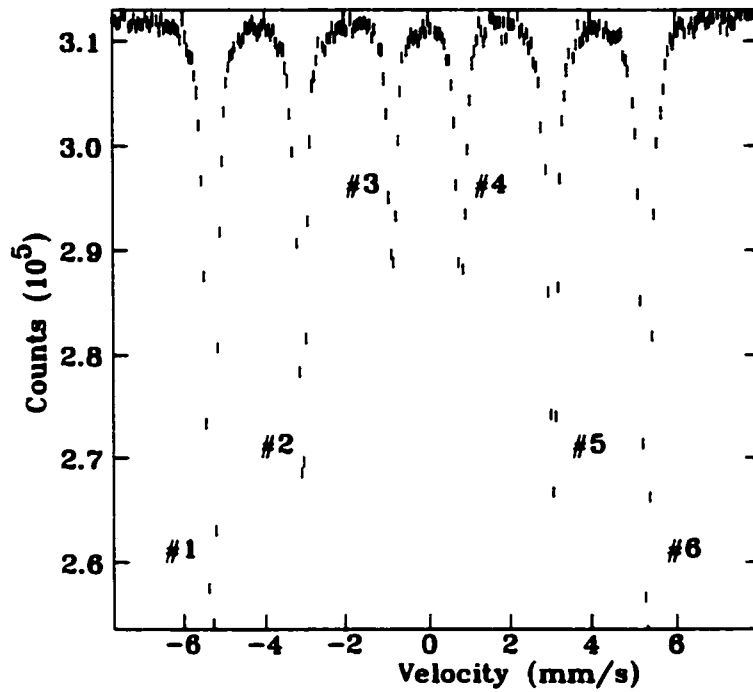
Figure 2.3: Transmission Mössbauer spectrum of α-Fe.

in α-Fe at room temperature[24], and the positions of the six absorption lines can be calculated to be at ±5.3123 mm/s, ±3.0670 mm/s and ±0.8397 mm/s. α-Fe is typically used for velocity and isomer shift calibration of the Doppler transducer.

The intensity ratios of the spectral lines are defined by the relation 3:R25:1:1:R25:3 where R25=$4\sin^2(\theta)/(1 + \cos^2(\theta))$ and θ is the angle between the magnetic moment and the direction of the γ-rays. When the magnetization of a sample is parallel to the γ-rays, $\theta = 0$, resulting in a four line spectrum. If the magnetization of a sample is perpendicular to the γ-rays, R25=4, the maximum value. For a powder sample, each Mössbauer nucleus is oriented in a random manner, and integrating over all θ's results in R25=2.

2.1.2 Static disorder

Mössbauer spectra of crystalline materials can usually be described with a small number of discrete values of hyperfine parameters (e.g. δ, Δ and B_{hf}). Some of the materials studied here were amorphous alloys and alloys with chemical disorder where
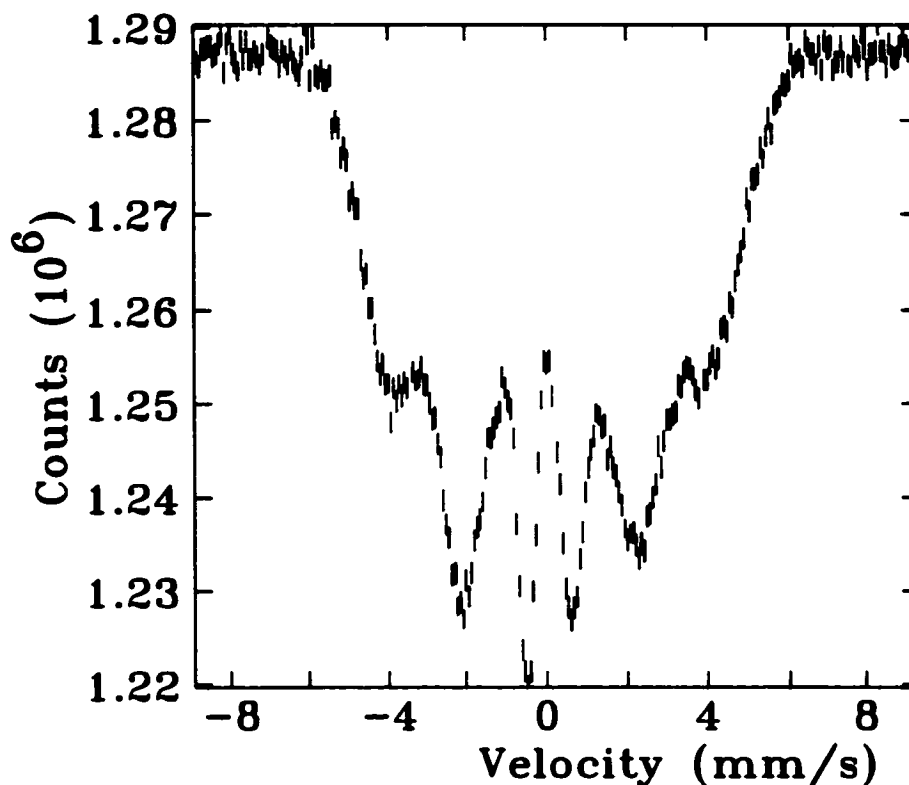
Figure 2.4: Transmission spectrum of a-Fe$_{92}$Zr$_8$ at 20 K.

the Mössbauer nuclei in the samples experience a variety of local environments. A continuous distribution of hyperfine parameters is necessary to describe Mössbauer spectra of these compounds. An example of a transmission spectrum of an amorphous material, a-Fe$_{92}$Zr$_8$, is shown in Fig. 2.4.

There are differences between the spectrum of a-Fe$_{92}$Zr$_8$ in Fig. 2.4 and that of α-Fe in Fig. 2.3, a crystalline metal (bcc) with a single 33 T hyperfine field. Although both spectra exhibit six absorption lines, the linewidths of a-Fe$_{92}$Zr$_8$ are much broader and the lineshape of the spectrum is dissimilar to α-Fe. These differences are due to a distribution of static hyperfine fields about the Mössbauer nuclei in the chemically and magnetically disordered material.

2.1.3 Dynamic disorder

The Mössbauer effect and hyperfine interactions have characteristic times, and are sensitive to environmental changes during these times. Time-dependent changes around a Mössbauer atom are called relaxation processes. Magnetic relaxation occurs when the magnetic configuration around Mössbauer nuclei change with time. Orientational changes of the electronic spin vary the magnitude and direction of a hyperfine field. The period of time over which the hyperfine field remains unchanged is the relaxation time, τ, of the process. The relaxation rate, or frequency, is given by $\nu = 1/\tau$.

The way a Mössbauer spectrum is altered by magnetic relaxation depends on the relative magnitudes of ν and the nuclear Larmor precession frequency ν_L. When $\nu \gg \nu_L$, the hyperfine field changes so quickly that it is time averaged to zero. Hence, the Mössbauer nucleus experiences no hyperfine field and a spectrum shows no line splitting. This occurs during fast paramagnetic and superparamagnetic relaxation. If $\nu \ll \nu_L$, the hyperfine field varies so slowly as to appear static to the Mössbauer nucleus. When $\nu \sim \nu_L$, the relaxation rate is just fast enough to affect the excited Mössbauer nucleus with a time-averaged hyperfine field before its decay. This results in a spectrum with broadened absorption lines. Herein lies one of the difficulties differentiating between static and dynamic disorder. Slow magnetic relaxation exhibits similar spectral characteristics as static disorder. This confuses the issue of resolving whether a transmission Mössbauer spectrum of a material is exhibiting effects from static or dynamic phenomena.

2.1.4 The transmission Mössbauer spectrometer

A schematic diagram of the setup used to collect a transmission Mössbauer spectrum is in Fig. 2.5. A 1 GBq ^{57}CoRh source is attached to a Wissel[26] MA-260 velocity transducer (Doppler modulator). The velocity of the source is controlled with a Wissel DFG-1200 digital function generator and a Wissel MDU-1200 driving unit. The drive function generator is essentially a digital-to-analog (DA) converter with an
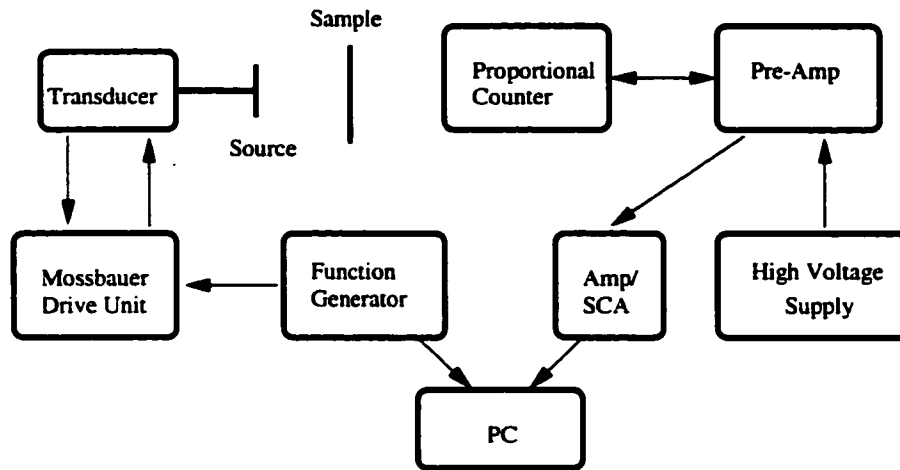
Figure 2.5: A schematic diagram of a transmission Mössbauer spectrometer.

internal clock that supplies the driving unit with a voltage waveform. This waveform, for a conventional transmission Mössbauer experiment, is a triangle (constant acceleration), and is amplified by the driving unit so the maximum and minimum voltages of the triangle waveform correspond to highest positive and negative velocities of the transducer (set by the operator). The drive function generator also provides TTL logic pulses for the channel advance, start signal denoting the beginning of the waveform, and sign signal for the positive and negative velocities of the waveform. With the transducer in a constant acceleration arrangement, γ-rays which pass through the sample are detected with a Xe plus 3% CO_2 proportional counter[27]. The signal from the proportional counter is amplified, and an ORTEC[28] single-channel analyzer (SCA) takes this output and is set to reject signal from all but the 14.4 keV γ-photons. The output of the SCA is then sent to a PC with an ORTEC multi-channel scaling (MCS) data acquisition card. The start and channel advance signals from the drive function generator are used to synchronize the γ-ray counts in the MCS so that counts collected for every channel of the function generator correspond to a specific velocity.

The transmission Mössbauer spectrometer was calibrated with α-Fe at room temperature. Spectra of the $Fe_{65}Ni_{35}$ sample were collected in an evacuated furnace. Spectra of the Fe_3O_4 ferrofluids and $Fe_{92}Zr_8$ were collected using a closed cycle re-

frigeration system at temperatures from 12 K to 300 K. The upper temperature of 180 K for the ferrofluids was set by the melting point of the carrier liquid. Spectra of the polysaccharide iron complex were collected in the same close cycle refrigeration system except for the 2 K, 5 K, 7 K and 15 K spectra that were collected in a helium flow cryostat.

2.2 Selective excitation double Mössbauer spectroscopy

Collecting a transmission Mössbauer spectrum involves equally driving all the energy transitions in the sample. The fundamental left-right symmetry of a transmission Mössbauer spectrum (Fig. 2.3), due to measuring what is essentially the absorption cross-section of resonant Mössbauer nuclei, results.

If the effects of both incoming and outgoing γ-photons can be detected, the differential cross-section of resonant nuclei is measured. This can be achieved using selective excitation double Mössbauer (SEDM) spectroscopy. SEDM is sensitive to time-dependent hyperfine interactions in a way which explicitly shows their existence. If an energy exchange between Mössbauer nucleus and surroundings occurs during the life-time of an excited nucleus, extra transitions (not available to the Mössbauer nucleus in a static magnetic field) will be observed and SEDM spectra will exhibit these new lines.

Two Mössbauer resonant scattering events provide a signal from resonant nuclei in the sample. The first resonant event pumps a selected transition of the hyperfine nuclear structure and populates a selected excited state. The second resonant event occurs during the de-excitation of a nucleus back into the ground state. SEDM spectra of material with a single, static hyperfine field (e.g. α-Fe) are collections of the following events: Say the $m_g = -\frac{1}{2} \rightarrow m_e = -\frac{3}{2}$ transition (see Fig. 2.2) is pumped. After the life-time of the Mössbauer nucleus, a de-excitation via the $m_e = -\frac{3}{2} \rightarrow m_g = -\frac{1}{2}$ transition occurs. A single, sharp line (see line #1 in Fig. 2.6) is the

23

result. If the $m_g = -\frac{1}{2} \to m_e = -\frac{1}{2}$ transition is pumped, de-excitation through the $m_e = -\frac{1}{2} \to m_g = -\frac{1}{2}$ and $m_e = -\frac{1}{2} \to m_g = +\frac{1}{2}$ transitions will occur. Two sharp lines whose intensities are proportional to the cross-sections of the respective transitions is the outcome (Fig. 2.6).

The SEDM apparatus, shown in Fig. 2.7, requires two Doppler modulators. One is
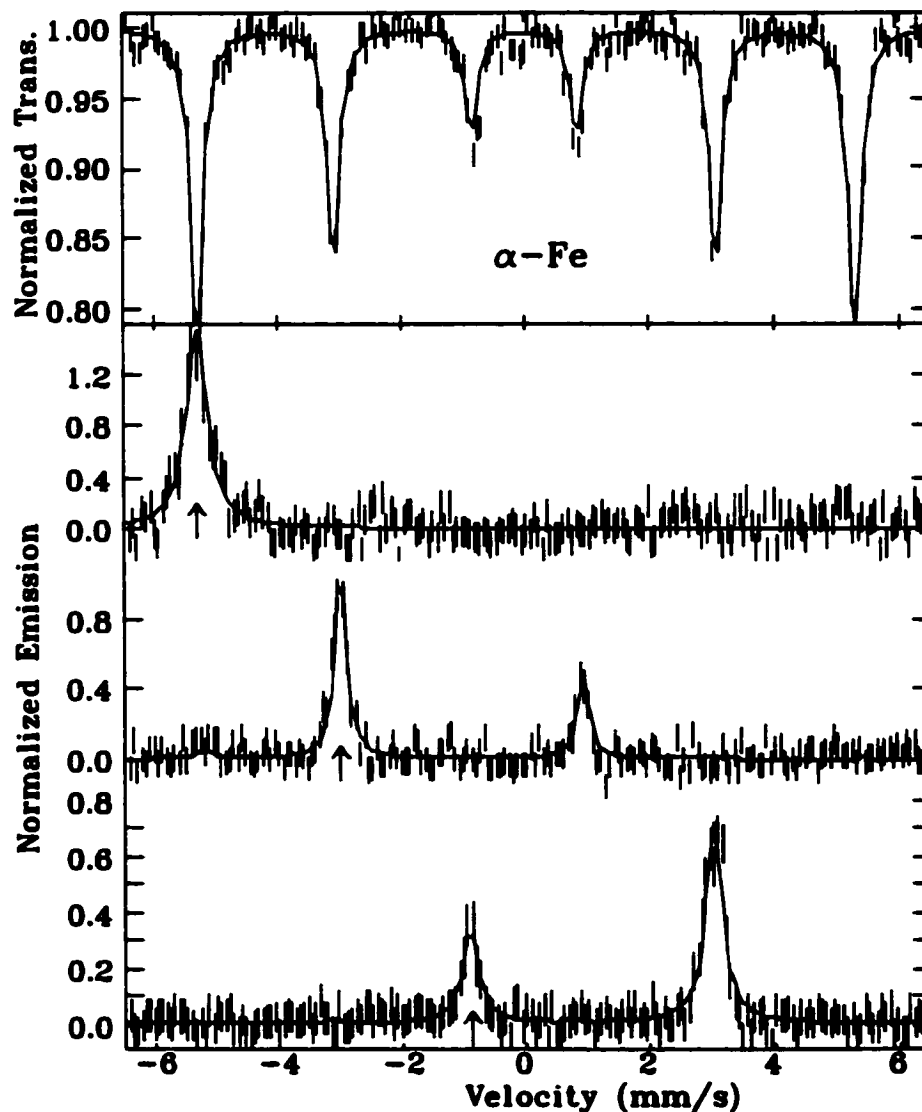
Figure 2.6: Transmission Mössbauer spectrum of α-Fe and the SEDM spectra when lines #1, #2 and #3 are driven (pump energies indicated by the ↑).
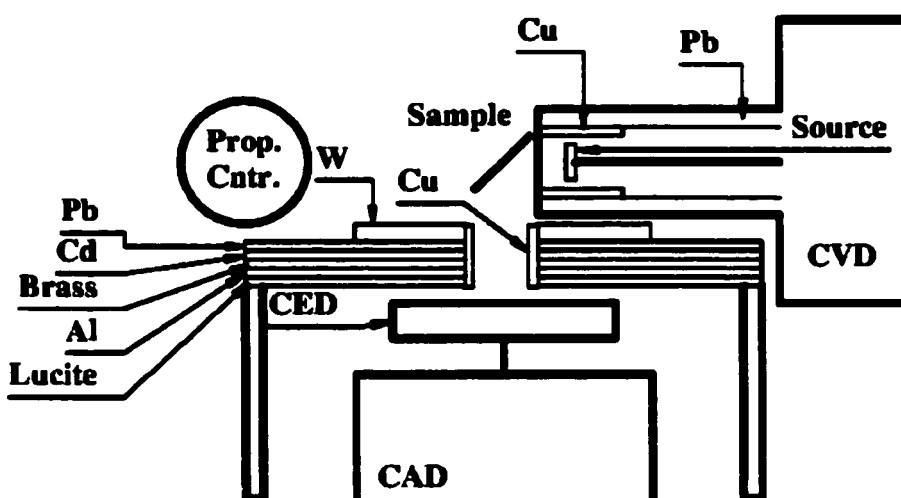
Figure 2.7: Top: Photograph of the SEDM apparatus with the closed-cycle refrigeration system. From left to right: Prop. counter, CAD with CED, CVD with source. Bottom: Schematic block diagram of the SEDM apparatus.

used to drive the single line Mössbauer source at a constant velocity (CVD), populating the desired nuclear sublevel in the sample. The other velocity transducer is used to record the scattered radiation from the sample by moving a single-line analyzer with a constant acceleration (CAD)[19].

Two things are crucial for a successful SEDM experiment. One is perfect synchronization of the CVD and CAD for the duration of the experiment. This is to ensure that data collection occurs only when the selected transition is being excited and that exactly the same energy for each velocity scan of the CAD is acquired by

the multi-channel scaler. Early works solved this problem using specially constructed electronics for the transducers and periodic energy calibration[16, 17, 18, 31]. Others have used expensive CAMAC technology to solve the transducer synchronization problem[35]. The second requirement is efficient detection of the scattered radiation from the sample. Early SEDM equipment used a single-line $Na_4Fe(CN)_6 \cdot 10H_2O$ absorber attached to the CAD with a standard proportional counter behind it[16, 17]. At that time, a high-efficiency proportional counter was the simplest method of measuring a signal from the sample. Still, a 2–4 GBq source was necessary for acceptable collection times.

Conversion electron detectors, in principle at least, are sensitive only to resonant photons. Microfoil conversion electron (MICE)[36] detectors are the most sensitive design of conversion electron detector. With multiple, ultra-thin ^{57}Fe enriched stainless-steel foils, these detectors offer excellent counting efficiency. A MICE detector designed to be Mössbauer transducer mounted[30] has been built, however, the extreme fragility of foils were not well suited to the constant vibration. Since the bulk of the signal comes from the first foil[36], and increasing the number of foils improves the count rate at the expense of the signal-to-noise ratio, we have built a simple, single foil, drive-mounted conversion electron detector (CED). The foil is firmly mounted onto the detector body so that it cannot vibrate. Our CED is both robust, and light enough, to be transducer mounted. With a lower counting efficiency than a MICE detector, this design of a CED still out-performs the counting efficiency of proportional counters by several orders of magnitude[37].

Our Wissel[26] Mössbauer transducers use digital-to-analog circuitry, like most modern transducers, and provide outputs which flag various conditions of the constant velocity and constant acceleration waveforms. With this information from the transducers, designing some digital electronic circuits to synchronize the CVD and CAD was a simple task.

With these ingredients, our SEDM apparatus has provided the necessary upgrade in counting efficiency, with a one thousand- [16] to five thousand- [17] fold improve-

26

ment in effective counting time when compared with previous experimental configurations, and the ability to stay synchronized for an indefinite amount of time.

2.2.1 Spectrometer design and operation

A photograph of our SEDM apparatus is shown in Fig. 2.7 along with a schematic diagram of the SEDM apparatus. We will discuss the construction and optimization of the CED, synchronization and data collection with the two drives, as well as shielding, in the following subsections. This is followed by a description of the calibration and operation of the SEDM spectrometer.

2.2.1.1 CED

The heart of our improvements to the SEDM technique is the use of a drive mounted conversion electron detector (CED) as our energy analyzer. This offers a tremendous enhancement in counting efficiency.

An orientation of 90° for the energy analyzer with respect to the source is the simplest, and fortunately, most beneficial, geometry to use in a scattering experiment. For a SEDM experiment, this setup solves two problems. One is that it reduces possible coherent Rayleigh scattering to a minimum as these scattering events have a $\cos^2(\theta)$ angular dependence. Another is that the 90° position offers the greatest distance between CVD and CAD, allowing the maximum amount of radiation shielding between source, sample and detector. This is a necessity which we will explain later in Sec. 2.2.1.3.

A detector with too large a collection area will lead to cosine broadening of the spectral lines, so it is necessary to keep the angular acceptance limits of the collected photons to a reasonable minimum. This restricts the photons that we can collect from the sample (which are radiating off the sample in all directions) to a small solid angle. An efficient detector of scattered γ photons from the sample is clearly needed. A CED provides the most efficient means of collecting resonant events from a sample.

In general, the relative advantages of a conversion electron detector go up as the magnitude of the absorption from a sample decreases[36]. An emission signal residing over low count background is a more effective detection technique for SEDM then a proportional counter which cannot offer a greater than 10% absorption signal from re-emitted γ-photons in a high count background.

A CED is basically a proportional counter with a resonant foil that acts as a cathode and a fine wire biased to a high voltage for an anode. A 14.4 keV γ-photon from a SEDM sample will resonantly scatter inside the cathode foil and excite a ^{57}Fe nucleus. Only about 10% of the nuclei will return to their ground states via a re-emitted photon. The other 90% emit a conversion electron followed by an x-ray or an Auger electron. On average, two conversion electrons are emitted for each resonant event[38], so this process offers the greatest possible signal. To reduce the sensitivity of the CED to higher energy γ-rays, a fill gas of helium is used. A few percent of a quench gas (in our case methane) is added to the helium, to keep the detector from avalanching due to photons scattering off the helium. To reduce the response of a CED to lower energy photons (such as the 6 keV x-ray from the decay of a Mössbauer nucleus), a filter material is placed in front of the cathode.

This CED is based upon a previous design used for Mössbauer source experiments with extremely low doping levels of ^{57}Co[37]. The SEDM CED is more modular, allowing for easy removal of the CED cathode sample, and attention towards sealing the detector has resulted in low He/CH_4 gas flow rates, ensuring consistent and reproducible performance. Low-density materials were used throughout the construction which served a two-fold purpose. Keeping the mass of the CED to a minimum ($\simeq$40 g for this CED) limited the possibility of adversely affecting the linear acceleration of the CAD. Lower Z materials also reduce the number of non-resonant scattering events that might take place anywhere in the CED during a measurement, diminishing background counts.

Sectional views of the Plexiglas detector body are in Fig. 2.8. The cover (not shown) is a 65 mm diameter, 2 mm thick Plexiglas disk. Plexiglas is light, easy
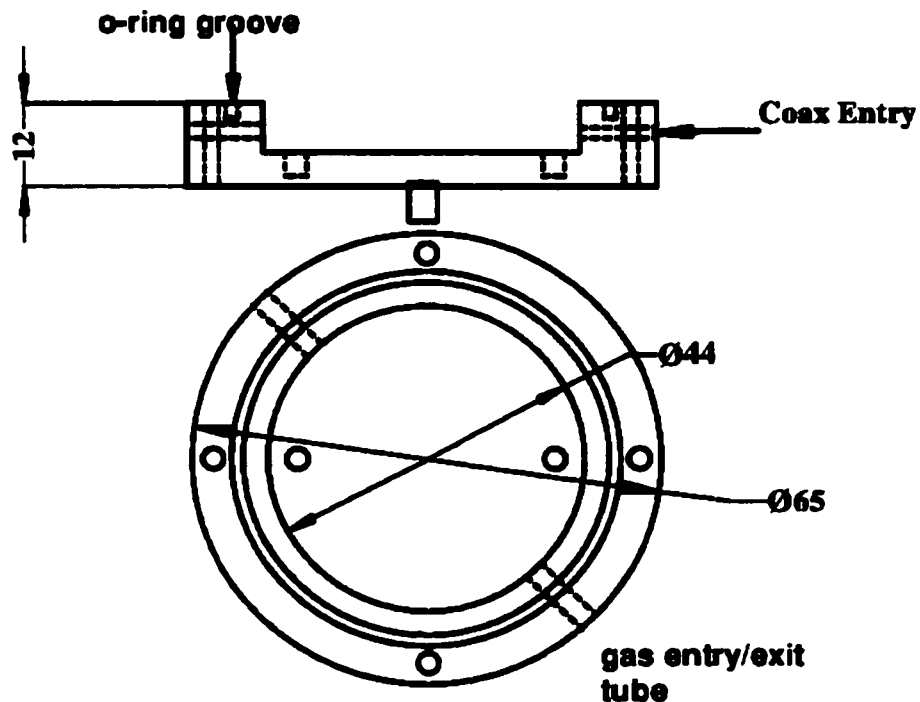
Figure 2.8: Sectional views of the detector body. All dimensions in mm.

to machine, and provides an excellent filter of the unwanted fluorescence from the sample. A 100 mm^2, 90% ^{57}Fe enriched 1.3 μm thick 310 stainless-steel foil[40] is the CED cathode. An enriched foil is used to maximize the possible resonance events from γ photons off the SEDM sample. The foil is clamped firmly in place with a 40 mm diameter, $\sim$0.1 mm thick Plexiglas ring with 9.8 mm diameter center hole to expose the cathode to the γ-photons from the sample. The anode wire is 25 μm gold-coated tungsten and soldered across the 4 mm sections of the disk shown in Fig. 2.9. This anode-holder is made of 2 mm thick copper-clad circuit board. Facing surfaces of the detector body and cover are polished and an o-ring is used to ensure a seal between detector body and cover. All inner surfaces were fully aluminized and connected to ground. Four nylon screws are used to fasten the cover to the body. A 250 mm long lightweight coaxial cable (RG-174/u) with a gold mini-SMC high-voltage connector carries the bias voltage from the pre-amp to the anode wire. One end of the SMC connector was threaded into the detector body and the anode wire was soldered onto the center pin of the connector. Thin coax is used to reduce mechanical stiffness which

29
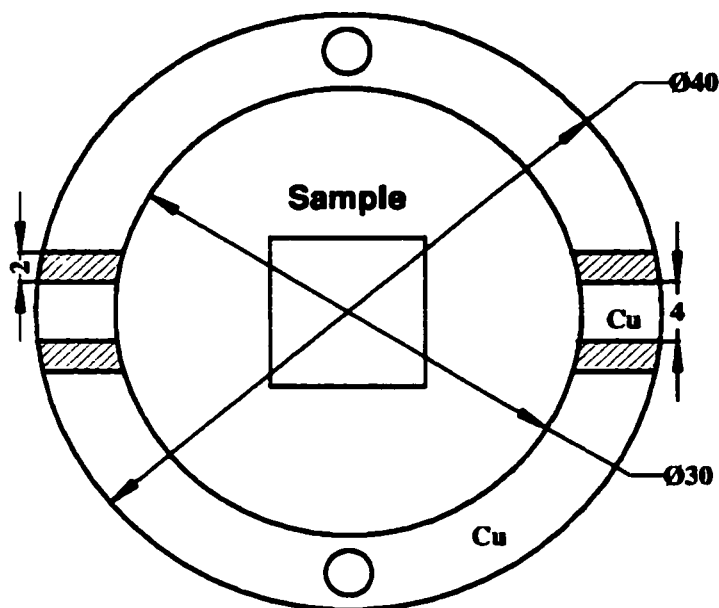
Figure 2.9: Sectional view of the anode wire mount made of 2 mm thick copper-clad circuit board. All dimensions in mm.

would interfere with oscillating the detector. The He with 4% CH_4 gas mix enters and exits though two 2 mm diameter plastic tubes. The premixed gas flows through the detector at a rate of ~ 0.1 cm^3/min. A photograph of the CED mounted onto the CAD during a SEDM experiment is shown in Fig. 2.7.

The CED was optimized for counting efficiency the following way. Initially, with the minimum possible lower level discriminator voltage, pulse height spectra of the CED on and off resonance, were collected at different bias voltages. The pulse height spectra, with the off resonance contribution subtracted, indicated when the conversion electron signal was maximized. Fig. 2.10 shows this trend for several bias voltages, with the 800 V bias showing a clear maximum for the conversion electron signal at channel ~ 100. To confirm this setting, conversion electron Mössbauer spectra of the single line stainless-steel cathode of the CED were collected at different bias voltages. The effect, $\varepsilon = I/I_\infty$ where I is the peak intensity and I_∞ is the baseline of the spectrum, was calculated for each spectrum, as well as the following measure of the effective counting time, $t_{eff} = 2(\varepsilon + 2)/(\varepsilon^2 I_\infty)$[39]. The operating bias voltage for the CED of 700 V exhibited the minimum effective counting time and maximum
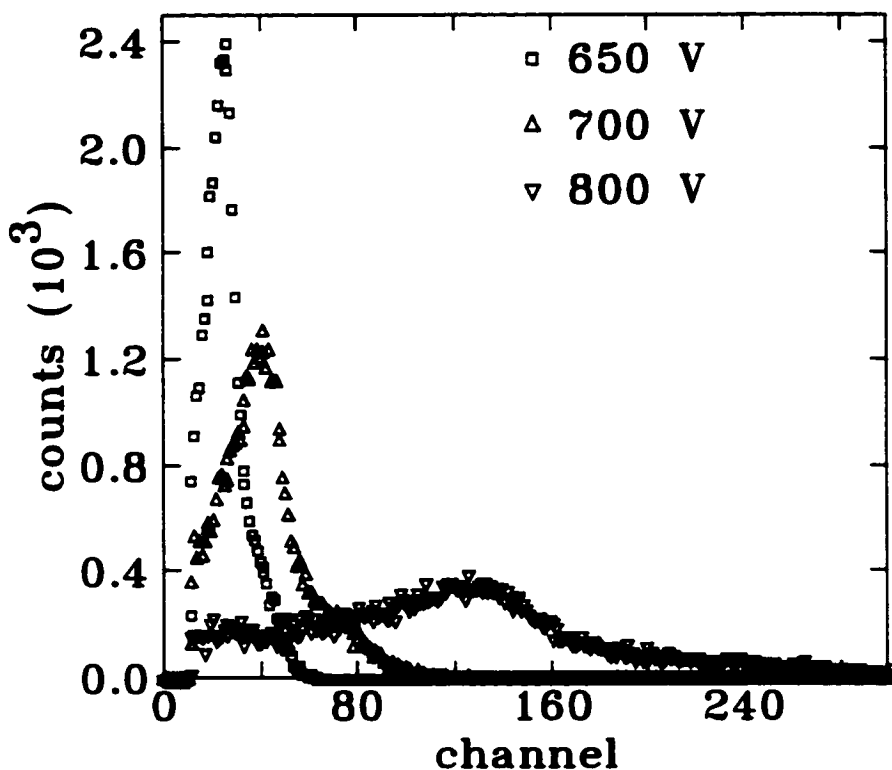
Figure 2.10: Pulse height spectra with off resonance background subtracted at different bias voltages for the CED. The conversion electron peak is clearly seen in the 800 V spectrum around channel 100.

signal effect, shown in Fig. 2.11. A spectrum of the enriched stainless-steel cathode is shown in Fig. 2.12. The CED has an operational linewidth of 0.153 ± 0.002 mm/s, compared to 0.191 ± 0.001 mm/s for a transmission spectrum of at 10 μm thick 310 stainless-steel.

Background contributions in the form of detector noise and low-energy photoelectrons were reduced with the proper selection of the lower level discriminator setting for the detector electronics. Using the same method to find the optimal bias voltage, a lower level discriminator setting of 10–12 mV was selected (see Fig. 2.13).

2.2.1.2 Drive synchronization and data collection

A requirement for SEDM spectroscopy is the synchronization of the CVD and CAD. The energy analyzer must sweep across its range of velocities while the transition is
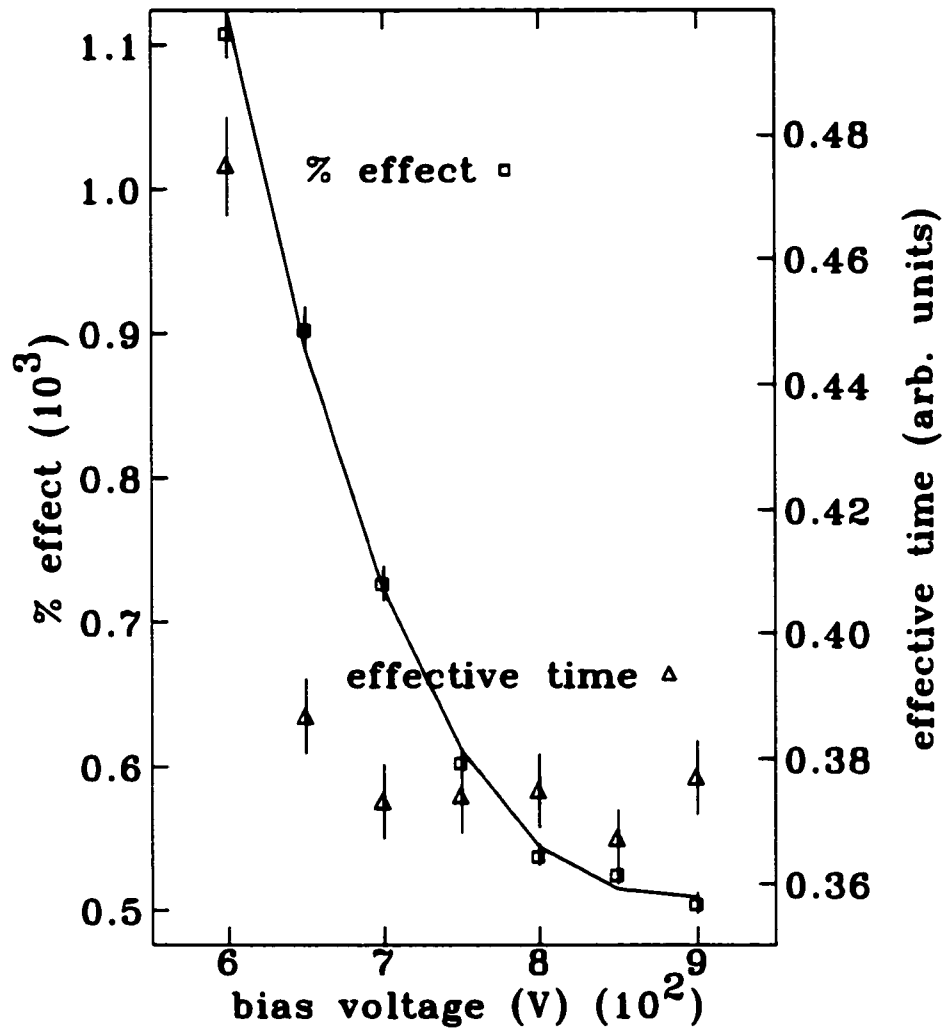
Figure 2.11: Effect (ε) and effective counting time t_{eff} as functions of CED bias voltage as described in the text. The solid line is a guide to the eye.

being pumped by the CV transducer and exactly the same velocity should be recorded in each channel of the multi-channel scaler during a scan. A Wissel[26] Velocity Transducer MA-260, Mössbauer Driving Unit MDU-1200 with a Digital Function Generator DFG-1200 was used for the CVD and a Mössbauer Velocity Transducer MA-260 with a Mössbauer Driving Unit MR-360 and a Digital Function Generator DFG-1000 was used for the CAD. The drive function generators are essentially digital-to-analog (DA) converters with internal clocks which supply the driving unit with a waveform and provide logic pulses during different parts of the waveform for data
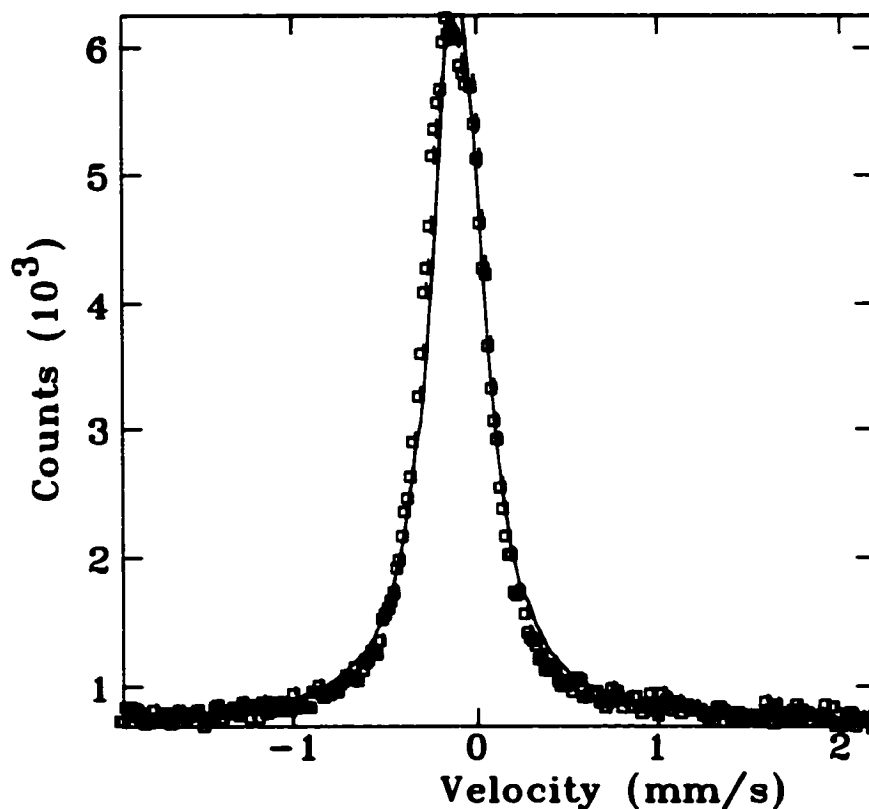
Figure 2.12: CED spectrum of the enriched 310 stainless-steel sample. A linewidth of 0.153±0.02 mm/s and and effect of ≈800% are substantial improvements over conventional transmission measurements.

collection (e.g. TTL pulses for the channel advance, a start signal denoting the beginning of the waveform, and a sign signal for the positive and negative velocities of the drive waveform). The internal clocks of the drive function generators can be disabled and an external TTL stepping pulse can be used to provide the channel advance for DA conversion to the driving unit. This feature allows the two drive systems to be used in a master/slave configuration. With an external channel advance frequency of ≈100 kHz (4096 channels×25 Hz drive resonant frequency) the CAD is slaved to the CVD using the circuit shown in Fig. 2.14. The start signal from the CVD and the sign signal from the CAD ensure that both waveforms begin at their maximum velocities at the same time. To establish synchronization after a drive has been turned off, a reset trigger is provided. The drive function generators are operated in a standard 512 channel/cycle configuration. The CAD uses a triangular, constant
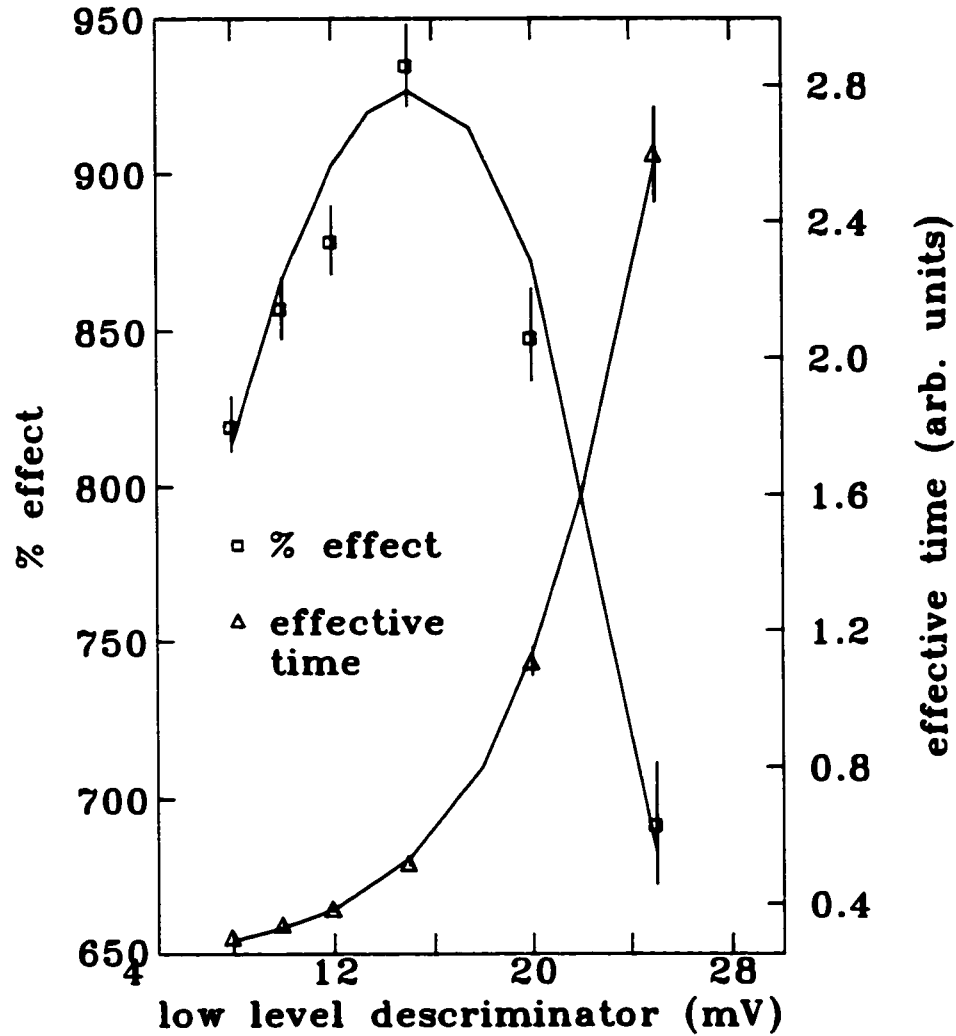
Figure 2.13: Effect (ε) and t_{eff} as a functions of the lower level discriminator setting for the CED. The solid lines are a guide to the eye.

acceleration waveform. To minimize the velocity error of the CVD proportional-integral feedback loop, a square waveform with a 20% sine wave component at the discontinuities (see Fig. 2.15) is used. Examining the diagram of the CAD and CVD waveforms in Fig. 2.15, it seems reasonable to have the CAD double its oscillation period so data can be collected during the positive and negative accelerations of the CAD and standard folding of a spectrum can occur to alleviate possible background problems. This was not possible with our Wissel drive units. The servo loop was unable to cope when operating at twice the 25 Hz mechanical resonant frequency.

34
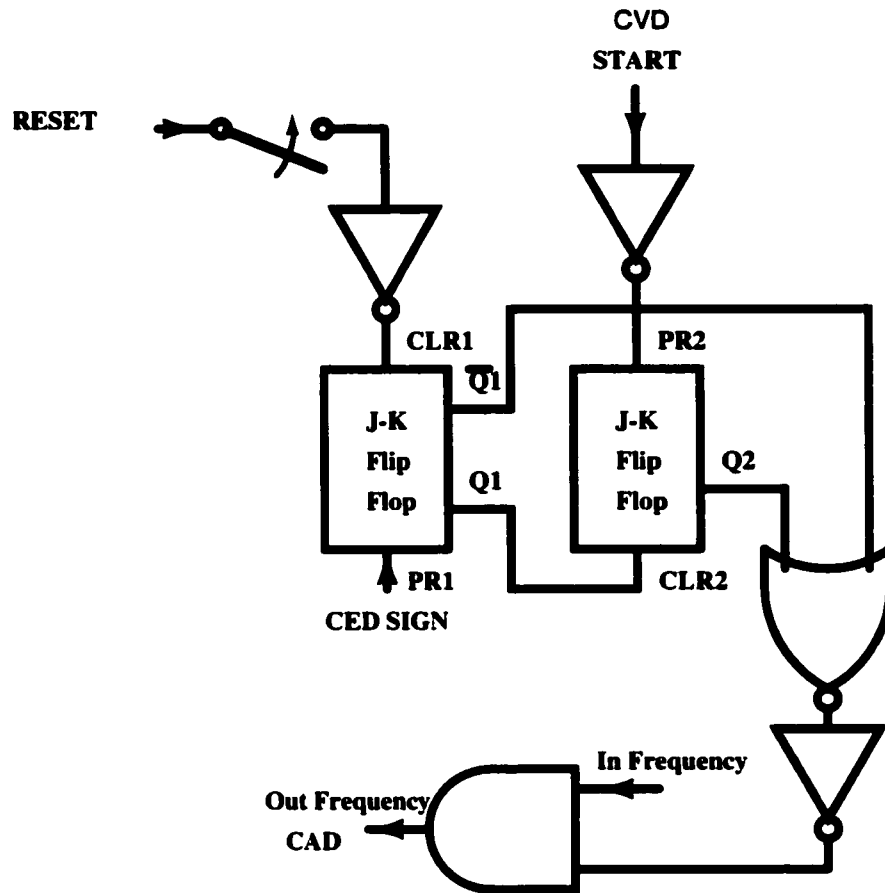
Figure 2.14: Schematic of the CVD and CAD synchronization circuit.

The function generators provide a sign signal which denotes when the waveform generates a positive or negative velocity and a count enable signal which establishes when a constant velocity section of the waveform has been reached. With the circuit in Fig. 2.16, counts from the detector are gated with the CVD sign and count enable signals. This way, the signal is collected by the multi-channel scaler data acquisition system only when the transition is being pumped by the CV transducer.

2.2.1.3 Shielding

It is very important when performing SEDM experiments to provide proper shielding of the detector from unwanted radiation. Optimum CED performance is achieved with a low background[36], so keeping non-resonant counts to a bare minimum is
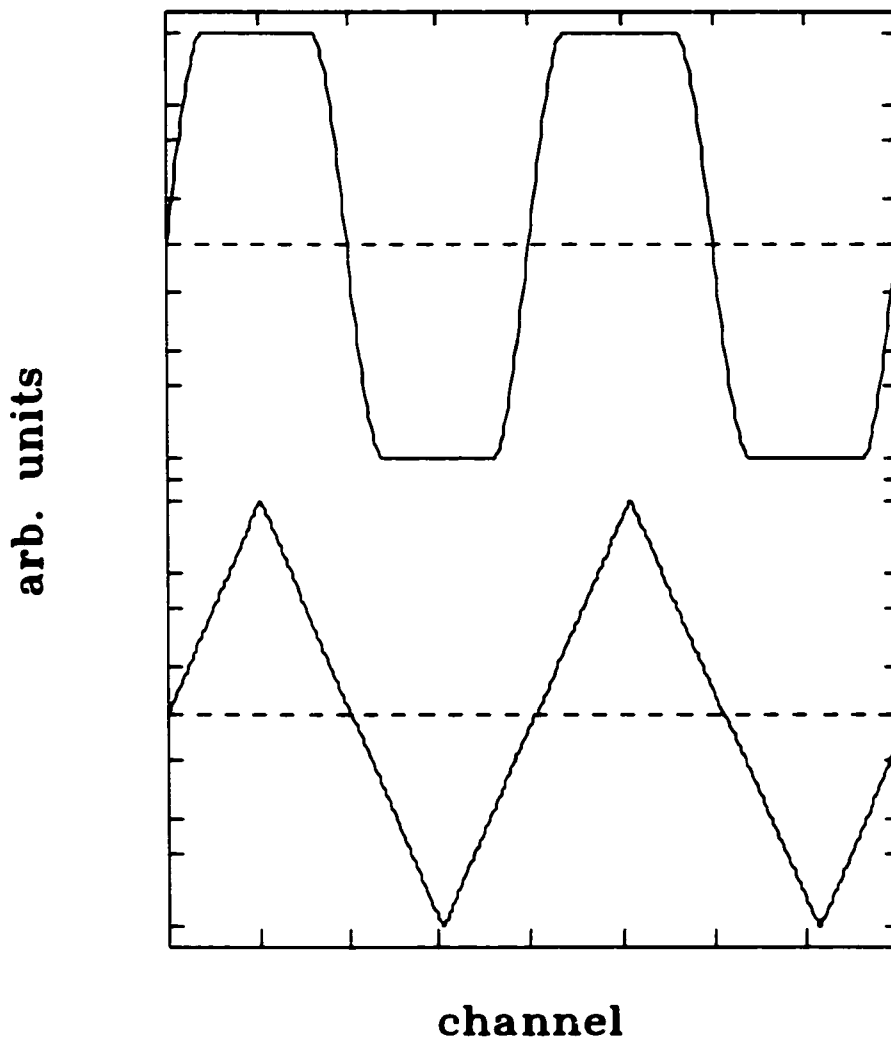
Figure 2.15: Diagram of the CVD (top) and CAD (bottom) waveforms used during a SEDM experiment.

crucial.

The biggest source of background counts is line-of-sight photons from the source. The 122 keV γ-rays from the nuclear decay of ^{57}Co can penetrate any shielding materials between source and detector. To improve the shielding for the detector, it is better to use many materials with complementary γ-ray absorption coefficients. With this in mind, each metal used for the CED shielding has an absorption coefficient which is optimum for a range of γ-ray energies. The metals are placed in a sequence
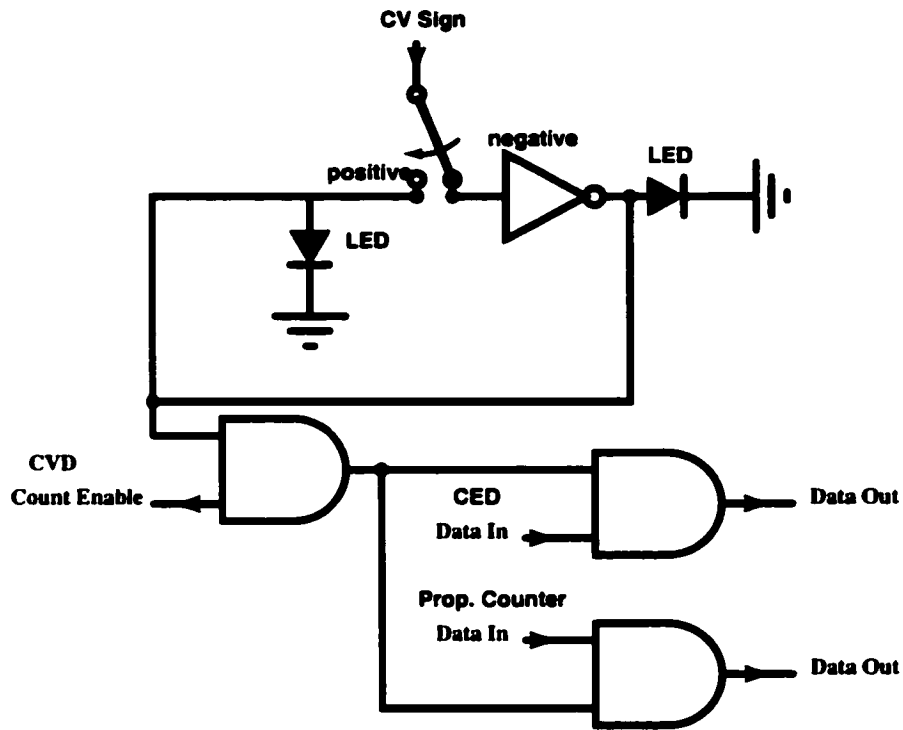
Figure 2.16: Schematic of the velocity gating circuit.

so photons of lower energies will be absorbed as they scatter on towards the CED. By the time photons have penetrated all the shielding materials, their energies are too low to create photoelectrons in the CED. An example of our shielding is schematically displayed in Fig. 2.7. 10 mm of tungsten is followed by 10 mm of lead, and then 3 mm of cadmium, 2 mm of brass, 2 mm of aluminum and 3 mm of Plexiglas. Although tungsten has a lower Z then lead, its higher density makes it a better absorber. Collimation of the scattered radiation from the sample is provided by an 11 mm inner diameter copper shell which passes through the shielding and is level with the 10×10 mm cathode. A 2 mm think copper shell sitting inside a 7 mm lead shell shields the source.

2.2.1.4 Operation

Our SEDM apparatus uses standard detector electronics, i.e. detector pre-amps, high-voltage (HV) power supplies, multi-channel analyzers and rate meters, from

ORTEC[28] and Canberra[29]. An Intel-based P.C. having two ORTEC multi-channel scaler (MCS) data acquisition cards collects the spectrum. One MCS card is used to collect counts coming from the CED (the SEDM experiment) and the other MCS card is used for collecting counts from the proportional counter when checking the CVD energy or recording the long term CED stability. The back of the CAD transducer has a source holder. A source is attached here when it is necessary to calibrate the CAD velocities. With a conventional transmission Mössbauer spectrum of the sample in hand, it is a simple task to determine the line energies for a CVD velocity. The experimental procedure for conducting a SEDM experiment is:

- Conventional transmission Mössbauer spectra are collected. These spectra are used to determine the transducer velocity for pumping a selected transition. Fits to the transmission spectra offer necessary information to fit SEDM spectra, e.g. distribution of hyperfine fields.

- With the drives synchronized for a SEDM experiment, the CVD energy is tuned across a range of energies centered about the calculated drive velocity and the gated counts from the proportional counter behind the sample are recorded in timed bins (e.g. 100 seconds per channel). The absorption as a function of drive energy will yield a maximum when the peak of the line is encountered. This is an important check of the CVD energy calculated from the transmission spectrum.

- Once the CVD energy is confirmed, the SEDM experiment begins with one MCS collecting the SEDM spectrum and the other MCS recording the CED counts in timed bins as a check of the detector performance (e.g. the number of counts per bin remains constant for the duration of the experiment).

Since the data-gating electronics collect during half of the CVD waveform, no background corrections, typically by folding, are possible. However, with our thin samples as well as source-sample and sample-CED distances of 2–5 cm, flat backgrounds were always measured.

38
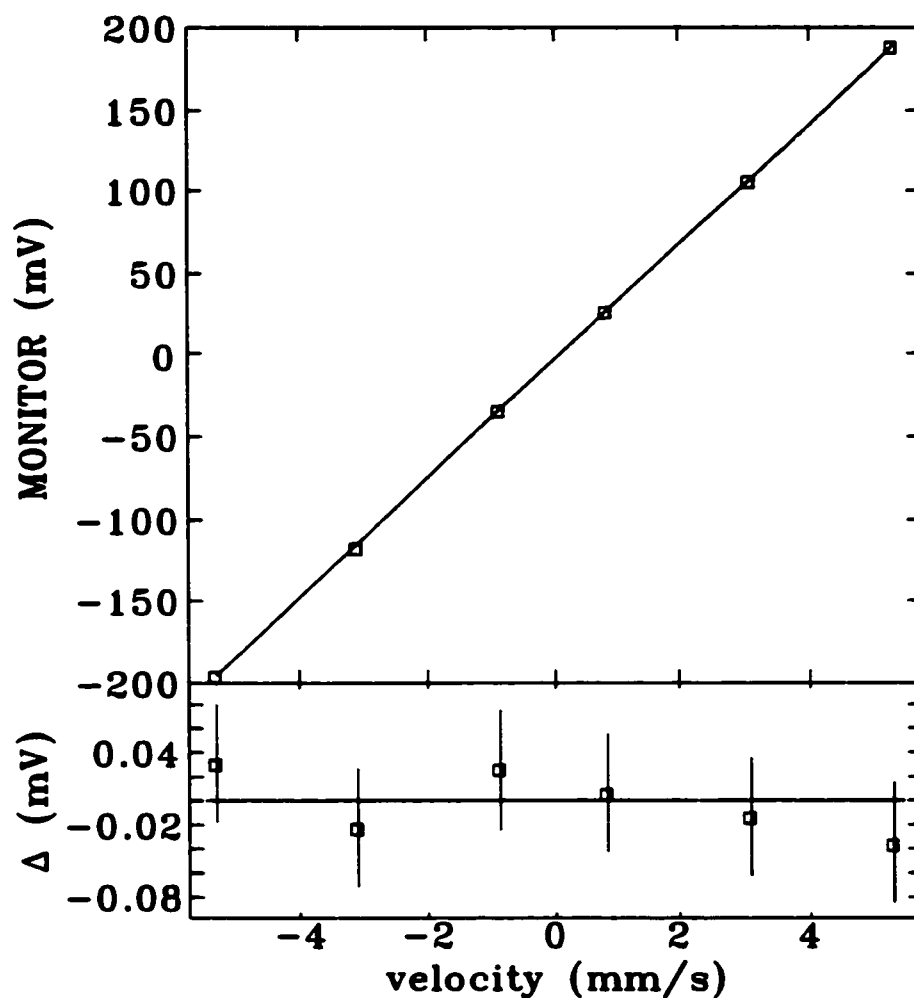
Figure 2.17: Velocity calibration of CAD with respect to the six lines of α-Fe. Residuals of the fit (Δ) are shown in the bottom part of the graph.

2.2.2 Spectrometer performance

Using a 1 GBq ^{57}CoRh source, the SEDM setup was tested on α-Fe. At first, with no calibration for the CVD velocity, all six lines of the α-Fe spectra were found by varying the CVD velocity and recording the absorption of γ-rays in the sample. A linear dependence between the AC voltage of the monitor output of the CVD and line positions for α-Fe was demonstrated and used as a calibration of the CVD velocity, shown in Fig. 2.17.
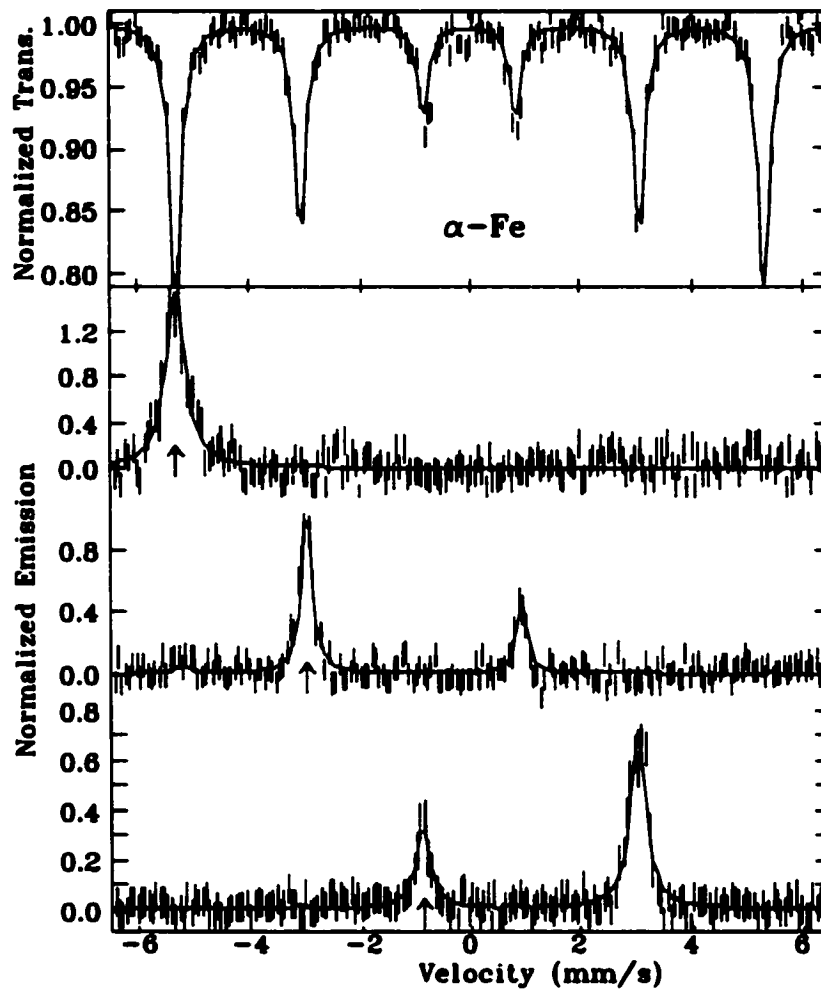
Figure 2.18: Transmission Mössbauer spectrum of α-Fe and the SEDM spectra when lines #1, #2 and #3 are driven (pump energies indicated by the ↑).

Collecting a SEDM spectrum while driving line #1 of α-Fe provided a strong indication that selective population of the $m_e = -\frac{3}{2}$ nuclear sublevel (shown schematically in Fig. 2.2) was happening. With the largest cross-section, driving line #1 would produce the strongest signal, and after approximately a day of counting, a single-line SEDM spectrum, shown in Fig. 2.18, was the result. With a line position of -5.31±0.01 mm/s, in agreement with the line #1 energy of α-Fe, the appearance of a single line agrees with the selection rules.

SEDM spectra when the excited states of lines #2 and #3 in α-Fe were populated

established that selective population of a nuclear sublevel was indeed occurring. The population of the $m_e = -\frac{1}{2}$ state results in de-excitations to the $m_g = -\frac{1}{2}$ and $m_g = +\frac{1}{2}$ states (see Fig. 2.2), i.e. pumping line #2 yields a spectrum with lines #2 and #4. When line #3 is driven, populating the $m_e = +\frac{1}{2}$ state has de-excitations occurring to the $m_g = -\frac{1}{2}$ and $m_g = +\frac{1}{2}$ states, resulting in both lines #3 and #5 in a SEDM spectrum (Fig. 2.18). This last SEDM spectrum is the most convincing evidence that selective population of the nuclear sublevels is happening, as the de-excitations via the $m_e = +\frac{1}{2} \rightarrow m_g = -\frac{1}{2}$ transition has a larger nuclear cross-section than the pumped $m_e = \frac{1}{2}$ state, resulting in the return line #5 which was *not* pumped having a much greater line intensity in the SEDM spectrum than the pumped line #3.

To evaluate the SEDM lineshape the energy distributions of the source radiation and scattered radiation from the sample as well as the detector energy resolution are required. These items are characterized by their linewidths. Including the energy distribution of the source, Γ_{CED}=0.153±0.002 mm/s, collected in a transmission geometry, describes the energy resolution of the CED. A measure of the source energy distribution is given by the inner lines (#3 and #4) of a α-Fe transmission spectrum, Γ_s=0.120±0.001 mm/s, which defines the excitation process of a Mössbauer nucleus in the source and the subsequent de-excitation. With this information, a SEDM model assuming Lorentzian lineshapes and a single hyperfine field, corrected for the CED isomer shift, was used to fit the α-Fe SEDM spectra. These spectra required approximately one day counting times, and exhibit a three order of magnitude improvement in counting efficiency over previous experiments[16, 17].

A 1 GBq ^{57}CoRh source was used to collect SEDM spectra of the $Fe_{80}B_{20}$, $Fe_{65}Ni_{35}$ and Fe_3O_4 ferrofluid samples. A 2 GBq ^{57}CoRh source was used to collect SEDM spectra of the $Fe_{92}Zr_8$ sample. SEDM spectra of $Fe_{65}B_{65}$ were collected in an evacuated furnace designed for scattering experiments (Fig. 2.19). SEDM spectra of the Fe_3O_4 ferrofluid and the $Fe_{92}Zr_8$ sample were collected in a closed cycle refrigeration system designed for scattering experiments (Fig. 2.20).

41

Figure 2.19: Photograph of SEDM apparatus with high temperature furnace.
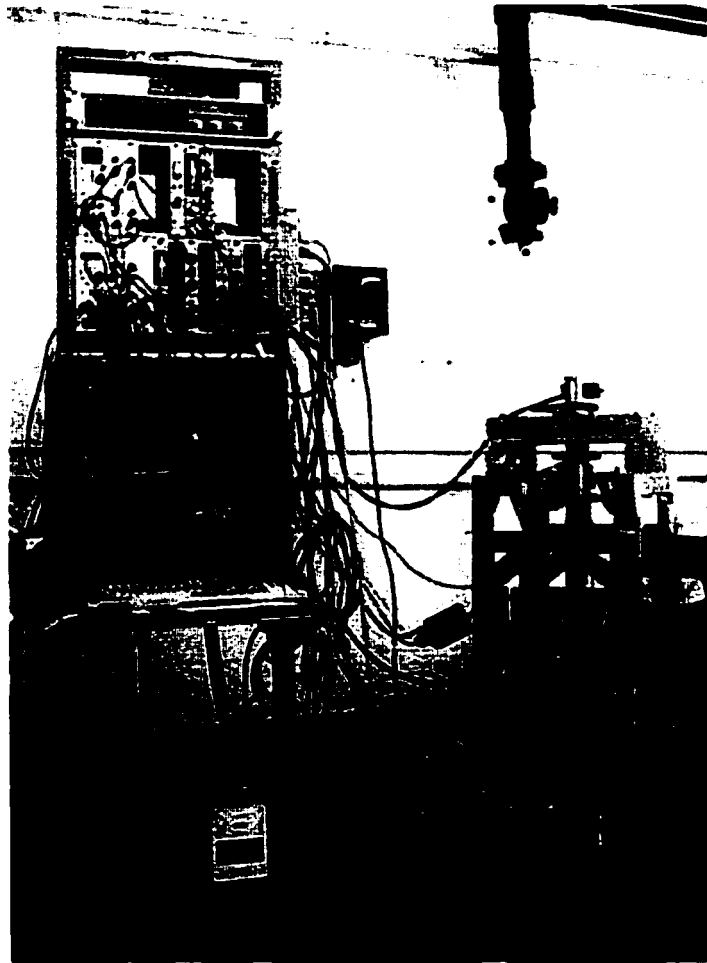
Figure 2.20: Photograph of SEDM apparatus with close cycle refrigeration system.

42

2.3 Muon spin relaxation spectroscopy

Transmission Mössbauer spectra of some materials will show very small line-splittings, where static disorder effectively washes out the sextet. Such a sample may experience time-dependent magnetism (e.g. moment spin flips or transverse spin freezing) which cannot be resolved using the above Mössbauer effect techniques. Pumping a specific sublevel with SEDM when a sextet pattern in a transmission Mössbauer spectrum cannot be clearly resolved is difficult. Moreover, a transmission Mössbauer experiment is sensitive to moment flips that are about or above the Larmor frequency of the Mössbauer nuclei and SEDM is sensitive to moments flips that are about or below the Larmor frequency. Unless transmission Mössbauer spectra lineshapes are clearly due to dynamic phenomena (such as in a ferrofluid), convincing results of time-dependent magnetism may be beyond the time resolution of the SEDM technique.

Another experimental method that is sensitive to magnetic interactions is muon spin relaxation (μSR). The muon is a sensitive local magnetic probe, and zero-field (ZF) μSR provides clear signatures from static and fluctuating moments. Static moments exhibit a Kubo-Toyabe type lineshape in the early time channels in a ZF-μSR spectrum while spin dynamics result in an exponential decay in later time channels. Additionally, the measuring times of Mössbauer effect experiments and μSR overlap, allowing comparison of fluctuation rates.

μSR requires low energy muons as it is necessary that they stop inside a sample of (relatively) convenient thickness ($\sim 200 - 300$ mg/cm^2). Fortunately, the simple two-body decay of charged pions

$$\pi^+ \rightarrow \mu^+ + \nu_\mu \tag{2.4}$$

from which the muon emerges in the rest frame of the pion with a momentum of 29.79 MeV/c and a kinetic energy of 4.119 MeV[92], offers the required energies. Since the neutrino is produced with its spin anti-parallel to momentum, conservation of linear and angular momentum forces the μ^+ to have its spin anti-parallel to its momentum in the rest frame of the pion. Hence, muons emitted from pion decay at

rest are also 100% spin polarized opposite to the direction of their momenta. This is the greatest advantage of μSR as a resonance technique: it begins with a perfectly polarized probe, regardless of the sample into which it is implanted. Muon beams are emitted from π^+ decay at rest in the surface layer of the primary target (at TRIUMF it is graphite) where the pions themselves are produced by collisions of high energy protons with target nuclei. This is why muons used for μSR are often called surface muons.

The positive muon, μ^+, is a spin $\frac{1}{2}$ particle with a half-life of 2.2 μs and magnetic moment of 8.90 μ_N. The muon is an impurity which is implanted into a sample and localizes itself at an interstitial site because of its positive charge. This process occurs very quickly, usually in less than 10^{-9} s[41]. Spin precession is monitored by observing the emitted positron with an energy up to 52 MeV (easily penetrates sample holders, cryostat or ovens, and the detectors used to establish the time and direction of the muon decay) after the muon decays

$$\mu^+ \rightarrow e^+ + \nu_c + \bar{\nu}_\mu \tag{2.5}$$

The decay positron is emitted preferentially along the muon spin direction. Due to the absence of a quadrupolar electric moment (spin $\frac{1}{2}$) the muon does not couple to electric field gradients and is therefore affected only by the local magnetic field, that can be small due to a large gyromagnetic ratio (μ_γ) of $2\pi \times 13.554 \times 10^7$ $T^{-1}s^{-1}$.

There are two basic geometries for a μSR experiment. In the transverse geometry, an external magnetic field is applied perpendicular to the muon beam polarization direction, and the positrons are detected perpendicularly to this external field. In the longitudinal geometry an external magnetic field can be applied along the initial muon beam polarization direction and a longitudinal-field (LF) μSR experiment is possible. If only a very weak external field is applied to compensate for terrestrial magnetic fields or stray fields from the accelerator, this longitudinal geometry can also be used for a zero-field (ZF) μSR experiment. Fig. 2.21 shows a schematic diagram of a longitudinal setup. Positron detectors are placed along the muon beam direction

44
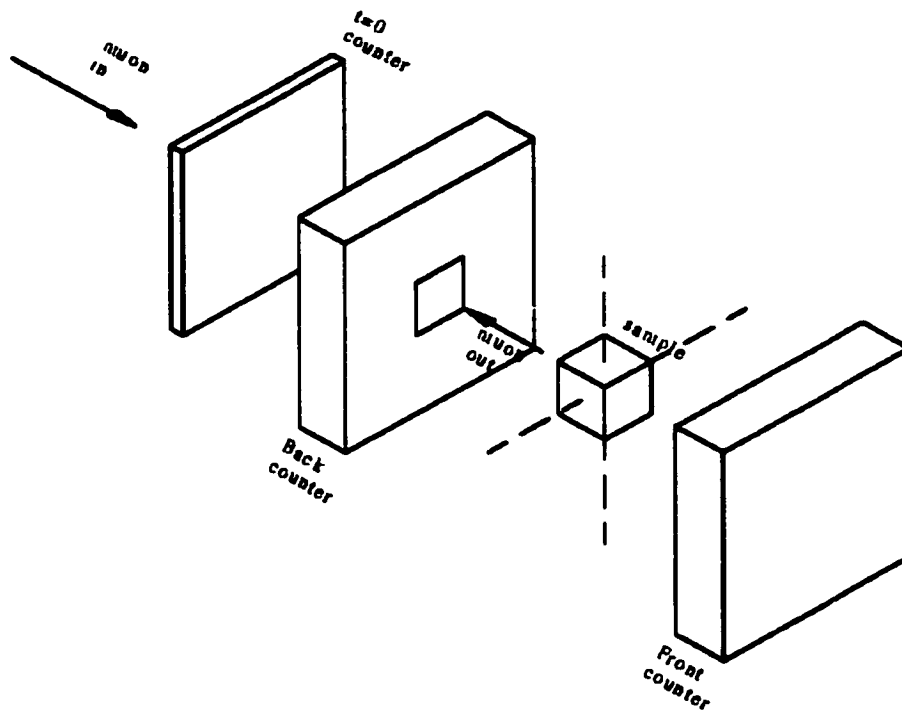
Figure 2.21: A schematic diagram of a longitudinal or zero-field μSR experiment. B = backward detector, F = forward detector.

upstream and downstream of the sample. The backward positron telescope is provided with a hole to allow passage of the incoming muon beam.

The positron detectors are plastic scintillation counters. When an ionizing particle passes through the scintillating plastic, a flash of light is generated and it is transmitted down clear plastic light guides by total internal reflection to a photomultiplier tube. This photomultiplier tube in turn emits an electrical pulse which is transmitted to a fast timing discriminator module. A logical timing pulse with an arrival time $\sim 1 - 2$ ns (and fixed delay by counter electronics) to counting electronics is the end result. Raw counter pulses are fed to fast discriminators which generate uniform timing logic pulses (if the raw pulse height is above a threshold).

An incoming muon generates a pulse in the $t = 0$ counter (Fig. 2.21) which sends a start pulse to a fast time digitizer (clock). When the muon decays it triggers a stop pulse from the front or back counters (Fig. 2.21), and stops the clock. The time interval is recorded in the corresponding bin of a time histogram. Additional logic
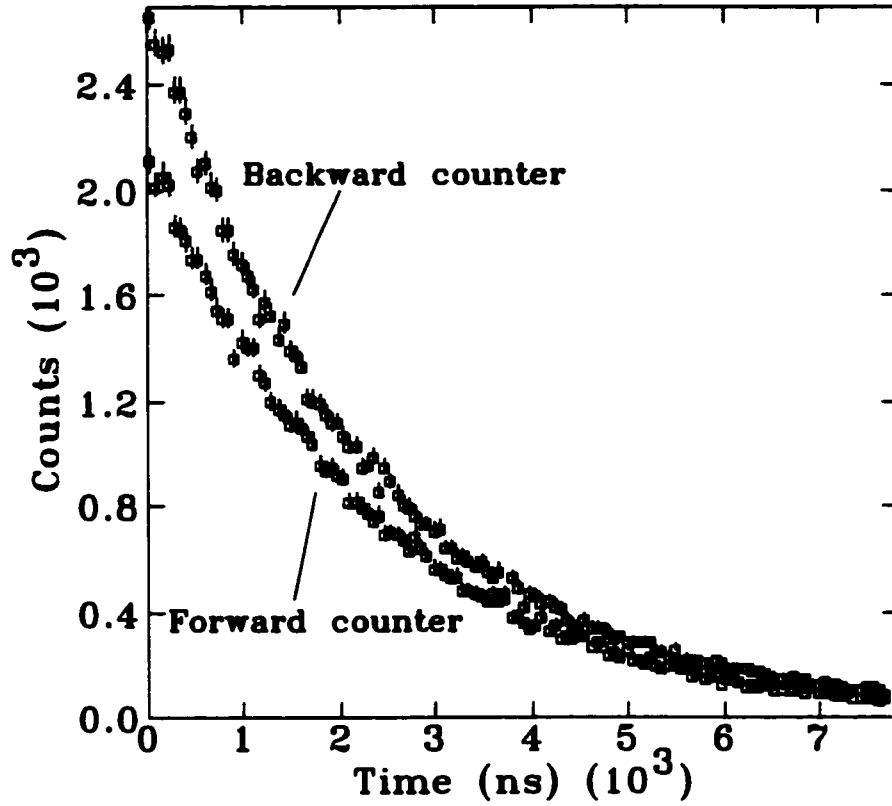
Figure 2.22: A typical μSR decay pattern of the timed histograms collected from the forward and backward counter telescopes.

modules are used to ensure that events that occur with more than one muon in the sample, or possible events which may produce multiple positrons, are not counted.

Fig. 2.22 shows a typical ZF-μSR decay pattern. This depolarization pattern is a function of the muon's lifetime, τ_μ, and the muon spin relaxation function $G_z(t)$. The physics of the muon's behavior in the magnetic sample is contained in $G_z(t)$, which corresponds to the correlation function of muon spins:

$$G_z(t) = 4 < S_z^\mu(0)S_z^\mu(t) > \tag{2.6}$$

The timed histograms collected from the pair of counter telescopes have a fitted form which is, in the most general case:

$$N_{B,F} = b_{B,F} + N_0^{B,F} \exp(-\frac{t}{\tau_\mu}) \times (1 \pm A_0^{B,F} G_z(t)) \tag{2.7}$$

where B denotes the backward counter and F the forward counter. Setting $t = 0$ as the time that the polarized muon stops in the sample, we have $N_{B,F}(t)$ as a measure of

46

the positron counts per unit time bin, $b_{B,F}$ the time dependent random background, $N_0^{B,F}$ a normalizing factor which includes the counts per bin at $t = 0$, and $A_0^{B,F}$ the initial magnitude of the asymmetry of the decay of muons into positrons. That is, $+A_0^B$ corresponds to N_0^B and $-A_0^F$ to N_0^F. These parameters describe the experimental conditions.

At TRIUMF, the time independent background is ascertained by recording the counts for several tenths of a microsecond before $t = 0$. This is achieved by carefully placing a delay in the counting electronics. The background is then subtracted, $B(t) = N_B(t) - b_B$, $F(t) = N_F(t) - b_F$ and an asymmetry histogram is constructed from data from opposing counters as:

$$A(t) = \frac{B(t) - F(t)}{B(t) + F(t)} \tag{2.8}$$

Since, in practice opposing counters are not identical, instrumental parameters $\alpha = N_0^F/N_0^B$ and $\beta = A_0^F/A_0^B$ allow the experimental asymmetry $A(t)$ to be correctly described by

$$A(t) = \frac{(1 - \alpha) + (1 + \alpha\beta)A_0^B G_z(t)}{(1 + \alpha) + (1 - \alpha\beta)A_0^B G_z(t)} \tag{2.9}$$

Usually, Eqn. 2.9 is inverted to yield the so-called corrected asymmetry and the displayed data is given by:

$$A_0^B G_z(t) = \frac{(\alpha - 1) + (\alpha + 1)A(t)}{(\alpha\beta + 1)(\alpha\beta - 1)A(t)} \tag{2.10}$$

and a typical ZF-μSR spectrum of the corrected asymmetry, $A_0^B G_z(t)$, is shown in Fig. 2.23.

The normalization ratio given by α is subject to systematic variations such as an intermittent discriminator in the counting electronics and is rarely very close to unity. The asymmetry ratio β is usually stable and the approximation $\beta \approx 1$ is used, so that $A_0^F \simeq A_0^B \simeq A_0$. If the time-independent backgrounds are not well known, they must be fitted, making it necessary to fit $N_B(t)$ and $N_F(t)$ separately, but simultaneously, with a common $G_z(t)$.

Facilities exist which produce quasi-continuous (e.g. TRIUMF in Canada) or pulsed (e.g. ISIS at the Rutherford Appleton Laboratory in the U.K.) muon beams.
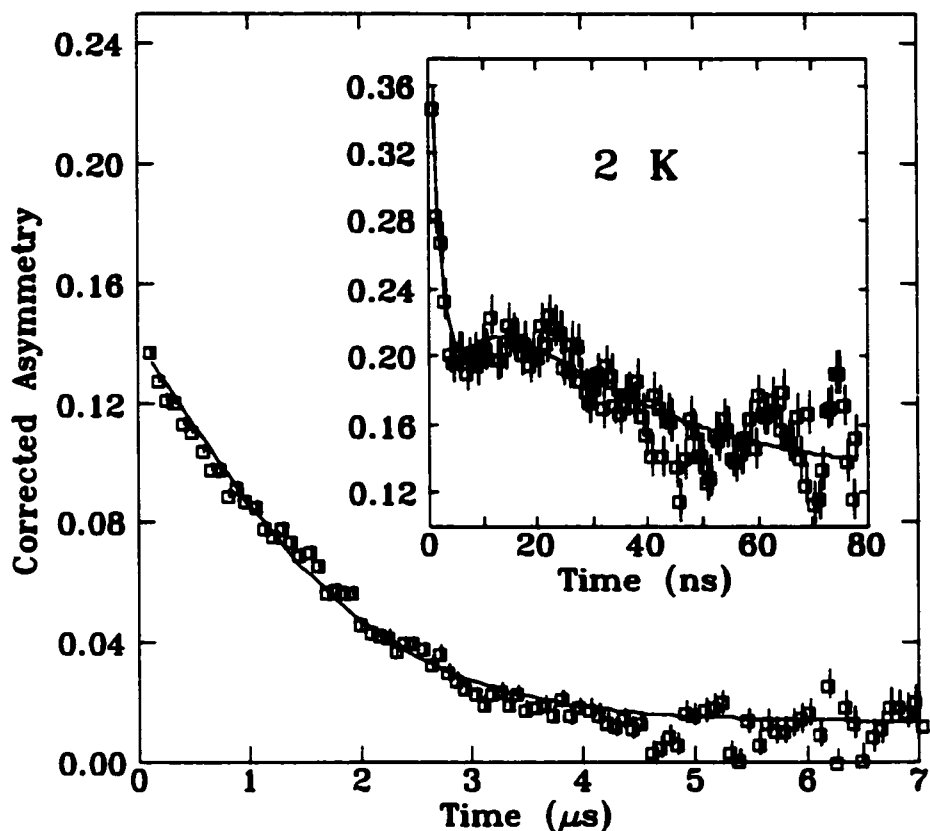
Figure 2.23: ZF-μSR spectrum of a polysaccharide iron complex at 2 K.

Pulsed muon beams are well suited for the study of weak magnetic signals due to an almost complete absence of background related to contamination of the beam with particles other than muons. Pulsed beams have a relatively low time resolution so they are unsuitable for the study of systems exhibiting fast relaxation processes or appreciable local fields (larger than ~50 mT at the muon site[42]). The low time resolution limitation does not apply to the quasi-continuous beams.

At TRIUMF, ZF-μSR measurements were done on the M20 beamline for the polysaccharide iron complex and on the M13 and M20 beamlines for the Fe-Zr systems. The data collection apparatus was the OMNI rig (Fig. 2.24). Sample temperatures were controlled between 2 K and 300 K in a helium flow cryostat. Field-zero was set to better then 1 μT using a flux gate magnetometer for the M20 beamline work, and was set to better than 0.1 mT using a Hall probe and confirmed using the muon precession signal in a pure silver blank for the M13 beamline work. Histograms

containing $1 - 4 \times 10^7$ events were acquired with timing resolutions of either 0.625 ns when well below T_C or 1.25 ns when below T_C up to 300 K.

Figure 2.24: The OMNI rig used for μSR experiments at TRIUMF. The decay positrons (e^+) are detected in one of four scintillation counters placed in the forward and backward directions relative to the incoming beam. The forward and backward detectors are visible at the left and right of the picture (pairs of cylinders attached to the black plates). The (similar) muon arrival detector is also visible at the lower left. The central structure is the cryostat containing our sample, and surrounded by Helmholtz coils to control the magnetic field at the sample.

49

Chapter 3

Lineshape Models

To accurately extract information from spectra, it is necessary to match a theoretical curve to a set of experimental data. In this chapter, various theoretical descriptions of physical phenomena and their effects on spectra are detailed. With these models, non-linear least-squares analysis is applied to the data, and physical properties of the samples obtained.

3.1 Evaluation of transmission Mössbauer spectra for ^{57}Fe

Static magnetic disorder

While transmission Mössbauer spectra of magnetic materials with a unique magnetic hyperfine field are easily described by a single Lorentzian sextet whose absorption peaks are at energies determined from the hyperfine interaction parameters described in Sec. 2.1 with intensities given by the appropriate 3:R25:1:1:R25:3 ratios, spectra of materials with static disorder require a more complicated description. Transmission Mössbauer spectra of magnetic materials with static magnetic disorder are best described by a range of hyperfine parameters that produce subspectra of Lorentzian lineshape which are weighted by a distribution. One method to calculate a distribution of subspectra for a series of hyperfine fields, B_{hf}, is Window's[44] series expansion
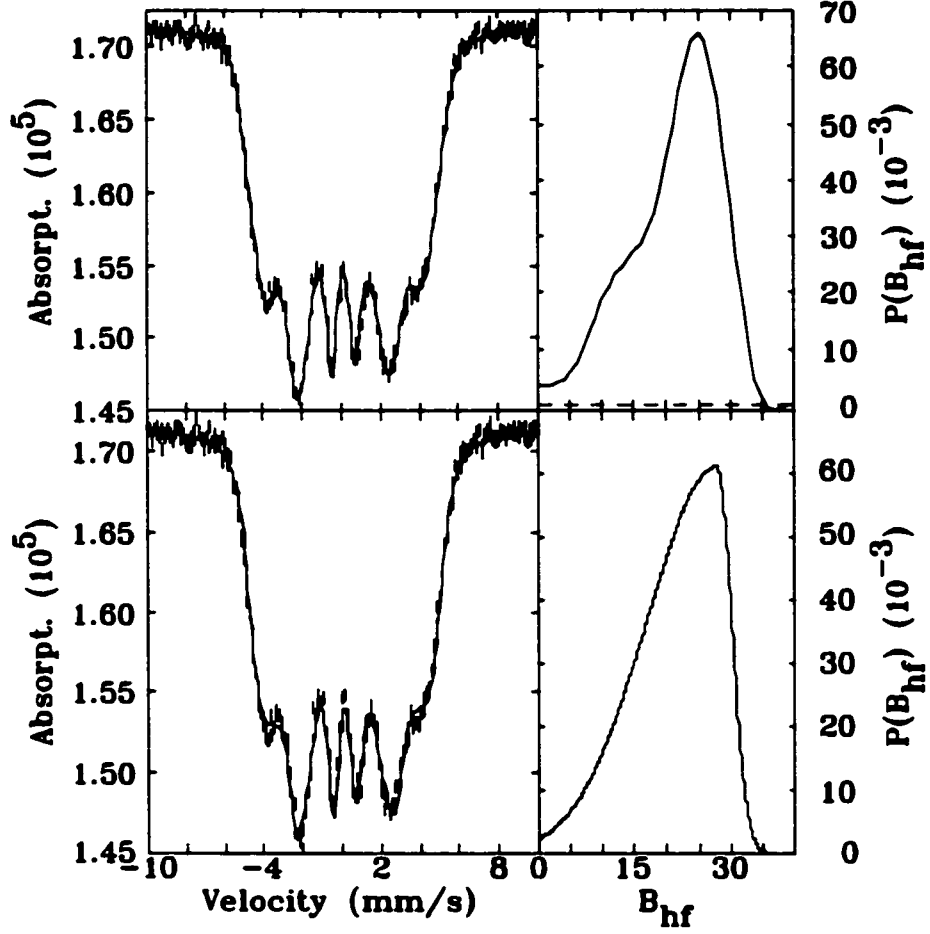
Figure 3.1: A transmission spectrum of $Fe_{92}Zr_8$ at 20 K (left) fit using Window's method (top) and an asymmetric Gaussian hyperfine field distribution (bottom). Hyperfine field distributions (right) calculated with each fitting procedure is also shown.

of the probability function of hyperfine fields, $P(B_{hf})$, given by:

$$P(B_{hf}) = \sum_{n=1}^{N} a_n \cos\left(\frac{n\pi B_{hf}}{B_{hf}^{max} - (-1)^n}\right) \tag{3.1}$$

where a_n is the normalization factor for the distribution, and B_{hf}^{max} is the maximum value of the hyperfine field necessary to describe a spectrum. The power of this method lies in the few assumptions made about $P(B_{hf})$, i.e. only the boundary conditions for the distribution $P(B_{hf}^{max}) = 0$ and $dP/dB_{hf} = 0$ for $B_{hf} = 0$ and $B_{hf} = B_{hf}^{max}$. A linear correlation between isomer shift and hyperfine field is necessary to describe slight asymmetry of the spectrum. Window's method is a standard fitting

algorithm for spectra in the Mössbauer literature, however, careful interpretation of $P(B_{hf})$ is necessary when applying it. Since a finite number of terms N is used to fit spectra (usually between six and ten), oscillatory components in $P(B_{hf})$ can occur, like the $P(B_{hf})$ bump at ~ 10 T in Fig. 3.1. Limiting N to the smallest number which can successfully fit the data is the general procedure for avoiding $P(B_{hf})$ oscillations. Another problem with this procedure is that unphysical, negative $P(B_{hf})$, are sometimes calculated. A fit using this procedure is shown in Fig. 3.1 where $N = 6$ terms were used. Notice the small portion of the calculated $P(B_{hf})$ which is negative for fields above 30 T.

With these limitations in mind, Window's method is a powerful fitting tool. Often it is the only way to consistently fit transmission Mössbauer spectra of materials with static disorder. Used with a subtraction procedure of zero and applied field transmission Mössbauer spectra, it offers a clear way to determine $P(B_{hf})$[22], where ringing components and negative values can be avoided.

To avoid the ringing and negative values of $P(B_{hf})$ from Window's method, a more robust, fixed functional form of $P(B_{hf})$ can be used to fit transmission Mössbauer spectra of many static magnetic amorphous materials. A useful $P(B_{hf})$ distribution is derived from an asymmetric Gaussian function. This functional form has a strong similarity to the $P(B_{hf})$ distributions often generated with Window's method. An example of a fit using an asymmetric Gaussian $P(B_{hf})$ is shown in Fig. 3.1. A linear correlation between isomer shift and hyperfine field is used to describe asymmetry in the spectra. Often, fits with an asymmetric Gaussian $P(B_{hf})$ are as successful at describing the experimental lineshape as Window's methods, with the added advantage of being less sensitive to poorer quality signal-to-noise spectra. Fitted values of average B_{hf} and field correlated isomer shift between both methods generally are in good agreement. Occasionally, this simple functional form for $P(B_{hf})$ cannot quite fit all spectral characteristics, as seen in Fig. 3.1, where is just misses lines #1 and #6. A more complicated combination of Gaussian $P(B_{hf})$'s may be needed[84]. Unfortunately, with a more complicated overall $P(B_{hf})$, the difficulties inherent to Window's
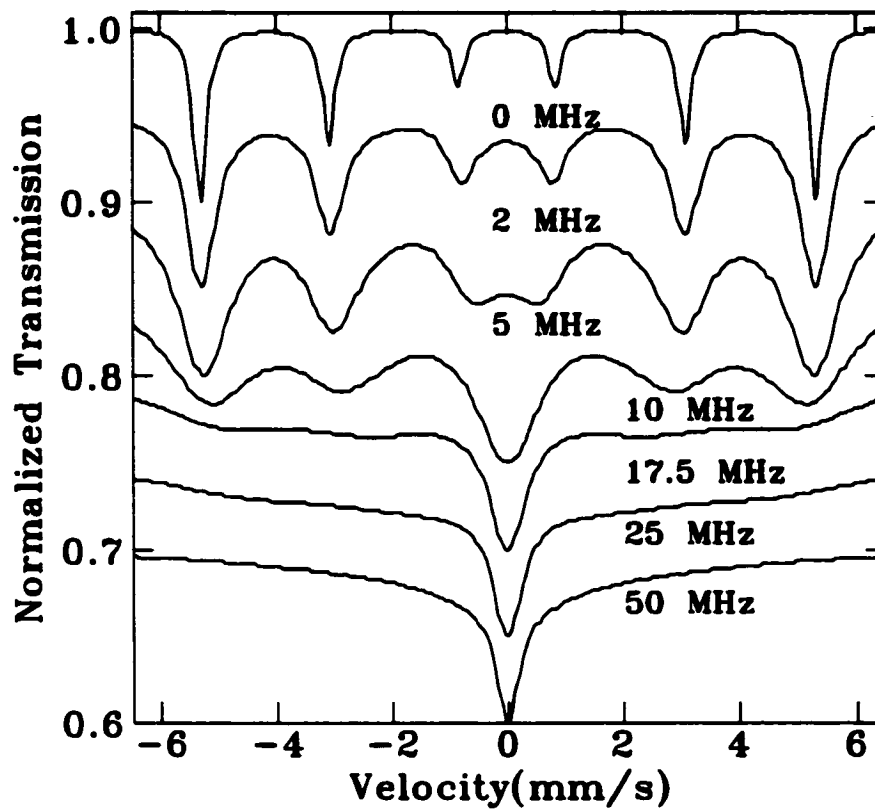
Figure 3.2: Lineshapes for different values of relaxation rate ν. $\Gamma=0.13$ mm/s and $B_{hf}=33$ T.

method are revisited.

Dynamic magnetic disorder

Calculations that describe transmission Mössbauer spectra with static disorder are reasonably straightforward. The physics of hyperfine interactions in Sec. 2.1 with Lorentzian lineshapes correctly describes spectra of static magnetic material. Time-dependent hyperfine interactions add an additional layer of complication to the physics of the Mössbauer nucleus in a magnetic field. The simplest time-dependent effect is when the orientation of a magnetic moment varies by 180° (spin flip) during the Larmor precession time of a Mössbauer nucleus in its excited state.

Magnetic relaxation in simple systems

Transmission Mössbauer spectra of a magnetic material undergoing spin flips are usually modeled using a stochastic two-level lineshape formalism, such as the one by Blume and Tjon[2]. The levels represent the two possible orientations that the moment can make (i.e. $0°$ and $180°$). The transition probabilities per unit time per unit occupation between the two levels are P_{12} and P_{21} where P_{12} denotes the transition from level one to level two and P_{21} the transition from level two to level one. Γ .s the natural linewidth, ω the energy of the incoming γ-ray and $\pm\delta$ the energies of the two levels (determined from the hyperfine interaction energies). We can use the well known lineshape expression[2]

$$I(\omega) = 2\Re \left[\frac{\imath(\omega' + \eta\delta) + 2R}{(\delta^2 - \omega'^2) + 2R(\omega' - \eta\delta)} \right] \tag{3.2}$$

where $\omega' = \omega - \imath\Gamma$, $\eta = (P_{21} - P_{12})/(P_{21} + P_{12})$ and $2R = P_{12} + P_{21}$. The real ($\Re$) component of the expression is used to predict spectra exhibiting simple moment reversals. The probability of the moment being oriented in either a 0 or $180°$ manner is described by the relaxation rate (i.e. the product of the transition probability per unit time and the occupation probability). The rate between level one and two is $\frac{1}{2}P_{12}$, and between level two and one is $\frac{1}{2}P_{21}$. The total relaxation rate is $R = \frac{1}{2}P_{12} + \frac{1}{2}P_{21}$. $R = \nu = 1/\tau$ with τ the relaxation time between moment flips. The lineshape for each line pair of the spectrum (i.e. lines #1 and #6, lines #2 and #5, and lines #3 and #4) are calculated with Eqn. 3.2 with the hyperfine parameters (e.g. δ and B_{hf}) calculated using the expressions in Sec. 2.1 and the correct 3:R25:1:1:R25:3 line intensities.

The effects of simple magnetic relaxation are shown in Fig. 3.2 (powder average). For slow relaxation, the lineshape is the same as for a static field, except for the slight broadening of the lines. As the relaxation rate increases, the lines spread out more until at fast relaxation rates, magnetic effects are time-averaged and gradually go to zero, leaving a single line in the center.

This simple magnetic relaxation model can be used to describe transmission Mössbauer

spectra of crystalline magnetic materials, such as $Fe_{65}Ni_{35}$[14] and bulk Fe_2O_3[56]. The model can also correctly describe the magnetic behavior of a superparamagnetic single domain particle.

Describing the behavior of a single domain particle as it changes from superparamagnetic (180° spin flips) on towards begin blocked at much lower temperatures, and it's effects on transmission Mössbauer spectra, is much more involved (and up to now has not been properly done). Unfortunately, one single domain particle cannot be studied with transmission Mössbauer spectroscopy (the holy-grail of fine particle magnetism is to create a single-sized single domain particle system), and a real magnetic fine particle system consists of a collection of single domain particles with a distribution of particle sizes. The following model correctly described the entire range of magnetic behavior in a fine particle system.

Magnetic fine particle systems

When describing magnetic fine particle systems, it is usually assumed that the particles are uniaxially anisotropic since even a small departure from sphericity will result in a strong uniaxial shape anisotropy[8]. The internal magnetic potential energy of a particle's average magnetic moment can then be described by the expression $E = -KV \cos^2(\theta)$, where K is the anisotropy constant of the particle, V its volume and θ the angle between the easy axis of the particle and the direction of magnetization.

At low temperatures, the moment of a single domain particle is fixed along its easy axis, in a blocked state. The moment will remain blocked until the thermal energy is great enough to allow it to oscillate about its easy axis. These oscillations, called collective excitations, occur until the thermal energy increases to the point where the moment can undergo 180° moment flips. At this temperature and above, the moment is superparamagnetic.

The moment oscillations during collective excitations can be viewed as the moment

rocking in its potential well. Mørup[1] modeled this behavior by assuming that the fluctuations around the easy axis occur much faster than the Larmor precession of the Mössbauer atoms. The probability of the moment being at an angle away from the easy axis is calculated, resulting in a correction to the magnetic hyperfine field. For the case of a uniaxially symmetric particle this is:

$$B_{obs} = B_{hf} \left(1 - \frac{k_B T}{2KV} \right) \tag{3.3}$$

where B_{obs} is the observed magnetic hyperfine field at the temperature T and B_{hf} is the static magnetic hyperfine field. Combining this with a distribution of particle sizes, each with a different V, yields an effective hyperfine field distribution which successfully predicts low temperature spectra of fine particle systems.

The success of Mørup's description of low temperature fine particle Mössbauer spectra is shown in Fig. 3.3. With the log-normal particle size distribution of the 4.5 nm ferrofluid, 12 K, 20 K and 25 K spectral lineshapes calculated with Eqn. 3.3 are in excellent agreement with experiment. Linewidths are constant, 0.42 ± 0.02 mm/s, and $B_{hf}=50.0 \pm 0.2$ T is consistent with the accepted value for Fe_3O_4[4, 59]. $K=3.3 \pm 0.2$ x 10^4 J/m^3 is in agreement with K of similar fine particle systems[51, 52, 53] and a more complete lineshape model[59]. Above 25 K, this simple description fails since collective excitations are no longer the only magnetic fluctuation present. A central, non-magnetic, component develops that cannot be described by the collective excitation model. Furthermore, there are increases in both the fitted linewidth (shown in Fig. 3.4 by the $\triangledown$) and B_{hf}, and a decrease of K.

At high temperatures, where $KV \ll k_B T$ and rapid reversals of the magnetic moment occur, spectra are usually modeled using a stochastic two level lineshape formalism, such as the one by Blume and Tjon (Eqn. 3.2). There is an equal probability of the moment being oriented in either a 0° or 180° manner with respect to the easy axis. This assumption is consistent with a single domain particle's moment not having a preferred orientation along its easy axis (the potential barrier E is symmetric). In Eqn. 3.2, $P_{21} = P_{21} \equiv P$ and the total relaxation rate is $R = \frac{1}{2}P + \frac{1}{2}P$.

56
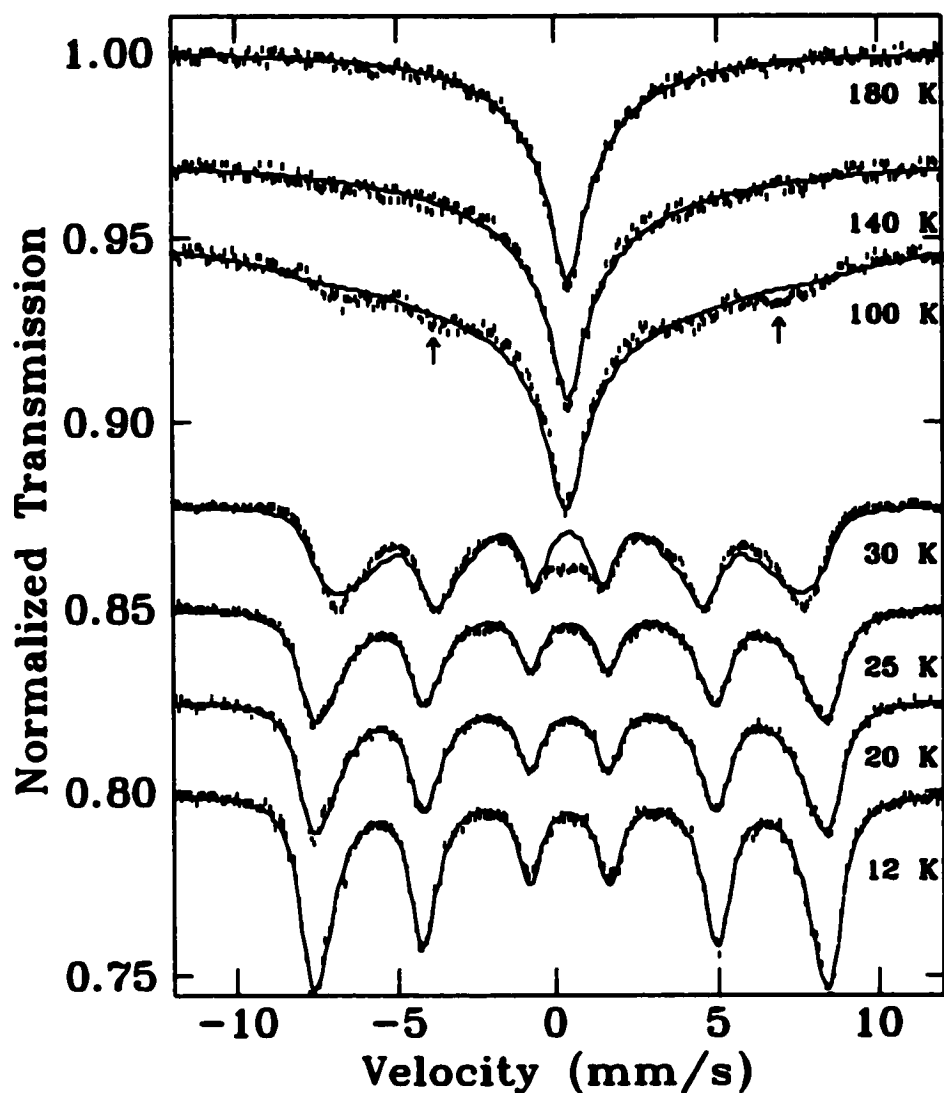
Figure 3.3: Fits to the 4.5 nm Fe_3O_4 ferrofluid using Mørup's collective excitation description for low temperature spectra and a two-level relaxation model for the high temperature spectra. These models clearly fail to predict the lineshape of the intermediate temperature spectra.

The wide range of particle sizes in a real system leads to a large variation of energy barriers. Spectrum modeling hinges upon the calculation of superparamagnetic moment behavior, effectively described by the relaxation time, τ. A valid expression of τ for all possible energy barrier sizes is therefore critical. Typically, a relation along the lines of $\tau = \tau_0 \exp(\alpha)$ is used, where $\alpha = KV/kT$ and τ_0 essentially depends upon the non-relaxing saturation magnetization[4, 64]. This approach is valid for $\alpha \gg 2$.
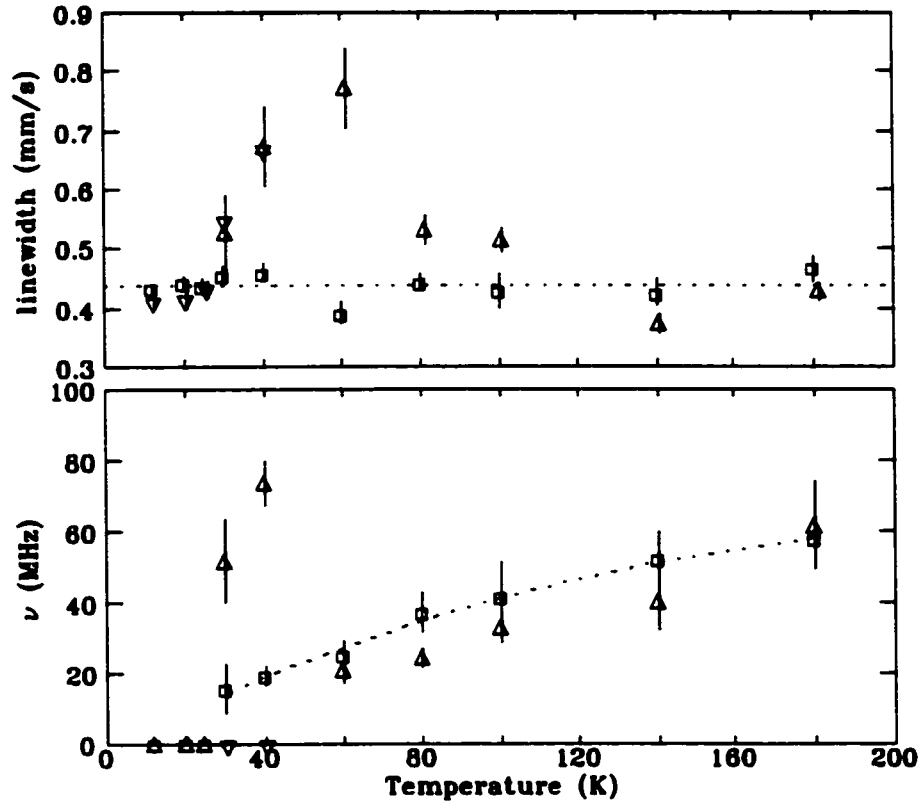
Figure 3.4: Results of fits of the 4.5 nm Fe$_3$O$_4$ ferrofluid using Mørup's collective excitation description ($\triangledown$), a two-level relaxation model ($\triangle$) and our multi-level formalism ($\square$). Relaxation rates, ν, were averaged over the log-normal particle size distribution.

This is the mathematical limit used to find the solution of the Fokker-Plank equation for a moment flip in an axially symmetry potential describing the relaxation process. See section D.3 of Ref. [4] for more details. At high temperatures (or for small moment sizes) Mössbauer spectroscopy measures moments with relaxation times in the $\alpha < 2$ regime[4]. Using an invalid expression for τ will result in an incorrect assessment of K and improperly scale the relaxation times for particles at the extremes of the size distribution. Coffey et al.[48] have determined an expression for the relaxation time

$$\tau = \tau_0 \frac{1}{4\alpha} \frac{1}{\frac{\alpha}{\alpha+1}\sqrt{\frac{\alpha}{\pi}} + 2^{-\alpha-1}}[\exp(\alpha) - 1] \qquad (3.4)$$

with $\tau_0 \propto VM_s$ where M_s is the saturation magnetization. This expression is valid to within a few percent of the exact analytic solution[4], for any value of α. It ensures that

a correct τ for each particle size is calculated and a consistent K for each temperature determined when modeling data.

The two level formalism with a log-normal particle size distribution and τ given by Eqn. 3.4 with $E = -KV\cos^2(\theta)$ results in an adequate description of the 180 K and 140 K 4.5 nm ferrofluid spectra, shown in Fig. 3.3. Fitted results in Fig. 3.4 show that the linewidths (denoted by $\triangle$) are reasonably consistent and the expected decrease of relaxation rate with temperature occurs. For the highest temperature spectra it was necessary to fix the zero-temperature hyperfine field to 50 T to avoid cross-correlations between the least-squares fitted relaxation rate, linewidth and hyperfine field. K could not be fit reliably and was fixed at 3.0×10^4 J/m^3. The fit quality quickly deteriorates on cooling as a static component develops (notice the arrows displaying the missed components of the experimental 100 K spectrum in Fig. 3.3) and it was necessary to let B_{hf} and K vary to fit the experimental spectra. Linewidths increase, with K and B_{hf} changing by as much at 50% to fit the spectra. As T_B is approached, the fitted relaxation rate *increases* in stark contrast with the actual slowing of the relaxation rate. This simple two-level model cannot predict the magnetic behavior of a fine particle system at intermediate temperatures.

At intermediate temperatures moments from the largest particles will be blocked. However, there is enough thermal energy for moments from medium-sized particles in the distribution to undergo collective excitations, and moments from smaller particles will be superparamagnetic. The models for collective excitations and spin flipping cannot correctly predict the transmission Mössbauer spectral lineshapes (Fig. 3.3).

At these intermediate temperatures, moments experience a variety of orientations. The many-level representation of Jones and Srivastava[47] offers the best way to model the complex dynamic behavior of single-domain particles. Computer hardware readily available at the time of their publication was not powerful enough for convenient least-squares fitting using this approach. Increases in processor power over the last few years allow for reasonable computation times for fitting spectra. This many-level model fully describes the effects of the various tilt angles that the moment can make. Collective

59

excitations, interparticle interactions and superparamagnetism are described within a single formalism[50]. Sack's[54] simplification of Anderson's[55] stochastic quantum mechanical model is used as a starting point:

$$I(\omega) = 2\Re(\mathbf{W}\underline{M}^{-1}\vec{1}).\tag{3.5}$$

It is assumed that the nuclear states are constant and the relaxation problem can be solved separately for each line pair, i.e. transitions from $|I_1 m_1 >$ to $|I_0 m_0 >$ where $I_1 = \frac{3}{2}$ and $I_0 = \frac{1}{2}$, displayed schematically in Fig. 2.2. The N components of the row vector $\mathbf{W}$ are proportional to the occupation probabilities of the states in equilibrium, $\vec{1}$ is a column vector with all its components equal to unity and $\underline{M}=(\imath\omega+\Gamma)\underline{I}-\imath\Omega-\Pi$ is the matrix which contains the physical description of the system. This description involves the line positions in the absence of relaxation, ω_i, which are components of the diagonal matrix Ω, and the natural linewidth Γ. The transition probability per unit time per unit occupation of state i, from state i to state j is given by $\Pi_{ij} = P_{ij}, \Pi_{ii} = -\sum_j P_{ij}$ $(i \neq j)$. For a two level system, this gives:

$$I(\omega) = 2\Re\left[\frac{(P_{21}, P_{12})}{P_{12}+P_{21}}\left[\begin{matrix} \imath(\omega-\delta)+P_{12}+\Gamma & -P_{21} \\ -P_{21} & \imath(\omega+\delta)+P_{21}+\Gamma \end{matrix}\right]^{-1}\left[\begin{matrix}1\\1\end{matrix}\right]\right]\tag{3.6}$$

and solving yields Eqn. 3.2.

This formalism can be extended to characterize the many orientations that the moment of a single-domain particle may take when it is thermally agitated at intermediate temperatures. Consider a particle to have S possible orientations. The possible angles between 0 and 180° are expressed by k steps from one to $(2S+1)$ so $\theta_k = \frac{\pi}{2}(\frac{k-S-1}{S})^2$. The magnetic hyperfine field distribution of Mørup's model is emulated by the resulting line positions $\omega_k = (S-k+1)\delta/S$ with 2δ the magnetic hyperfine splitting between line pairs. The occupation probabilities of the levels W_i and transition probabilities per unit time between levels P_{ij} are necessary to solve Eqn. 3.5. The equilibrium populations can be described using a Boltzmann distribution, $W_k = \exp(-E_k/kT)$ so that detailed balance is conserved, and we discretize the potential barrier describing the uniaxial particle with $E_k = -KV\cos^2(\theta_k)$. $\underline{M}$ is given

60

by:

$$M_{kk} = i(\omega - \omega_k) + \Gamma - M_{kk-1} + M_{kk+1} \qquad (3.7)$$

with

$$M_{kk+1} = -P_{kk+1}[\exp(-\Delta E/kT)] \qquad k < (2S+1)/2 \qquad (3.8)$$

$$M_{kk-1} = -P_{kk-1}[\exp(-\Delta E/kT)] \qquad k \geq (2S+1)/2 \qquad (3.9)$$

where the Boltzmann factor is used only for a step 'up' to a higher energy level during the random walk of the magnetization vector. Also $\Delta E = E_k - E_{k\pm1}$ and

$$P_{kk+1} = R[S(S+1) - (k-S-1)(k+S)] \qquad k < (2S+1)/2 \qquad (3.10)$$

$$P_{kk-1} = R[S(S+1) - (k-S-1)(k+S-2)] \qquad k \geq (2S+1)/2 \qquad (3.11)$$

where R is the relaxation rate between levels.

Eqn. 3.5 is then solved with inversion of $\underline{M}$ necessary for each ω of the simulated spectrum.

The moment relaxation rate must be carefully defined in contrast to the simple two level situation. There are multiple angles to which the moment can relax to and from, instead of just 0 and 180°, so the minimum and maximum orientation change of the moment during the relaxation process must be defined. In this case, the relaxation rate is the product of the occupation probability of the particle's initial level before the orientation change occurs and the transition probability per unit time between the two levels. This rate must be summed for all components of the random walk from initial to final orientation. For example, the average 180° flip rate is given by:

$$\nu = \sum_{i=1}^{2S} W_i P_{ij}/(2S+1) \qquad (3.12)$$

To complete the model, a distribution of particle sizes and an expression for the fluctuation rate between moment orientations, R, is necessary. Our description of a magnetic fine particle system assumed a log-normal particle size distribution. We used Eqn. 3.4 for R. With a least-squares fitting routine the following parameters were used to fit spectra: Baseline, Γ, intensity, B_{hf}, isomer shift, τ_0 and K. Fig. 3.4 shows

61

that, at high temperatures, our model generates the same behavior as the two-level formalism, while at low temperatures, collective excitations are correctly described. We will use this model to properly describe the magnetism in several fine particle systems.

3.2 Evaluation of selective excitation double Mössbauer spectra

The description of a scattering Mössbauer experiment is much more involved than for a transmission Mössbauer experiment. It is necessary to establish a formalism to describe the resonant scattering that occurs during a selective excitation double Mössbauer (SEDM) experiment where only a single transition is driven, and two resonant Mössbauer events occur during the measurement. Bohdan Balko and Gilbert R. Hoy have developed a complete description of the SEDM process in a sample with a single, static B_{hf}[17]. This model calculates the energy distributions of scattered radiation from sample and energy analyzer, and integrates these energy distributions to describe the effects of sample thickness, determining the line absorptions(a single-line $Na_4Fe(CN)_6 \cdot 10H_2O$ absorber attached to the CAD with a standard proportional counter behind it[16, 17] was used in the SEDM apparatus). This approach was necessary to include sample thickness effects (SEDM was performed on a $\sim$5 cm thick iron bar as well as a bulk α-Fe_3O_2 crystal). The SEDM experiments reported here were on very thin metal alloys (melt spun ribbons $\sim$0.1 mm thick) and two ferrofluids with low iron content[34]. No thickness effects were observed in transmission Mössbauer or SEDM spectra. Additionally, since we performed SEDM experiments on samples with static disorder, it was necessary to use a SEDM lineshape model which was valid for a range of B_{hf}'s. A simpler description assuming Lorentzian lineshapes for the SEDM spectra of thin samples was devised which could be combined with a $P(B_{hf})$.
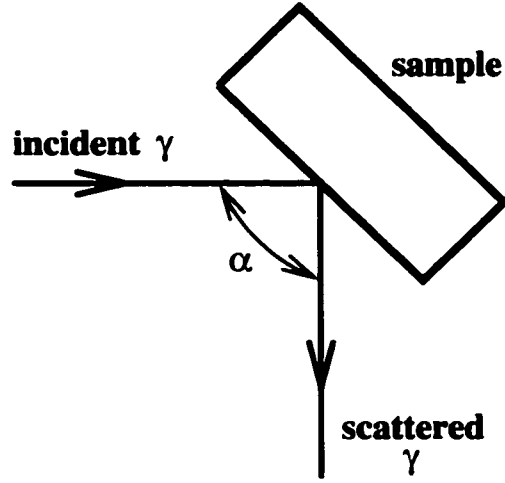
Figure 3.5: Sample orientation relative to the incident and scattered radiation directions in a SEDM experiment.

Time-independent results

There are two energies which describe a SEDM experiment. One is the CVD transducer velocity which defines the energy of the populated sublevel in the sample. The other is the velocity of the CAD during its energy analysis of scattered radiation from the sample. In analyzing a SEDM experiment it is important to know the energy distribution of the source radiation, the energy distribution of the scattered radiation from the sample and the energy resolution of the detector. These items are characterized by the linewidths of these processes.

When a material with a single, static hyperfine field is examined using SEDM, the lineshape is described by the expression:

$$I(E,S) = \frac{(\Gamma_D/2)^2}{E^2 - (\Gamma_D/2)^2} \times (\sum_{i=1}^{6} \frac{W_{i,i}(\alpha)(\Gamma/2)^2}{(E - E_i)^2 + (\Gamma/2)^2} \frac{(\Gamma_b/2)^2}{(E - S)^2 + (\Gamma_b/2)^2}$$

$$+ \sum_{i=2}^{3} \frac{W_{i,i+2}(\alpha)(\Gamma/2)^2}{(E - E_{i+2} - G)^2 - (\Gamma/2)^2} \frac{(\Gamma_b/2)^2}{(E - S - G)^2 + (\Gamma_b/2)^2}$$

$$+ \sum_{i=2}^{3} \frac{W_{i+2,i}(\alpha)(\Gamma/2)^2}{(E - E_{i+2} + G)^2 - (\Gamma/2)^2} \frac{(\Gamma_b/2)^2}{(E - S + G)^2 + (\Gamma_b/2)^2})$$

(3.13)

where S is the CVD velocity, E the CAD velocity and E_i the energy of each spectral line (see Fig. 2.2), and $G = E_4 - E_2$. Γ_b represents the linewidth of the source, Γ

63

the lifetime of the excited state and Γ_D is the instrumental linewidth of the CED (or more generally, the energy analyzer). $W(\alpha)$ represent the angular distribution of resonantly scattered radiation, where $\alpha = 90°$ is the scattering angle (Fig. 3.5). For a powder sample we have[17]

$$W_{1,1} = W_{6,6} = \left(\frac{3}{8\pi}\right)^2 \frac{1}{4}\left(\frac{26 + 2\cos^2(\alpha)}{15}\right) \tag{3.14}$$

$$W_{2,2} = W_{5,5} = \left(\frac{3}{8\pi}\right)^2 \frac{4}{9}\left(\frac{6 + 2\cos^2(\alpha)}{15}\right)$$

$$W_{3,3} = W_{4,4} = \frac{1}{9}W_{1,1}$$

$$W_{2,4} = W_{4,2} = W_{3,5} = W_{5,3} = \left(\frac{3}{8\pi}\right)^2 \frac{1}{9}\left(\frac{14 - 2\cos^2(\alpha)}{15}\right)$$

which is appropriate when describing the SEDM spectra of the ferrofluids, as the moments are frozen in a random orientation in the carrier-liquid at temperatures below $\sim$200 K (R25=2). For the α-Fe foil and melt-spun ribbon samples, a bulk magnetization direction results in transmission Mössbauer spectra with a R25$\neq$ 2. It is not possible to calculate the W's for this more complex situation. Determining W becomes a difficult structure problem where at least three transmission Mössbauer spectra need to be collected with the incident γ-rays at different orientations with respect to sample[25]. For these experiments, the SEDM sample was always mounted with the ribbons horizontal with respect to the incident γ-rays or, for the α-Fe foil, its rolled direction horizontal with respect to the incident γ-rays. Using the 3:R25:1:1:R25:3 ratios from transmission Mössbauer spectra fits to denote $W_{1,1}{:}W_{2,2}{:}W_{3,3}{:}W_{4,4}{:}W_{5,5}{:}W_{6,6}$ correctly described the SEDM spectra.

When describing a SEDM spectrum of a sample with static disorder, additional information is required. The distribution of hyperfine fields, $P(B_{hf})$, determined from a transmission Mössbauer spectrum allows the various energies of a selected sublevel to be calculated for each hyperfine field in $P(B_{hf})$. The source linewidth, Γ_b, determines the range of transitions which can be pumped. The continuum of B_{hf}'s in the sample are approximated by a series of SEDM sub-spectra, one for each B_{hf} in the distribution from a transmission Mössbauer spectra fit, weighted by $P(B_{hf})$.

This correctly describes a SEDM spectrum of a material with static disorder. It is given by:

$$I(E, S) = \sum_{B_{hf}=0}^{B_{hf}^{max}} P(B_{hf}) \times \frac{(\Gamma_D/2)^2}{E^2 - (\Gamma_D/2)^2} \times \tag{3.15}$$

$$\left(\sum_{i=1}^{6} \frac{W_{i,i}(\alpha)(\Gamma/2)^2}{(E - E_i)^2 + (\Gamma/2)^2} \frac{(\Gamma_s/2)^2}{(E - S)^2 + (\Gamma_s/2)^2} \right.$$

$$+ \sum_{i=2}^{3} \frac{W_{i,i+2}(\alpha)(\Gamma/2)^2}{(E - E_{i+2} - G)^2 - (\Gamma/2)^2} \frac{(\Gamma_s/2)^2}{(E - S - G)^2 + (\Gamma_s/2)^2}$$

$$\left. + \sum_{i=2}^{3} \frac{W_{i+2,i}(\alpha)(\Gamma/2)^2}{(E - E_{i+2} + G)^2 - (\Gamma/2)^2} \frac{(\Gamma_s/2)^2}{(E - S + G)^2 + (\Gamma_s/2)^2} \right)$$

Time-dependent results

To describe SEDM spectra of a system with magnetic relaxation, we must limit ourselves to an approach which is valid only for excitation on resonance. The more general case of a scattering lineshape with time dependent fields has not yet been solved.

To facilitate comparison of relaxation rates obtained with the models for magnetic relaxation which we have applied to transmission spectra, we start with the line shape function Eqn. 3.5 and use:

$$I(E, E_i) = 2\Re(\mathbf{W}\underline{M}^{-1}\vec{1}). \tag{3.16}$$

with

$$W = \begin{pmatrix} P_1 \\ P_2 \end{pmatrix}, \quad M = \begin{pmatrix} -i(E + E_i) + R + \Gamma/2 & -R \\ -R & -i(E - E_i) + R + \Gamma/2 \end{pmatrix} \tag{3.17}$$

where $R = \nu$ is the relaxation rate between states, E is the energy of the scattered radiation, E_i is the line energy and Γ is the linewidth of the excited states in the sample. $I(E)$ describes the scattered radiation from the sample. Unlike the transmission situation, in a SEDM experiment, the initial and final populations of the two (or more) excited states during the time-dependent process must be averaged over the lifetime of the Mössbauer nucleus. Since we are using a Markovian argument to describe the relaxation process, if one state is initially populated and we consider either state to
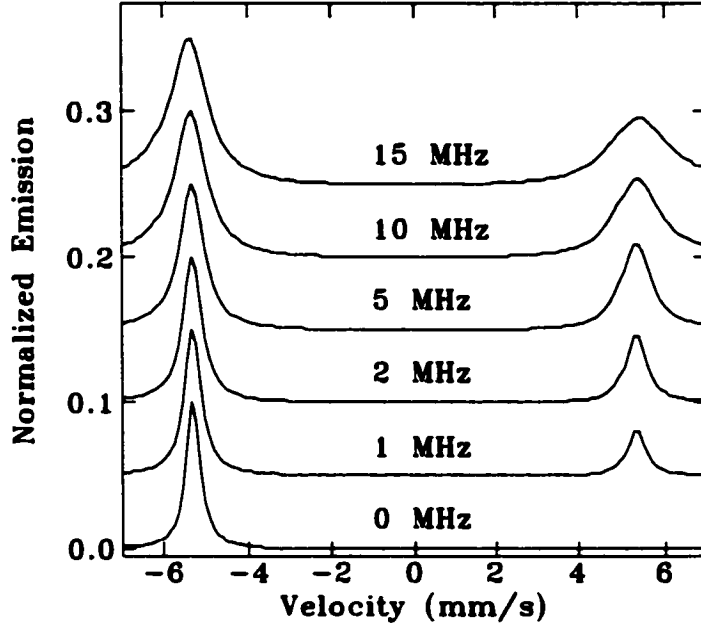
Figure 3.6: Lineshapes for different values of relaxation rate ν with equal populations between the two levels ($k = 1$).

be equally likely at equilibrium, we have an initial estimate of the populations for the two levels (i.e. corresponding to $+h$ and $-h$) given by[67]

$$P_1 = \frac{1}{2}(1 + \exp(-2Rt))$$

$$(3.18)$$

$$P_2 = \frac{1}{2}(1 - \exp(-2Rt))$$

We see that as P_1 decreases, P_2 increases with time until each are $\frac{1}{2}$. Averaging over the nuclear lifetime[17, 67], we have

$$P_1 = \frac{R + \Gamma/2}{2R + \Gamma/2}$$

$$(3.19)$$

$$P_2 = \frac{R}{2R + \Gamma/2}$$

which defines our W in Eqn. 3.17.

The result of the lineshape for relaxation between two sublevels is:

$$I(E, S) = \frac{(\Gamma_D/2)^2}{E - (\Gamma_D/2)^2} \times$$

$$(3.20)$$

$$\left(\sum_{i=1}^{6} I(E, E_i) \times \frac{W_{i,i}(\alpha)(\Gamma_b/2)^2}{(E-S)^2 + (\Gamma_b/2)^2} + \right.$$

$$\sum_{i=2}^{3} I(E, E_i) \times \frac{W_{i,i+2}(\alpha)(\Gamma_b/2)^2}{(E - S - G)^2 + (\Gamma_b/2)^2} +$$

$$\left. \sum_{i=2}^{3} I(E, E_i) \times \frac{W_{i+2,i}(\alpha)(\Gamma_b/2)^2}{(E - S + G)^2 + (\Gamma_b/2)^2} \right)$$

In Fig. 3.6 we show the final SEDM lineshapes for different values of the relaxation rate, ν. In general, the difference in the two peak heights depends on the ratio of the relaxation rate to the nuclear lifetime (ν/Γ) and the lines will be broadened according to the ratio of the relaxation rate to the energy splitting (ν/E_i), just as in ordinary transmission results.

If a sample exhibits both static disorder and magnetic relaxation, a series of sub-spectra based on the above SEDM relaxation lineshape description for each B_{hf} of the static distribution weighted by $P(B_{hf})$ (obtained from a transmission Mössbauer spectrum fit) will describe the SEDM spectra. This combination of static disorder with magnetic fluctuations will be necessary, e.g. to characterize SEDM spectra of a frustrated magnet at temperatures where transverse spin freezing happens, and may be needed to characterize spin dynamics in a spin-glass. The lineshape calculation is give by

$$I(E, S) = \sum_{B_{hf}=0}^{B_{hf}^{max}} P(B_{hf}) \times I_{relax}(E, S) \tag{3.21}$$

where $I_{relax}(E, S)$ is given by Eqn. 3.20. The relaxation effects combined with a distribution of hyperfine fields will increase the SEDM linewidth for a given relaxation rate.

3.3 Evaluation of zero-field muon spin relaxation spectra

The third experimental technique which was used to measure static and dynamic disorder in frustrated magnets and a magnetic fine particle system was zero-field muon

spin relaxation (ZF-μSR). Unlike a Mössbauer nucleus that experiences a time dependent moment fluctuation (e.g. collective excitation or moment flip), the muon, being a spin $\frac{1}{2}$ particle at an interstitial site in the magnetic material, will experience static and dynamic magnetic effects through exchange interactions with the local magnetic field. The magnetism due to these exchange interactions will have the same character as that measured by Mössbauer nuclei in a sample. This allows direct comparisons to be drawn between the spectral signatures of static and dynamic magnetic behavior in Mössbauer spectra and μSR spectra. μSR lineshapes for disordered materials will be described.

A disordered magnetic material will contain many interstitial sites into which a muon can localize itself. This large variation of muon sites (Fig. 3.7) and the effect it has on a μSR spectrum allows the magnetic field which the muons are exposed to be described by a Gaussian distribution of local fields $\vec{H}$:

$$P_G(H_i) = \frac{\gamma_\mu}{(2\pi)^{1/2}\Delta} \exp\left(-\frac{\gamma_\mu^2 H_i^2}{2\Delta^2}\right) \quad i = x, y, z \qquad (3.22)$$

where $\Delta^2/\gamma_\mu^2 = \langle H_x^2 \rangle = \langle H_y^2 \rangle = \langle H_z^2 \rangle$ and $\gamma_\mu = 2\pi \times 1.3554 \times 10^8 \text{s}^{-1}\text{T}^{-1}$.

For static magnetic fields about a muon, when the muon stops at $t = 0$ with its spin pointing in the z direction, the spin evolves in time as

$$\sigma_z(t) = \frac{H_z^2}{H^2} + \frac{H_x^2 + H_y^2}{H^2} \cos(\gamma_\mu H t) \qquad (3.23)$$
$$= \cos^2(\theta) + \sin^2(\theta) \cos(\gamma_\mu H t)$$

where θ is the polar angle of $\vec{H}$ with respect to the z axis.

The muon spin relaxation function for zero external longitudinal field is the statistical average of $\sigma_z(t)$,

$$G_z(t) = \int \int \int \sigma_z(t) P_G(H_x) P_G(H_y) P_G(H_z) \, dH_x dH_y dH_z \qquad (3.24)$$

which yields

$$G_z^{KT} = \frac{1}{3} + \frac{2}{3}(1 - \Delta^2 t^2) \exp\left(-\frac{1}{2}\Delta^2 t^2\right) \qquad (3.25)$$

This is known as the Gaussian Kubo-Toyabe muon spin relaxation function, after R. Kubo and T. Toyabe who first derived this expression[68].

When magnetic fields around the muon are time-dependent, or the muon can hop from site-to-site, in effect diffusing through the material which results in a time-dependent magnetic field change about the muon, the behavior of the muon is more difficult to describe. If a Markovian modulation of the field H occurs with a rate ν then

$$\frac{\langle H(t)H(0)\rangle}{\langle [H(0)]^2\rangle} = \exp(-\nu t) \tag{3.26}$$

with the range of the field distribution $P_G(H, \Delta)$ given by Eqn. 3.22[69, 70].

The time evolution of the muon spin relaxation function $g_z(t)(\equiv G_z^{KT}(t)$ of Eqn 3.25) consists of contributions from muons which experienced no changes in the magnetic field around the muon at its site in the material until time t, $g_z^{(0)}(t)$, only one change in the magnetic field, $g_z^{(1)}(t)$, two variations in the field, $g_z^{(2)}(t)$ and so on

$$G_z(t) = \sum_{n=0}^{\infty} g_z^{(n)}(t) \tag{3.27}$$

If $\exp(-\nu t)$ is the probability that the muon did not experience a field change until time t, with ν the relaxation time between changes, the time evolution of the relaxation

Figure 3.7: Schematic view of different ranges of local fields at different muon sites. Atoms with magnetic moments are denoted by •, those without by o. Muons are represented by ⋆.

69

function of a muon which did not experience a field change can be written as

$$g_z^{(0)}(t) = \exp(-\nu t)g_z(t) \tag{3.28}$$

and the time evolution of the relaxation function of a muon which underwent one field change is

$$g_z^{(1)}(t) = \nu \int_0^\infty \exp\{-\nu(t - t_1)\}g_z(t - t_1)\exp\{-\nu t_1\}g_z(t_1)\,dt_1 \quad (0 < t_1 < t) \tag{3.29}$$

In effect we have

$$G_z^{KT}(t, \Delta, \nu) = \tag{3.30}$$

$$[\exp(-\nu t)g_z(t) +$$

$$\nu \int_0^t g_z(t_1)g_z(t - t_1)\,dt_1 +$$

$$\nu^2 \int_0^t \int_0^{t_2} g_z(t_1)g_z(t_2 - t_1)\,dt_1\,dt_2 + \cdots]$$

Eqn. 3.29 can be recast in terms of a Laplace transform:

$$f_z(s) = \int_0^\infty g_z(t)\exp(-st)\,dt \tag{3.31}$$

we find[69]

$$F_z(s) = \sum_{n=0}^\infty \nu^n f_z^{n+1}(s + \nu) = \frac{f_z(s + \nu)}{1 - \nu f_z(s + \nu)} \tag{3.32}$$

and to extract the muon spin relaxation function with time-dependent magnetic effects, the inverse Laplace transform is necessary

$$G_z(t) = \int_0^\infty F_z(s)\exp(-st)\,ds \tag{3.33}$$

The heart of $G_z(t)$ lies in the calculation of $f_z(s)$

$$f_z(s) = \int_0^\infty \left\{\frac{1}{3} + \frac{2}{3}(1 - \Delta^2 t^2)\exp\left(-\frac{1}{2}\Delta^2 t^2\right)\right\}\exp(-st)\,dt \tag{3.34}$$

The original work of Hayano et al.[69] solved $f_z(s)$ in two parts. The first term of $f_z(s)$ was written analytically and remaining terms were left in an integral form. Their formula (Eqn. 20 of [69]) as published, was incorrect. This difficulty was probably

70

due to typographical errors since numerical calculations of $G_z(t)$ presented later in the same paper have the correct form.

Fortunately, $f_z(s)$ does have a full analytic form which we solved

$$f_z(s) = \frac{1}{3}s + \frac{2}{3}\sqrt{\frac{\pi}{2}}\frac{1}{\Delta}\exp\left(\frac{s^2}{2\Delta^2}\right)\text{erfc}\left(\frac{s}{\sqrt{2}\Delta}\right) \tag{3.35}$$
$$-\frac{2}{3}\Delta^2\left\{\sqrt{\frac{\pi}{2}}\frac{1}{\Delta^3}\exp\left(\frac{s^2}{2\Delta^2}\right)\text{erfc}\left(\frac{s}{\sqrt{2}\Delta}\right)\left[1 + \frac{s^2}{\Delta^2}\right] - \frac{s}{\Delta^4}\right\}.$$

$F_z(s)$ (Eqn. 3.32) and its inverse transform $G_z(t)$ need to be calculated for each time bin of a μSR spectrum. $G_z(t)$ cannot be solved analytically. A numerical inverse Laplace transform method is necessary to determine $G_z(t)$. Many numerical inversion techniques were applied[71]. Weeks method [72] using Laguerre functions was the only technique robust enough to compute $G_z(t)$ over the range of times ($\sim$8 ns – 10 μs) in a μSR spectrum.

The basis of Weeks methods is the expansion of an original function $f(t)$ into a series of generalized Laguerre functions

$$f(t) \simeq t^\alpha \exp(-ct) \sum_{k=0}^{N} a_k \frac{k!}{(\alpha + k)!} L_k^\alpha(t/T) \tag{3.36}$$

where α, c and T are parameters. The Laguerre polynomials may be calculated from the recursion relations[71]

$$L_0^\alpha(t) = 1 \tag{3.37}$$
$$L_1^\alpha(t) = 1 + \alpha - t$$
$$nL_n^\alpha(t) = (2n + \alpha - 1 - t)L_{n-1}^\alpha(t) - (n - 1 + \alpha)L_{n-2}^\alpha(t)$$

and the coefficients are given by

$$a_0 = (N + 1)^{-1}\sum_{j=0}^{N} h(\theta_j) \tag{3.38}$$
$$a_k = 2(N + 1)^{-1}\sum_{j=0}^{N} h(\theta_j)\cos(k\theta_j)$$
$$\theta_j = \left(\frac{2j + 1}{N + 1}\right)\frac{\pi}{2}$$
$$h(\theta) = \Re\{((1 + \cot(\theta/2))/(2T))^{\alpha+1}F(1/(2T) + c + \imath\cot(\theta/2)/2T)\}$$

71
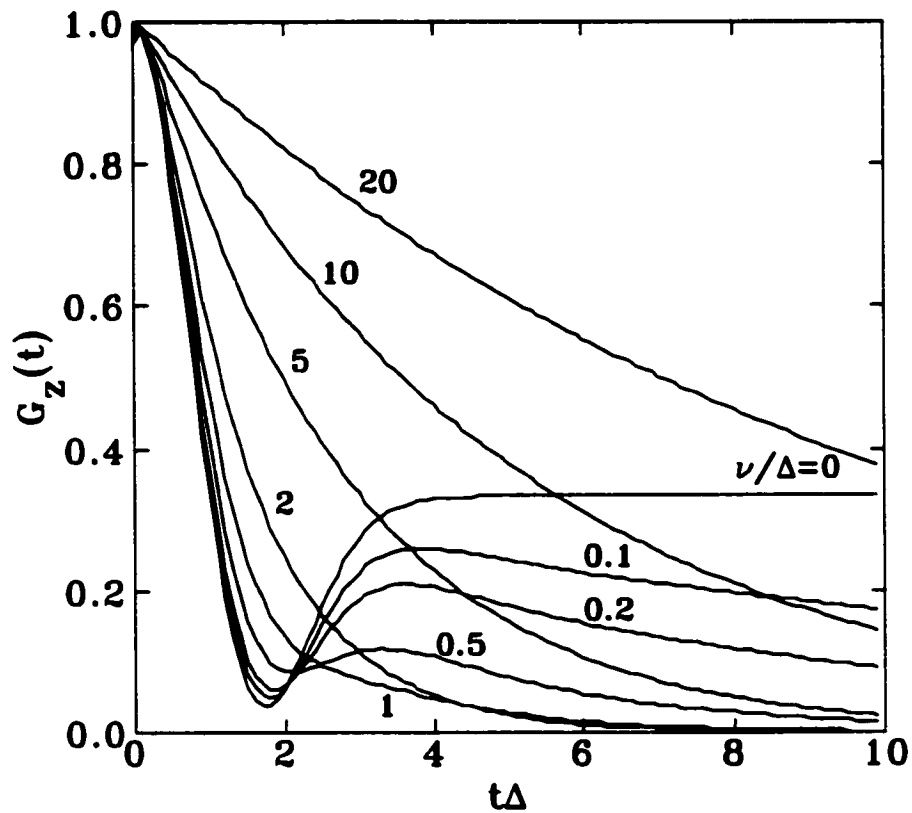
Figure 3.8: Zero-field longitudinal relaxation functions assuming a Gaussian distribution of fields about the muon for different relaxation rates ν.

A final component to the solution of $G_z(t)$ is the numerical approximation of erfc(x). The complex error function is a close cousin to the complimentary error function, erfc(x) by the relation

$$w(z) = \exp(-z^2)\mathrm{erfc}(-\imath z) = \frac{1}{\pi\imath} \int_C \frac{\exp(-t^2)\ dt}{t - z} \qquad (3.39)$$

with $z = x + \imath y$. The function $w(z)$ can be numerically approximated[73] and $f_z(s)$ can be recast in terms of $w(z)$. All the ingredients for the numerical solution of $G_z(t)$ are available.

Examples of $G_z(t)$ are presented for several values of ν in Fig. 3.8. Examining the simplest case of $\nu = 0$ (i.e. the static case) given by Eqn. 3.25, the $\frac{2}{3}$ component corresponds to the muon's damped oscillations around H due to the inhomogeneity of H_x and H_y. The persisting $\frac{1}{3}$ component represents the muons which stopped where the local field was parallel to the initial spin direction. When $\nu > 0$, for slow
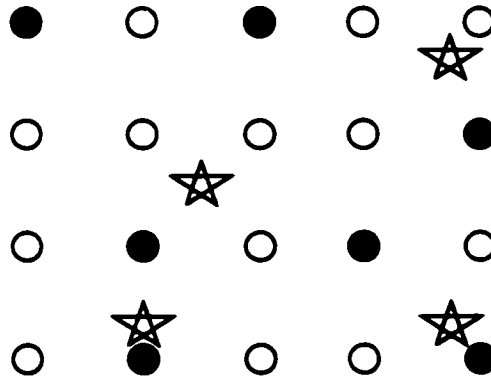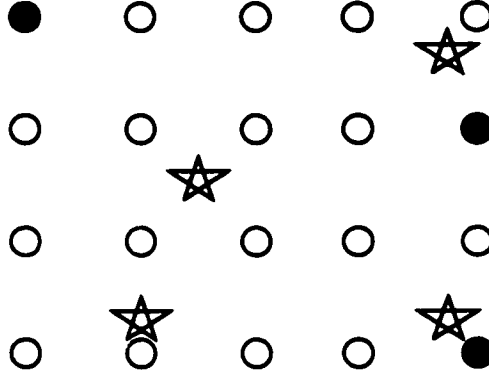
Figure 3.9: Schematic view of different ranges of local fields at different muon sites in a dilute alloy. Atoms with magnetic moments are denoted by •, those without by ○. Muons are represented by ★.

relaxation, the recovery of asymmetry to $\frac{1}{3}$ is suppressed and $G_z(t, \Delta, \nu)$ shows a hump which provides a very sensitive measure of the relaxation time while the lineshape at early times remains essentially unaltered.

In a dilute alloy (Fig. 3.9) where the magnetic impurity is only a few percent, the local field at a muon site can still be described by a Gaussian distribution such as Eqn. 3.22, however, the average magnetic field in a material is better described by a Lorentzian distribution[74]

$$P_L(H_i) = \frac{\gamma_\mu}{\pi} \frac{a}{(a^2 + \gamma_\mu^2 H_i^2)} \tag{3.40}$$

The probability $\rho(\Delta)$ of finding a muon site of value Δ is

$$\rho(\Delta) = \sqrt{\frac{2}{\pi}} \frac{a}{\Delta^2} \exp\left(\frac{-a^2}{2\Delta^2}\right) \tag{3.41}$$

where $\rho(\Delta)$ was determined to satisfy

$$P_L(H_i) = \int_0^\infty P_G(H_i)\rho(\Delta) \, d\Delta \tag{3.42}$$

so that to total field distribution in the sample is Lorentzian (Eqn. 3.40).

To obtain the zero-field muon spin relaxation function in a dilute alloy, $G_z^{KT}(t)$ of Eqn. 3.31 is integrated over the probability of being at a muon site with a Δ, i.e.

$$G_z^{SG}(t, a, \nu) = \int_0^\infty G_z^{KT}(t, \Delta, \nu)\rho(\Delta) \, d\Delta \tag{3.43}$$

73
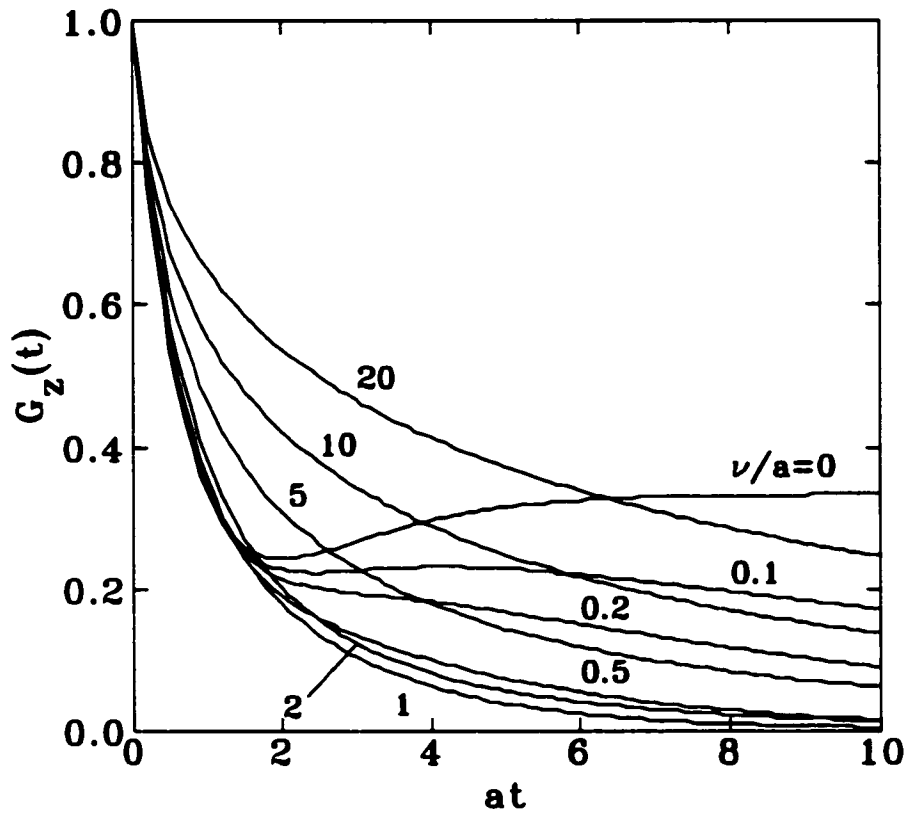
Figure 3.10: Zero-field longitudinal relaxation functions assuming a Lorentzian distribution of fields about the muon for different relaxation rates ν.

which is also called the spin-glass (SG) muon spin relaxation function as it was developed to model μSR spectra of dilute-alloy spin-glasses. Fig. 3.10 shows some typical lineshapes for different values of relaxation rate ν.

The static case, $\nu = 0$ becomes

$$G_z^L(t) = \frac{1}{3} + \frac{2}{3}(1 - at)\exp(-at) \qquad (3.44)$$

as originally derived by Kubo[75].

Calculations of $G_z^{KT}(t, \Delta, \nu)$ and $G_z^{SG}(t, \Delta, \nu)$ are involved and require a large amount of computation time. In fact, one does not find any examples of the full formalism being used to fit data anywhere in the literature. The closest attempt has been modeling the muon behavior with Monte Carlo simulations and extrapolating the results to experimental spectra[76].

In general, μSR spectra are characterized with a so-called dynamical Kubo-Toyabe relaxation (product) function[74] which is simple to compute

$$G_z(t) = G_s(t) \times G_d(t) \tag{3.45}$$

$$G_s(t) = \frac{1}{3} + \frac{2}{3}\{1 - (\Delta t)^\alpha\} \exp\left(-\frac{(\Delta t)^\alpha}{\alpha}\right)$$

$$G_d(t) = \exp[-(\lambda t)]$$

The K-T minimum is defined by $\alpha = 1$ for a Lorentzian lineshape and $\alpha = 2$ for a Gaussian one in $G_s(t)$. The fluctuating local field which leads to muon spin depolarization at a rate $\lambda(T)$ is described by $G_d(t)$. $\lambda(T)$ is an effective $1/T_1$ spin-lattice
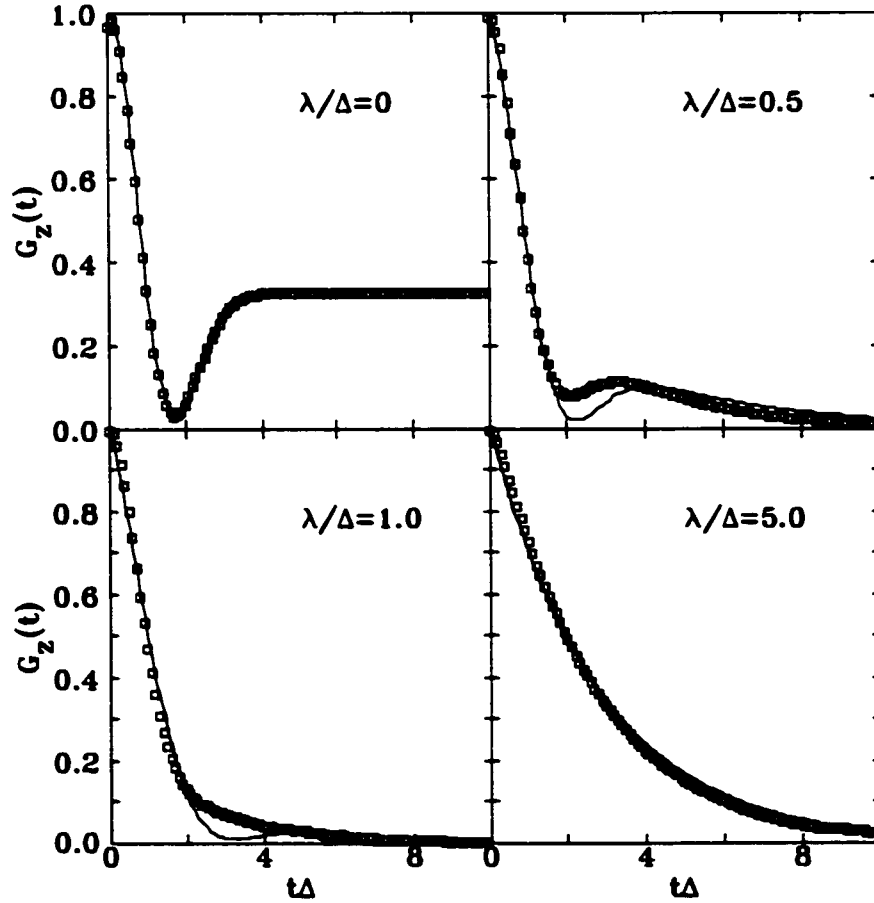
Figure 3.11: Zero-field longitudinal relaxation functions calculated using the dynamic Kubo-Toyabe formalism ($\square$) and fitted with the product function, Eqn. 3.46 (solid lines). Note the misfit for values of $\lambda/\Delta = 0.5$ and 1.0.

75

relaxation rate.

Since the bulk of the μSR literature is devoted to the study of magnetic systems[92] where there is a clear distinction between static effects in early time channels and dynamic effects in later time channels, Eqn. 3.45 correctly describes these μSR spectra, and the numerically intensive calculations required to fit spectra with the full dynamic Gaussian Kubo-Toyabe or spin-glass function, can be avoided.

For materials with a high concentration of magnetic moments, the product function may no longer be adequate. This is shown in Fig. 3.11, where various values of $(\lambda \equiv \nu)/\Delta$ are plotted. Lineshapes from the correct dynamic Kubo-Toyabe function for a Gaussian distribution of fields are fitted with the product function where $\alpha = 2$. At intermediate values of λ/Δ the product function cannot correctly describe the lineshape of a μSR spectrum of a material with strong static and dynamic signals. An attempt to deal with this difficulty (incorrectly) in the μSR literature is to fit the value of α (between 1 and 2) for the static signal, and use a stretched exponential function $G_d(t) = \exp[-(\lambda t)^\beta]$ to describe the dynamic signal. This will fit spectra, however, values of λ may be adversely affected. Changes in fitted values of α and β over a temperature scan with μSR spectra of a sample will sometimes be interpreted in terms of two distinct populations of slow moments and fast moments in the sample, an attempt to justify use of the product function[74, 92]. Values of α which are not 1 or 2, and $\beta \neq 1$ are simply signs that the full dynamic Kubo-Toyabe or spin-glass function are necessary to fit the lineshape of the μSR spectrum.

Chapter 4

Results and Discussion

The goal of this research is to examine materials with static and dynamic disorder, and identify the spectral signatures of these properties. To begin with, it is necessary to establish the effects of static disorder on transmission Mössbauer and selective excitation double Mössbauer (SEDM) spectra. With this knowledge, SEDM can be used to determine if magnetic relaxation is happening in a material whose transmission Mössbauer spectra show spectral characteristics which can be modeled in terms of dynamic phenomena. Once dynamic magnetic behavior has been unambiguously identified with SEDM, zero field muon spin relaxation (ZF-μSR) can be used to simultaneously identify the static and dynamic properties of some magnetic materials that experience both time-independent and time-dependent magnetic disorder. Transmission Mössbauer spectroscopy can then be used to measure the static disorder of the material while SEDM spectroscopy will establish the magnetic properties of the dynamic disorder measured with ZF-μSR.

4.1 Static disorder

4.1.1 Amorphous alloy

To establish the effects of static disorder on Mössbauer spectra, a-$Fe_{80}B_{20}$ was studied. This alloy was prepared by arc melting the appropriate ratio of pure elements under

77

IS	-0.055±0.002 mm/s
IS-B_{hf}	0.0050±0.0009 mm/s/T
Γ	0.218±0.005 mm/s
absorption	9.46±0.08 %
baseline	$6.1755 \times 10^5 \pm 218$ counts
R25	2.18±0.02
B_{hf} peak	25.5±0.2 T
B_{hf} width, left	3.51±0.02 T
B_{hf} width, right	3.27±0.05 T

Table 4.1: Asymmetric Gaussian distribution of B_{hf} for amorphous materials fit results. IS $\equiv$ isomer shift, IS-B_{hf} $\equiv$ field correlated isomer shift.

Ti-gettered argon and then melt spinning under a partial pressure of helium onto a copper wheel at 50 m/s. Absence of crystallinity was confirmed using Cu K_α x-ray diffraction. Thermogravimetric analysis determined a Curie temperature (T_C) of 658 K. The spectrum was collected at 290 K, which is 0.45 T_C.

Fig. 4.1 shows the transmission spectrum fitted with an asymmetric Gaussian hyperfine field distribution, $P(B_{hf})$. Table 4.1 lists the fit results. The transmission spectrum exhibits the usual broadened six-line pattern of a metallic glass with a broad hyperfine field distribution. The computed static distribution of hyperfine fields (which is almost a symmetric Gaussian) properly describes the a-$Fe_{80}B_{20}$.

Collecting a SEDM spectrum while driving line #1 of the a-$Fe_{80}B_{20}$ provided a strong indication that selective population of the $m_e = -\frac{3}{2}$ sublevel was happening. With the largest cross-section, driving line #1 provides the strongest signal (notice the larger intensity of line #1 in Fig. 4.2), and after approximately three days of counting, a single line spectrum resulted. The line position of the SEDM spectrum is in perfect agreement with the line #1 energy of the transmission spectrum (Fig. 4.2) where the appearance of a single line agrees with the selection rules. The effects of static disorder on a SEDM spectrum are clear: the selection rules for a static magnetic hyperfine field, where pumping the $m_e = -\frac{3}{2}$ excited state results in decay to the $m_g = -\frac{1}{2}$ ground state, are followed. In effect, $Fe_{80}B_{20}$ is exhibiting the same
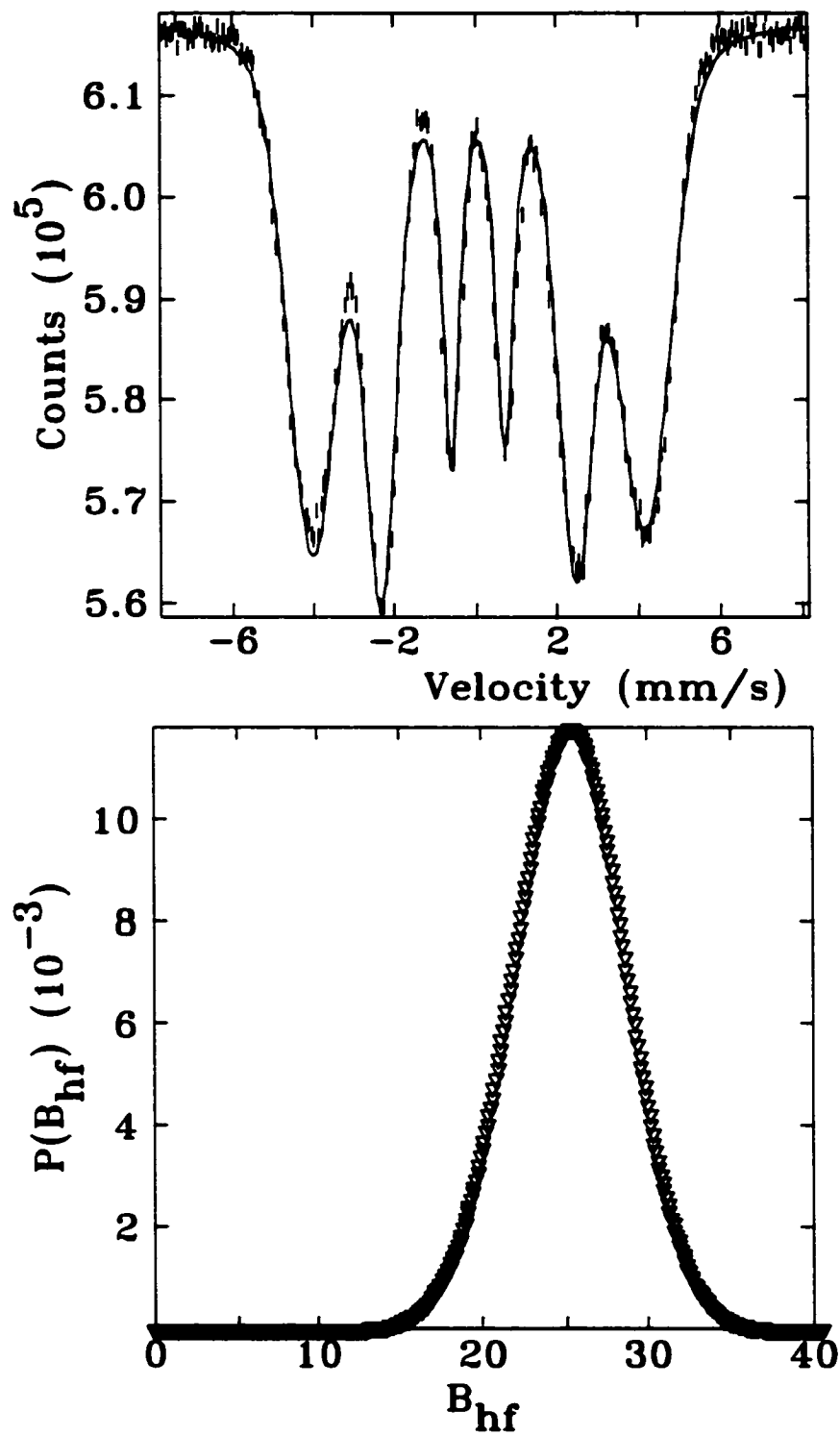
Figure 4.1: A transmission spectrum of a-$Fe_{80}B_{20}$ at 290 K fit using an asymmetric Gaussian $P(B_{hf})$ hyperfine field distribution.
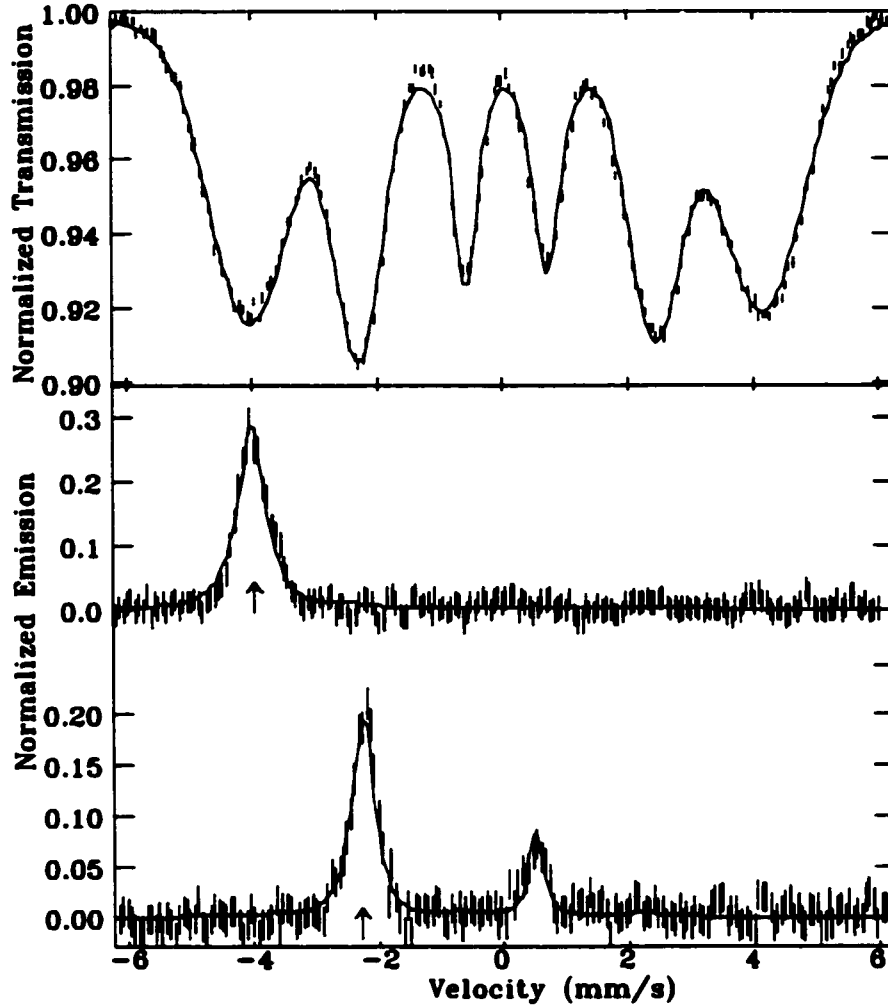
Figure 4.2: Transmission Mössbauer spectrum of $Fe_{80}B_{20}$ and SEDM spectra when lines #1 and #2 are driven (pump energies indicated by the ↑).

magnetic behavior as α-Fe.

Further evidence that a static field is being probed by SEDM is given by driving line #2. This establishes that selective population of a nuclear sublevel is indeed occurring in the disordered alloy. Population of the $m_e = -\frac{1}{2}$ state results in de-excitations to the $m_g = -\frac{1}{2}$ and $m_g = +\frac{1}{2}$ states, i.e. pumping line #2 results in a spectrum with lines #2 and #4, as shown in Fig. 4.2. The appearance of lines #2 and #4 are in agreement with the selection rules, and with a smaller nuclear cross-section, line #2 has a smaller intensity than line #1 (compare the intensities of the two SEDM spectra in Fig. 4.2). Additionally, since the line #4 nuclear cross-section is smaller

than the line #2 nuclear cross-section, line #4 has the smallest intensity.

The striking difference between the SEDM spectra of α-Fe and the a-Fe$_{80}$B$_{20}$ is that the lines are much broader (cf. Fig. 2.18). The broad lines can be fitted assuming the same $P(B_{hf})$ determined from the transmission spectrum (Fig. 4.2). From the distribution of hyperfine fields, a range of energies for the $m_g = -\frac{1}{2} \rightarrow m_e = -\frac{3}{2}$ transition is pumped by the source during the SEDM experiment (unlike the single transition driven in α-Fe). $\Gamma_s = 0.120 \pm 0.001$ mm/s and $P(B_{hf})$ correctly predict the SEDM lineshapes with fitted linewidths of 0.165$\pm$0.002 mm/s, that includes the CED energy resolution, describing the energy distribution of scattered radiation from the sample. Compare the narrower SEDM linewidths to those from the individually fitted lines of the transmission spectrum of a-Fe$_{80}$B$_{20}$; line #1 gives 0.71$\pm$0.02 mm/s and line #2 0.39$\pm$0.01 mm/s.

The smaller linewidths of the SEDM fits indicate that only part of the hyperfine field distribution is being probed by the SEDM experiment, a consequence of the narrow source linewidth that is driving a small fraction of the energies corresponding to the line #1 transition. This is direct evidence that static disorder can be detected using SEDM spectroscopy. These are the first SEDM results on a magnetic material with static disorder, and strengthens the validity of using a distribution of hyperfine fields to describe the magnetic environments in such a material.

4.1.2 Chemically disordered alloy

The physical description of an amorphous alloy exhibiting a distribution of local magnetic environments for each Mössbauer atom is clearly applicable when representing an amorphous alloy system like a-Fe$_{80}$B$_{20}$. Invar, Fe$_{65}$Ni$_{35}$, is an example of a magnetic system where the physical interpretation of Mössbauer spectra is not so clear-cut[11, 12, 13, 14].

A Fe$_{65}$Ni$_{35}$ sample was made by arc melting appropriate ratios of pure elements under Ti-gettered argon and then melt spun under a partial pressure of helium onto

Temp	295 K	395 K	498 K
Γ	0.149±0.006 mm/s	0.136±0.009 mm/s	0.132±0.001 mm/s
R25	1.96±0.06	1.87±0.09	2.00
IS	-0.09±0.02 mm/s	-0.07±0.02 mm/s	-0.146±0.005 mm/s
IS-B_{hf}	0.0028±0.0006 mm/s/T	0.00137±0.0009 mm/s/T	0.0029±0.0006 mm/s/T
$\langle B_{hf} \rangle$	23.2 T	17.7 T	8.2 T

Table 4.2: Some fit results of the $Fe_{65}Ni_{35}$ using Window's method.

a stainless-steel wheel at 30 m/s. X-ray diffraction spectra displayed the expected crystalline peaks and thermogravimetric analysis determined a Curie temperature of 499 K[77]. Some $Fe_{65}Ni_{35}$ ribbon was annealed at 800 K for an hour and the expected five degree increase in the Curie temperature was observed[12].

Transmission Mössbauer spectra were collected and assuming a distribution of environments, were fit using Window's method (Eqn. 3.1). Examples of some of the spectra and the $P(B_{hf})$ used to fit them are shown in Figs. 4.3, 4.4 and 4.5 with fit results in Table 4.2.

SEDM spectra obtained while driving line #1 of $Fe_{65}Ni_{35}$ show a single broadened line at all temperatures examined (Fig. 4.7). These SEDM lineshape posses the same characteristics as the a-$Fe_{80}B_{20}$ SEDM spectra. Driving the $m_g = -\frac{1}{2} \rightarrow m_e = -\frac{3}{2}$ transition (line #1) results in only a decay via the $m_e = -\frac{3}{2} \rightarrow m_g = -\frac{1}{2}$ transition (again line #1). The SEDM spectra of $Fe_{65}Ni_{35}$ are consistently fitted with the same $P(B_{hf})$ distribution model as was applied to the a-$Fe_{80}B_{20}$ alloy (Eqn. 3.16), using the $P(B_{hf})$ determined from the transmission Mössbauer spectra of $Fe_{65}Ni_{35}$ fits with Window's method. Fitted parameters were just the SEDM pump line intensity (line #1) and the linewidth of the SEDM spectra that characterizes the CED and lifetime of the Mössbauer atom's excited state ($\Gamma = 0.167 \pm 0.005$ mm/s), consistent with the a-$Fe_{80}B_{20}$ fits. $P(B_{hf})$ from the transmission Mössbauer spectra fits once again correctly predict the SEDM lineshape.

The transmission Mössbauer spectra of the $Fe_{65}Ni_{35}$ spectra can be equally well fit
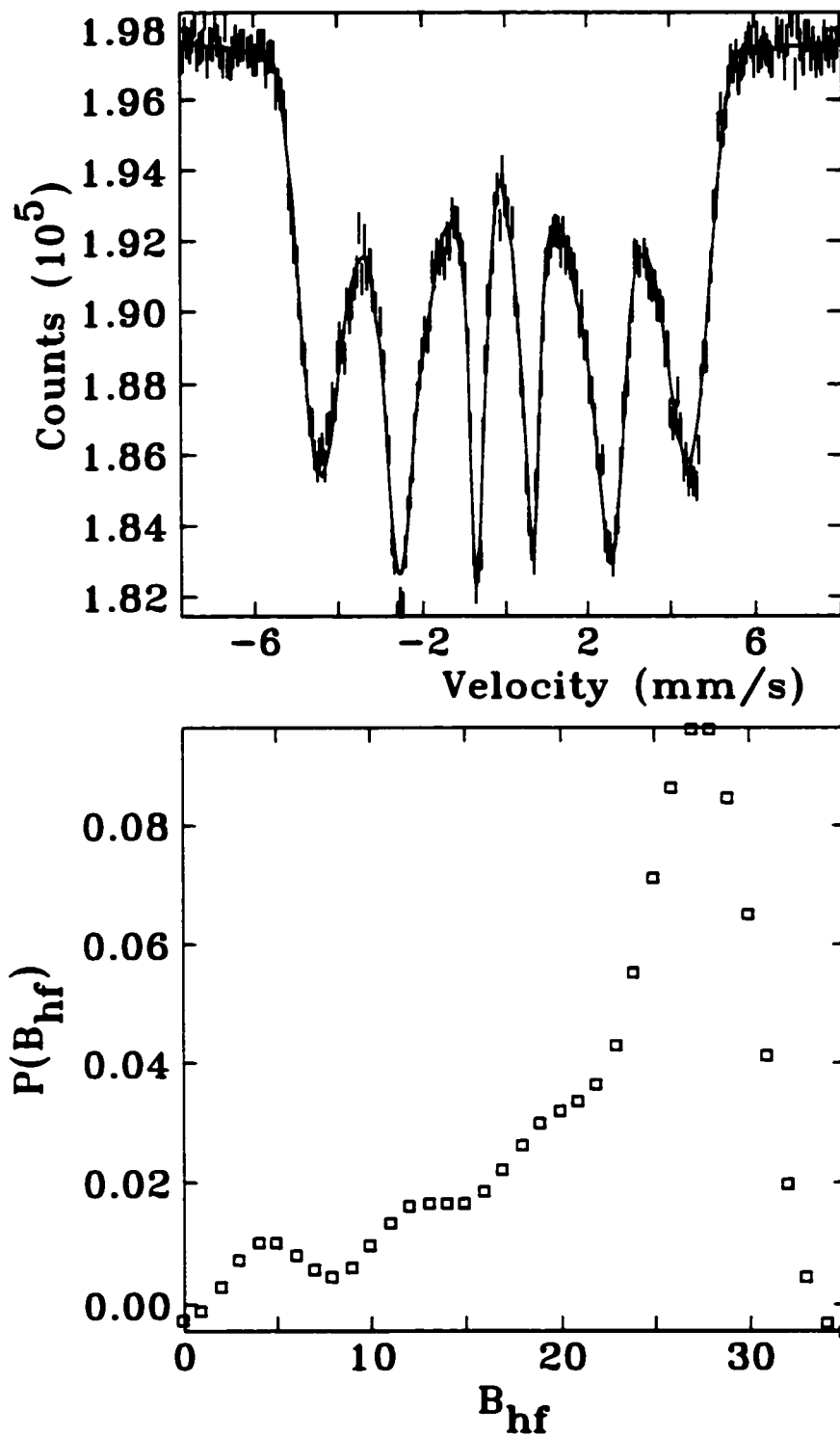
Figure 4.3: Transmission spectrum with a Window fit $P(B_{hf})$ of $Fe_{65}Ni_{35}$ at 295 K.
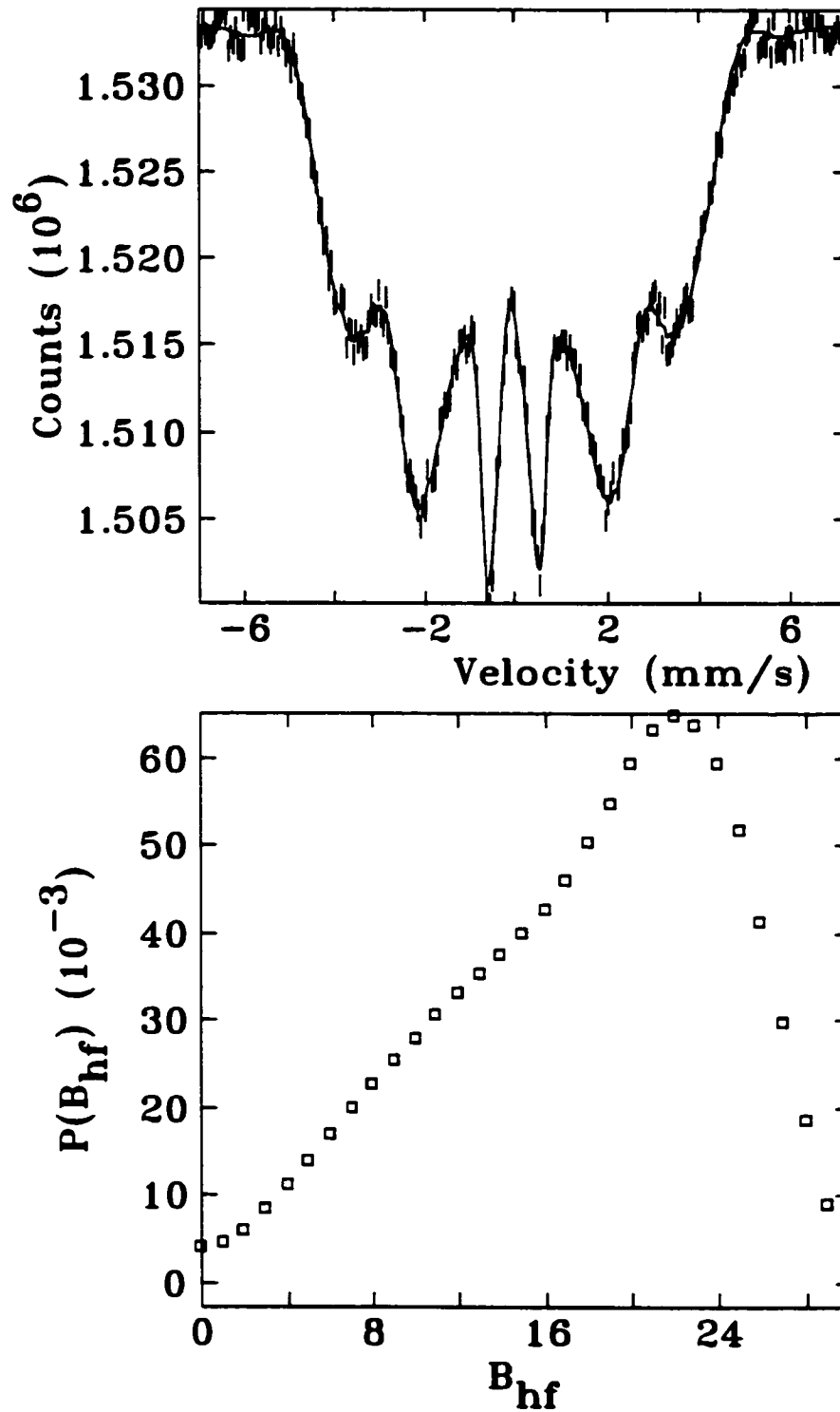
Figure 4.4: Transmission spectrum with a Window fit $P(B_{hf})$ of $Fe_{65}Ni_{35}$ at 395 K.
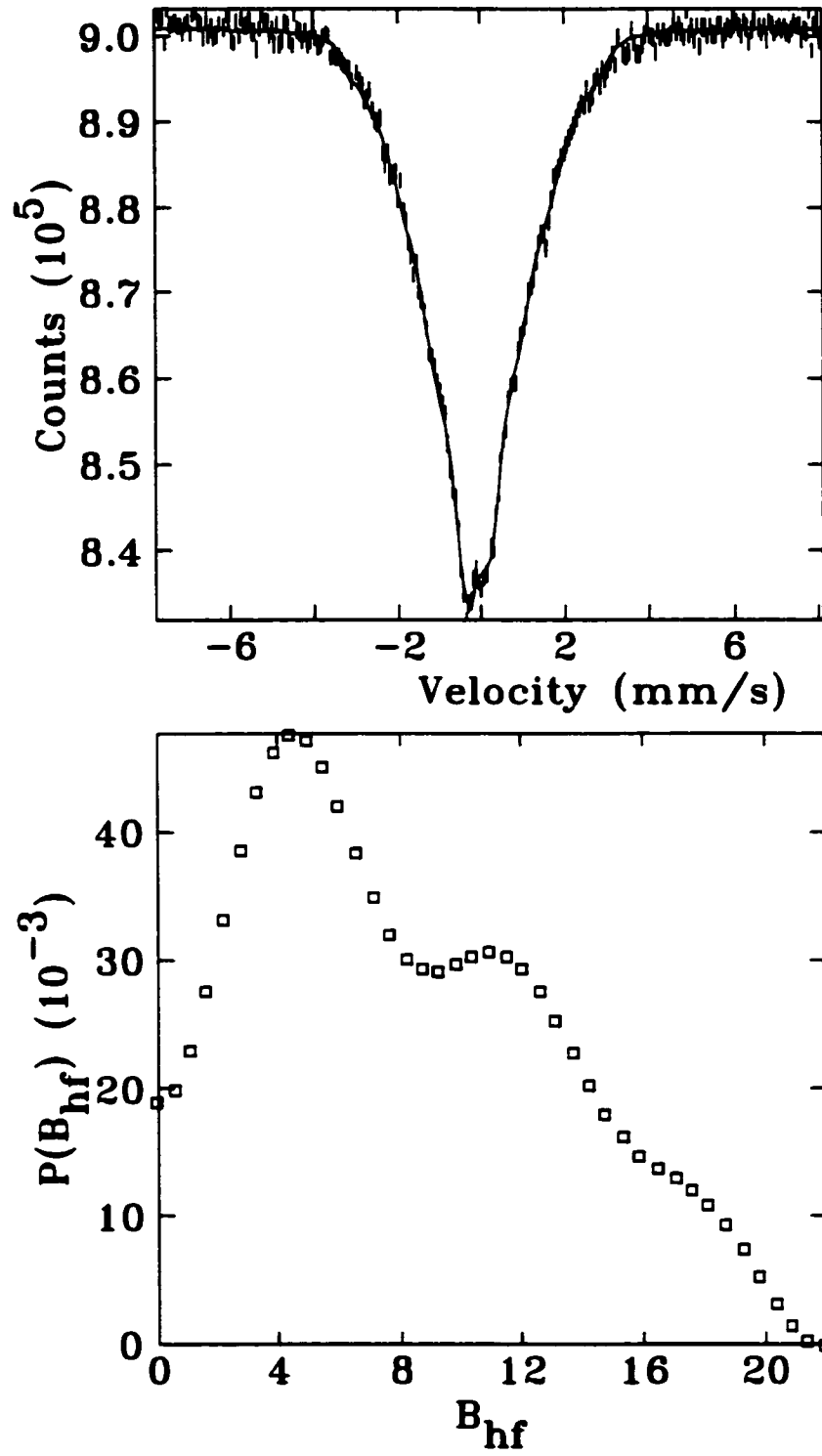
Figure 4.5: Transmission spectrum with a Window fit $P(B_{hf})$ of $Fe_{65}Ni_{35}$ at 498 K.

assuming a single, time-dependent magnetic environment around Mössbauer atoms[14]. Using a simple Blume-Tjon model (Eqn. 3.2) with a magnetization vector characterizing the magnetic moment orientation (i.e. two asymmetric potential barriers describe the $0°$ and $180°$ moment orientations), we can fit the $Fe_{65}Ni_{35}$ transmission Mössbauer spectra. Spectra and fits are shown in Fig. 4.6 with fitted results in Table 4.3. A supermoment fluctuation rate (bottom of Fig. 4.6) describes the moment flips between the two uniaxial directions by R and the magnetization is defined as $M \equiv H_0 \eta$ (see Eqn. 3.2). Field and linewidth were determined from room temperature spectra and kept fixed for all other temperatures to remove possible cross-correlations between these parameters and the relaxation rate.

Fluctuation rates from these fits should, in principle, also describe the SEDM spectrum of the same temperature. With $\langle B_{hf} \rangle$ and isomer shift from the field distribution fits of the $Fe_{65}Ni_{35}$ spectra, we can fit the SEDM spectra using Eqn. 3.21. From the large fluctuation rates at high temperatures, a strong peak from the $m_e = +\frac{3}{2} \rightarrow m_g = +\frac{1}{2}$ transition, due to a moment flip during the Larmor precession time of the excited nucleus, should be present. However, the 496 K $(0.99T_C)$ spectrum shown at the bottom of Fig. 4.7 clearly demonstrates that the relaxation rate derived from the transmission fit is far too high. Fluctuation rates derived from the SEDM spectra using Eqn. 3.21 for some of the temperatures investigated are shown in Fig. 4.8. If relaxation effects are present, they cannot be happening at rates any faster then 0 ± 0.1 MHz at 496 K $(0.99T_C)$.

Temp	295 K	395 K	498 K
Γ	0.244±0.007 mm/s	0.244 mm/s	0.244 mm/s
IS	-0.0137±0.005 mm/s	-0.049±0.007 mm/s	-0.121±0.009
B_{hf}	31.2±0.2 T	31.2 T	31.2 T
M	27±1 T	20.4±0.5 T	8.9±0.3 T
ν	150±5 MHz	176±4 MHz	283±8 MHz

Table 4.3: Some fit results of the $Fe_{65}Ni_{35}$ using a Blume-Tjon relaxation model. R25 = 2.
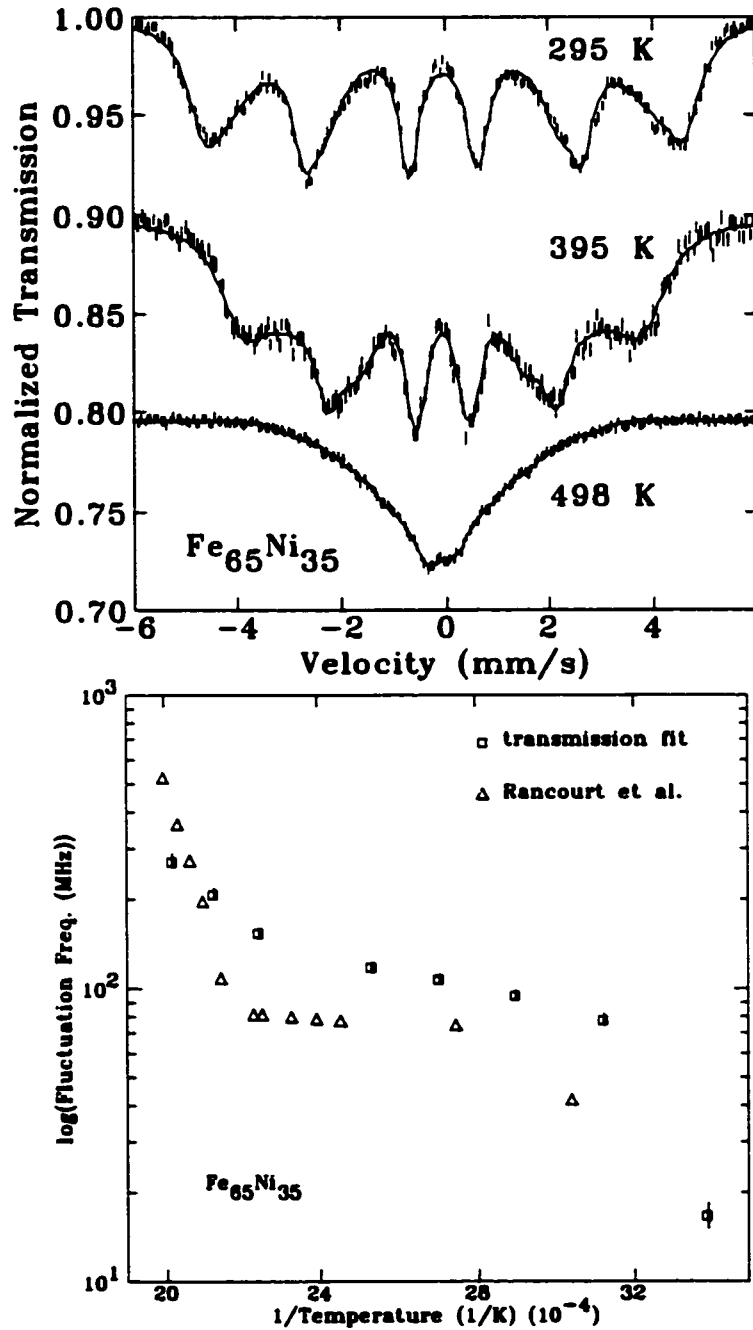
Figure 4.6: Top: Transmission spectra of $Fe_{65}Ni_{35}$ fit using a Blume-Tjon relaxation model. Bottom: Logarithm of the supermoment fluctuation rate as a function of reciprocal temperature from transmission Mössbauer spectra fits. Values from Rancourt et al.[14] for comparison.
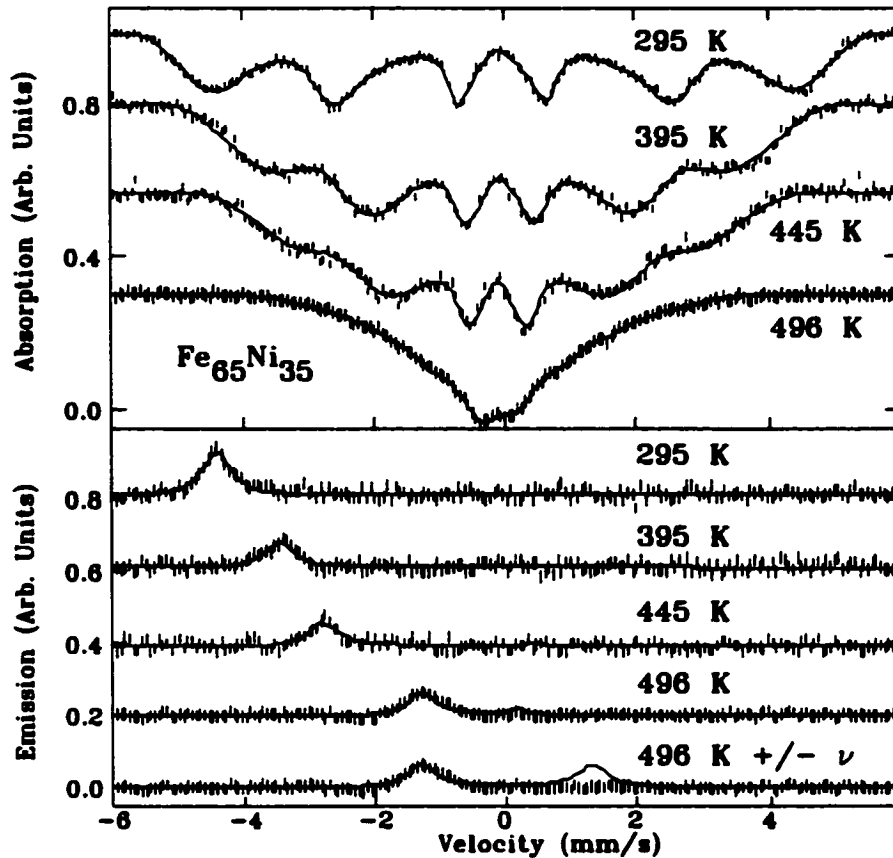
Figure 4.7: Transmission Mössbauer spectra of $Fe_{65}Ni_{35}$ (top) obtained at indicated temperatures fit using a distribution of hyperfine fields and SEDM spectra of line #1 (bottom). Similar results were obtained by Price and Stewart[31] on $Fe_{66}Ni_{34}$ at 295 K.

Although transmission Mössbauer spectra of $Fe_{65}Ni_{35}$ were open to interpretation as to the physical origin of the lineshape (i.e. static disorder or magnetic relaxation), SEDM has clearly shown that magnetic relaxation is not occurring in $Fe_{65}Ni_{35}$ at all temperatures up to $0.99T_C$. This is a clear display of the power of the SEDM technique: it provides unambiguous spectral signatures for static and dynamic magnetic phenomena. This is the first incontrovertible experimental evidence that $Fe_{65}Ni_{35}$ is a magnetic material with a continuum of *static* magnetic fields.
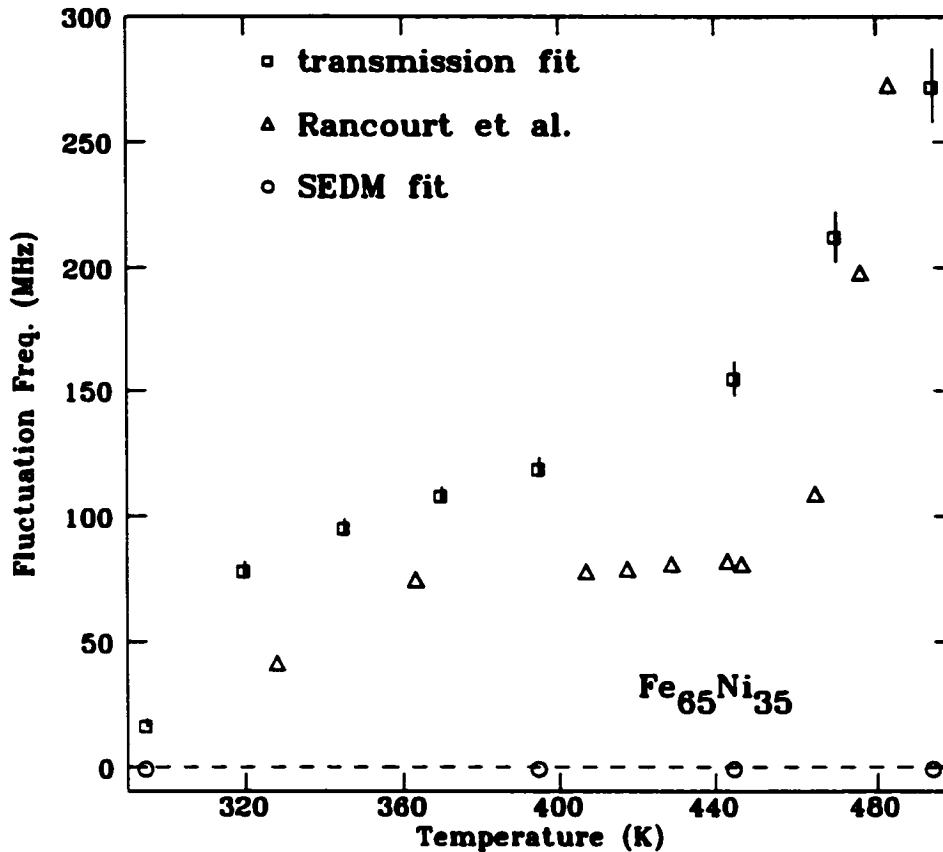
Figure 4.8: Supermoment fluctuation rate as a function of reciprocal temperature from transmission Mössbauer spectra fits. Values from Rancourt et al.[14] for comparison. Estimates of the fluctuation rates from SEDM data are plotted, displaying discrepancy with transmission fit results.

4.2 Magnetic fine particle systems

It is now necessary to collect SEDM spectra of a material which is undergoing magnetic relaxation. The spectral characteristics that are provided by the relaxation model of Eqn. 3.21 need to be confirmed. A single domain particle, when superparamagnetic, is known to undergo a spin flip. Magnetic fine particle systems are composed of single domain particles, so SEDM spectra of this sort of system should provide the necessary evidence of magnetic relaxation. A ferrofluid is a convenient magnetic fine particle system, so the next step in our investigation of dynamic magnetic disorder is to measure superparamagnetic relaxation in a ferrofluid with transmission Mössbauer and SEDM spectroscopy. While trying to fit transmission Mössbauer spectra of the

ferrofluids, it was discovered that the lineshape problem has not been adequately solved. The difficulty was overcome, as described in Sec. 3.1, and a third magnetic fine particle system, a polysaccharide iron complex (a ferritin biomimic) was examined with transmission Mössbauer spectroscopy as an additional test sample for the model.

Transmission Mössbauer studies

The magnetic fine particle systems that were examined were two commercial Fe_3O_4 ferrofluids[34] and an akaganéite (β-$Fe^{+3}O(OH)$) based polysaccharide-iron complex (PIC) called Niferex[49]. The manufacturer supplied the ferrofluids with particle size distributions determined by electron microscopy that gave $ln(\sigma_D) = 0.225$ for the 6.0 nm ferrofluid and $ln(\sigma_D) = 0.2$ for the 4.5 nm ferrofluid. The PIC is a ferritin biomimic and is reported to have a mean particle size of 6.5 nm[58]. $ln(\sigma_D) = 0.3$ was chosen, in agreement with previous studies[58], and allowed for consistent fits to the spectra. AC susceptibility (χ_{ac}) data were collected using a Quantum Design Physical Properties Measurement System at temperatures from 2.5 K to 300 K with driving frequencies of 10, 100, 1 kHz and 10 kHz. An exponential dependence of the blocking temperature as a function of driving frequency was demonstrated and used to extrapolate blocking temperatures relevant to the Mössbauer effect measurement time of 10^{-8} s.

The ferrofluid samples were left at room temperature for six months to determine if any changes in contents would occur. The 4.5 nm ferrofluid particles remained unaffected, but the 6.0 nm ferrofluid had aged in some manner that caused visible clumping. Mössbauer and χ_{ac} data were collected for this 6.0 nm aged ferrofluid to examine variations in its magnetic properties.

χ_{ac} vs. T for the Fe_3O_4 ferrofluids is shown in Fig. 4.9 for various measuring frequencies. Similar results were obtained with the PIC. For a given frequency, $\chi_{ac}(T)$ exhibits a maximum at T_B when the superparamagnetic moment flip rate coincides with the driving frequency of the measurement. The broad peak in χ_{ac} reflects the
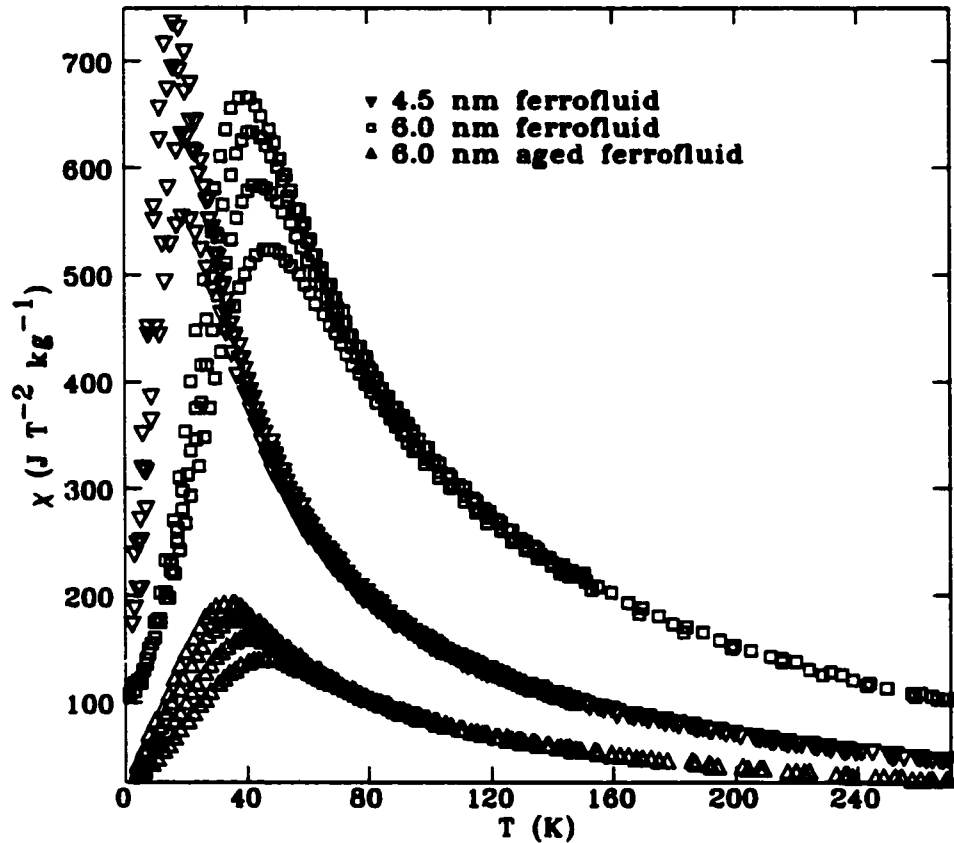
Figure 4.9: Thermal variation of χ_{ac} vs frequency for the Fe_3O_4 ferrofluids. This behavior scaled with the saturation magnetization established for each sample, ensuring that these results exhibit the magnetic behavior of the iron in the particles. Note the substantial reduction in signal caused by aging of the 6 nm sample. Driving frequencies of 10, 100, 1 kHz and 10 kHz were used to demonstrate an exponential dependence of the blocking temperature as a function of driving frequency. With this trend, blocking temperatures relevant to the Mössbauer effect measurement time of 10^{-8} s could be extrapolated.

distribution of particle sizes in the ferrofluids. The lower T_B for the smaller mean particle sized ferrofluid is expected. Smaller particles will reside in shallower potential wells, i.e. KV will be smaller, and will unblock at a lower temperature. This is consistent with recent χ_{ac} measurements on Fe_3O_4[63]. Data for the aged 6.0 nm ferrofluid exhibit a substantial reduction in amplitude and a shift in T_B to lower temperatures. Experimental results[60] and Monte Carlo simulations[61] indicate that increasing interparticle interaction strength causes a lowering of T_B and a strong suppression of χ_{ac}. In addition, the frequency dependence of T_B is reduced. Thus
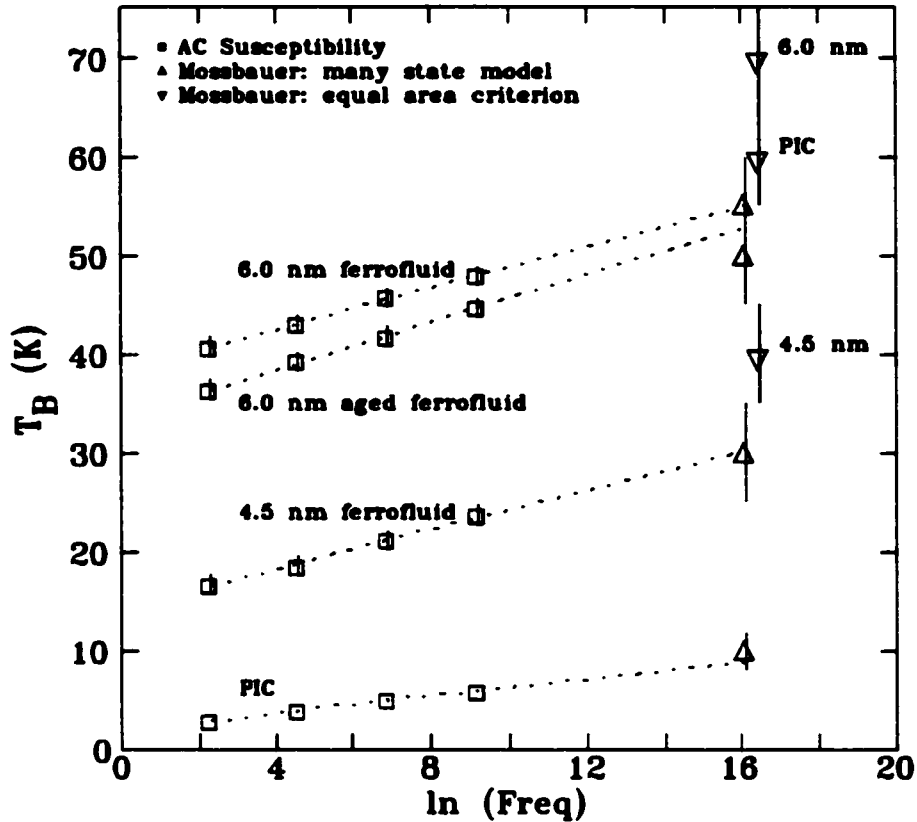
Figure 4.10: Plots of T_B versus measurement frequency for the χ_{ac} measurements and Mössbauer many-level model. Notice the poor agreement of the equal area criteria, especially for the PIC.

the aging-induced changes in the 6.0 nm ferrofluid are fully consistent with increased interparticle interactions associated with the visible clumping that had occurred.

The variation of T_B with measurement frequency for the χ_{ac} data is shown in Fig. 4.10, where the exponential behavior is clear in this log-linear plot. Failure of the equal area definition for T_B is also clearly demonstrated, most conspicuously by the PIC, with a factor of six over estimate of T_B. The full range of magnetic behavior (static moments, collective excitation, and superparamagnetism) is present at intermediate temperatures (such as T_B). The PIC sample, with the widest distribution of particle sizes, provides the strongest signals from static moments and collective excitations, so is an ideal test for the multi-level model. For the PIC, our model correctly describes the large spectral contribution of static moments and collective excitations

as well as the small superparamagnetic component of the particle size distribution at T_B. This ensures consistent fits of the PIC through the whole temperature range, and, for the PIC, as well as the ferrofluid samples, provides excellent agreement with the χ_{ac} results.

Mössbauer spectra collected for the different samples are shown in Fig. 4.11 – the 4.5 nm ferrofluid, Fig. 4.12 – the 6.0 nm as-received ferrofluid, Fig. 4.13 – the 6.0 nm aged ferrofluid and Fig. 4.14 – the PIC. For the ferrofluids, once the carrier liquid has frozen at around 200 K, the easy axis of each particle is frozen in a random direction. The PIC is a powder sample ensuring a random orientation for the easy axes of the particles at any temperature. The freezing conditions for the ferrofluids and powder form of the PIC ensures that the magnetization orientation of all single domain particles is completely isotropic in space (R25=2). For all samples at high temperatures a collapsed lineshape with essentially zero hyperfine field is observed. All of the samples are superparamagnetic and are above T_B at this point. On cooling, the flip rates of largest particles slow first and a sextet component develops in the spectra. Next, the moment flip rates of smaller particles slow and a broad sextet becomes more distinct with line asymmetry from collective excitations appearing. Finally, at the lowest temperatures, less line asymmetry from collective excitations occurs as moments become fully blocked. The coexistence of sextet and central components in the spectra over a large range of temperatures is unique to magnetic fine particle systems. The area ratio of sextet and collapsed components over a wide temperature range is unlike the swift collapse within a small temperature range seen in paramagnetic to ferromagnetic phase transitions [4].

25 levels were used in our model (Sec. 3.1) to fit the ferrofluid spectra and 36 levels for the PIC. Fewer levels would not describe the spectra consistently for all temperatures and more levels simply increased the computation time for least-squares fits. Table 4.4 contains some of the fitted parameters for the spectra. The hyperfine field was a fitted parameter for low temperature spectra. As relaxation effects became dominant, the field was fixed at 50 T to reduce the effects of correlations between
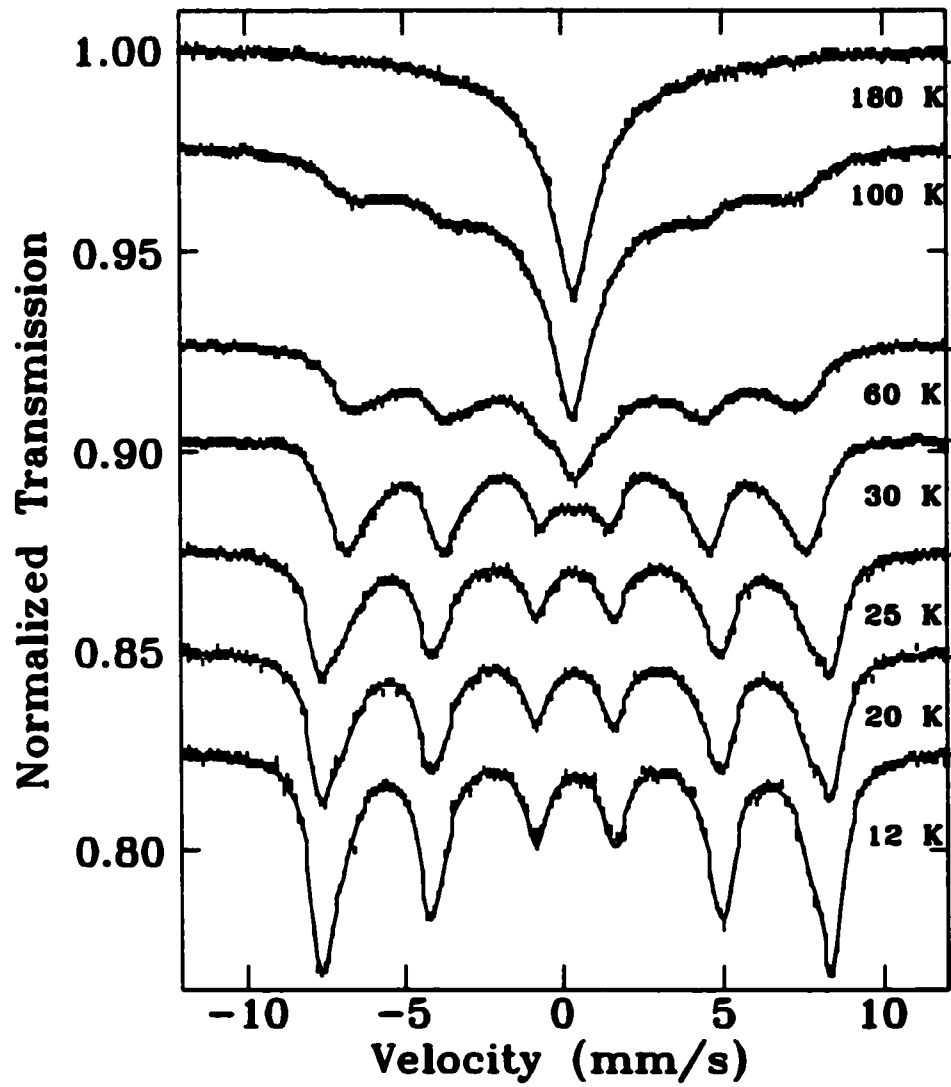
Figure 4.11: Mössbauer spectra of the 4.5 nm Fe_3O_4 ferrofluid.
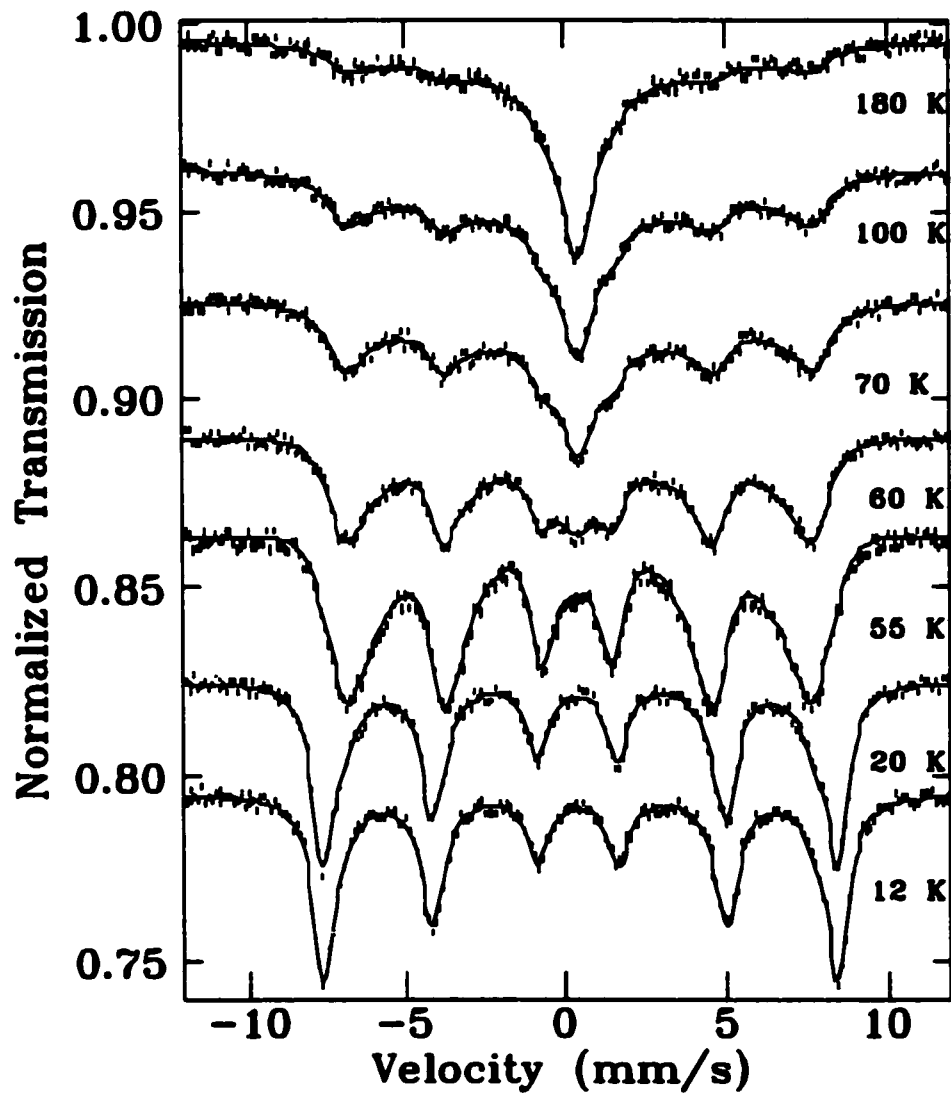
Figure 4.12: Mössbauer spectra of the 6.0 nm Fe_3O_4 ferrofluid.

95
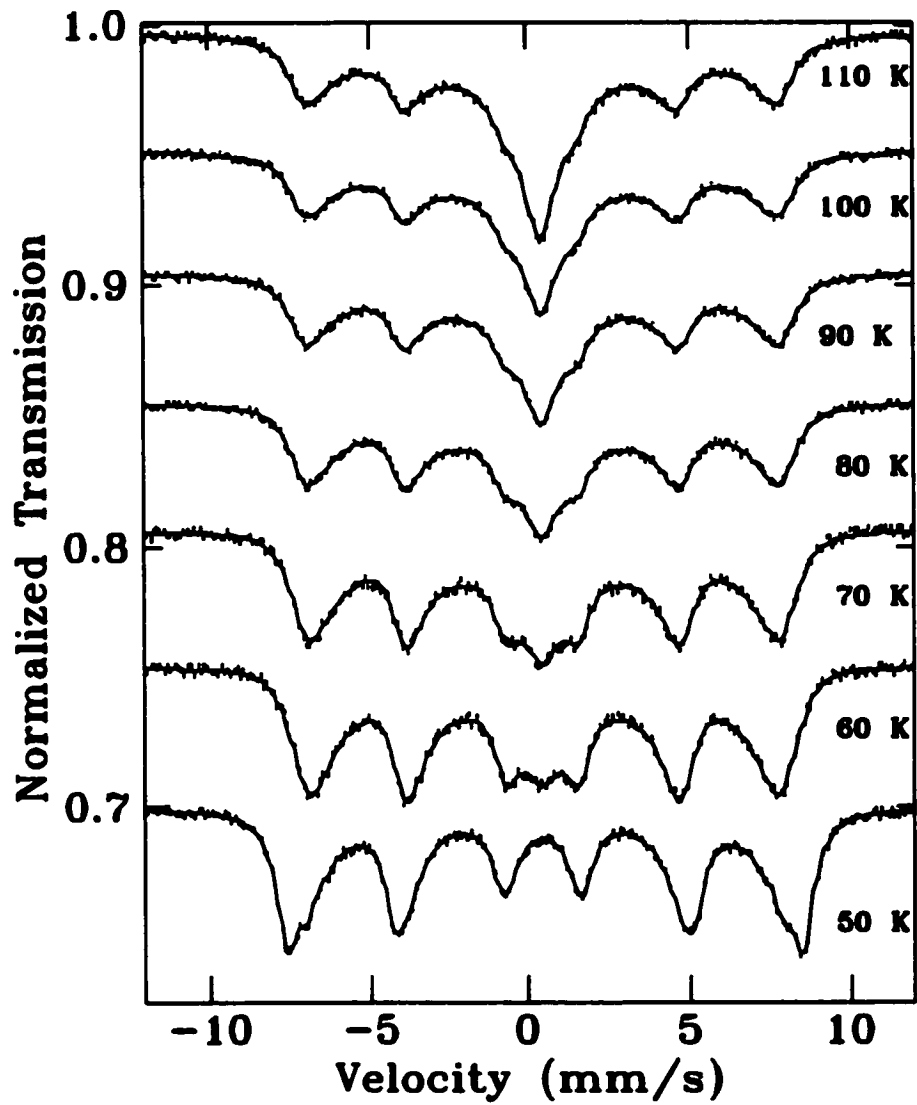
Figure 4.13: Mössbauer spectra of the aged 6.0 nm Fe_3O_4 ferrofluid.

96
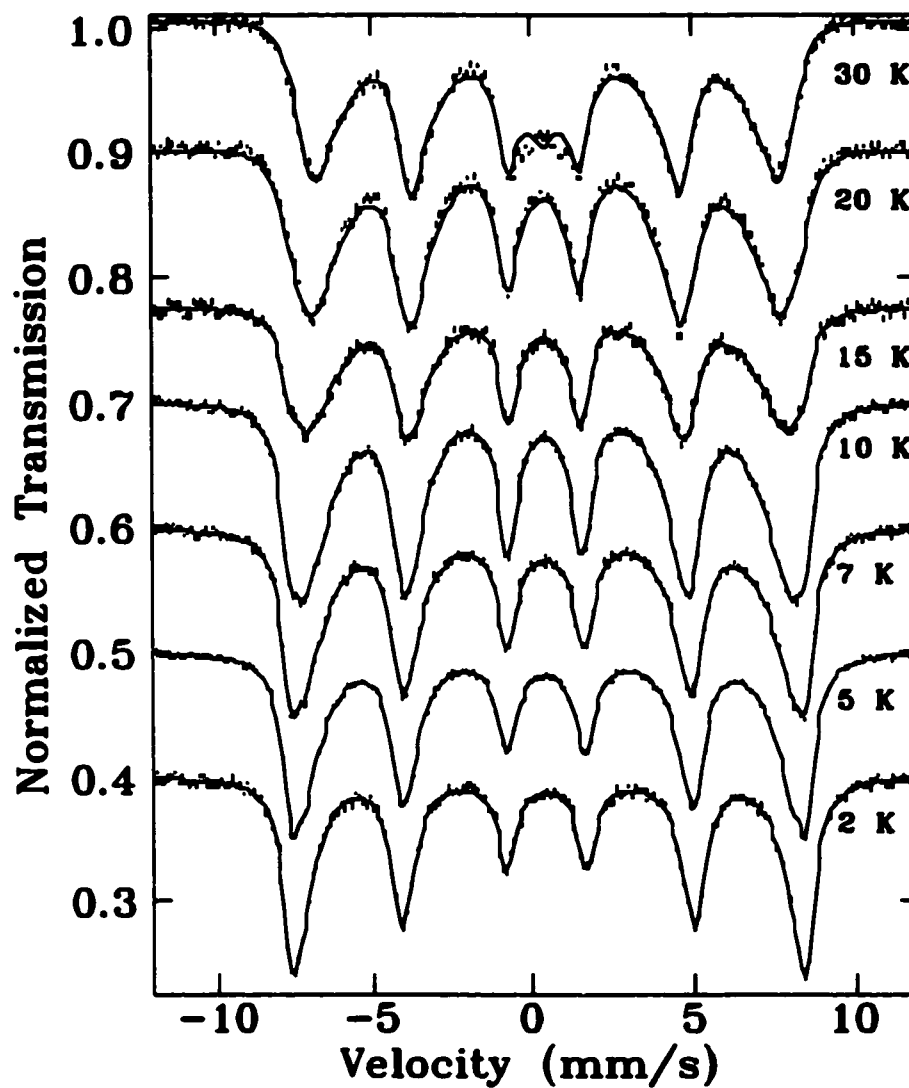
Figure 4.14: Mössbauer spectra of the polysaccharide iron complex (PIC). Our present model cannot predict the quadrapole doublet in the PIC and begins to fail around 30 K.

97

Sample	Γ (mm/s)	B_{hf}(T)	K ($\times 10^4 J/m^3$)	T_B (K)
4.5 nm ferrofluid	0.44±0.02	50.02±0.06	3.0±0.1	30±5
6.0 nm as-received ferrofluid	0.40±0.02	50.04±0.08	2.4±0.2	55±5
6.0 nm aged ferrofluid	0.409±0.006	50.1±0.2	1.9±0.2	50±5
PIC	0.339±0.008	49.99±0.06	1.1±0.2	10±2

Table 4.4: Summary of the fitted parameters, Γ, B_{hf} and K for the samples examined with our multiple-level model. T_B is established when $\nu_0 > 0$ (see Fig. 4.15).

hyperfine field, linewidth and relaxation rate.

The validity of our description is clearly visible in Figs. 4.11, 4.12 and 4.13. The model is able to reproduce the lineshape of the samples at all temperatures with small variations in the linewidth (Γ) and K. A consistent Γ when fitting using any magnetic relaxation formalism is crucial. Line broadening in a spectrum should be reflected by an increase in ν and not incorrectly compensated for by Γ. The paramagnetic spectrum of the akaganéite in the PIC exhibits a significant quadrapole splitting that cannot readily be included in our model. As a result, we were unable to fit the PIC spectra above 30 K (Fig. 4.14). The model correctly tracks the area of the central component with a singlet, but is simply unable to provide a doublet. Our present formalism assumes that the nuclear Hamiltonian that is fluctuating from moment oscillations commutes with itself at different times. To properly predict the lineshape of the PIC, a much more complex formalism needs to be devised that involves Liouville superoperators for solving the combined stochastic-quantum mechanical problem[62]. We did not fit PIC spectra above 30 K due to this shortcoming.

Fitted values for ν_0 and K are shown in Fig. 4.15, and extrapolated 180° moment flip rates in Fig. 4.16. Values of K are in agreement with similar magnetic fine particle systems[51, 52, 53] and PIC[58]. The lower value for K in the as-received 6.0 nm ferrofluid with respect to the 4.5 nm ferrofluid indicates stronger interparticle interactions[4, 46]. In general, stronger interparticle interactions are expected in systems with broader particle size distributions. The variation in K between the
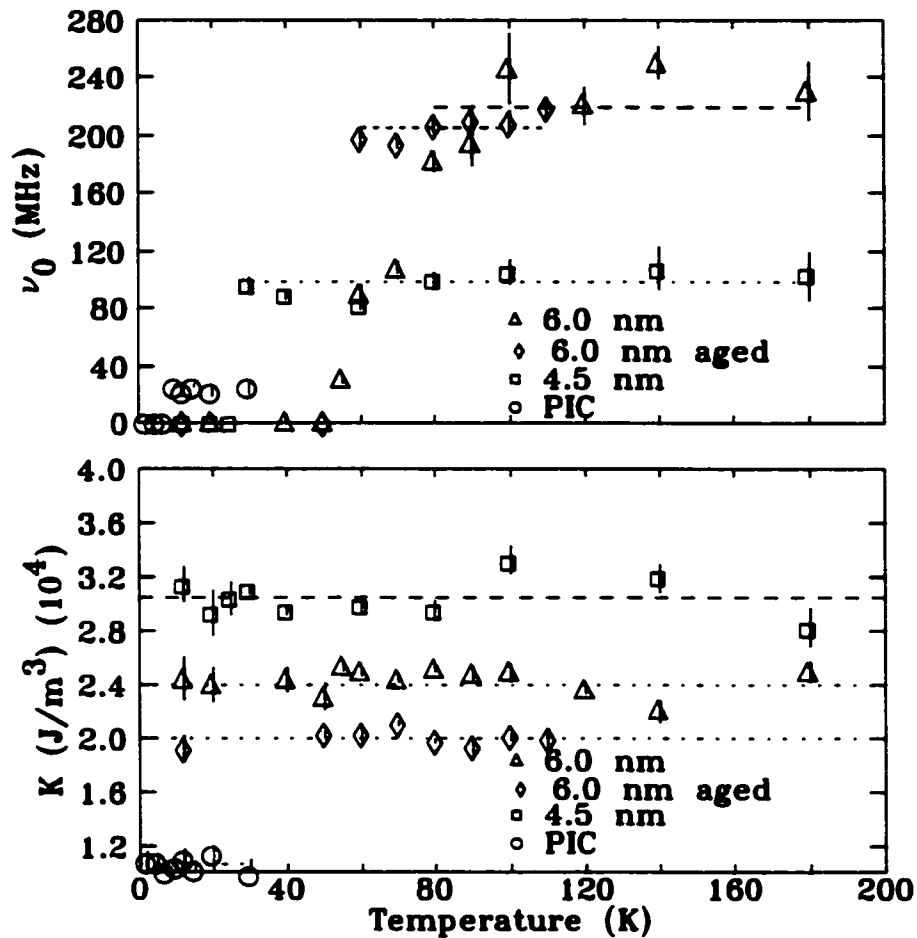
Figure 4.15: Plots of the pre-exponential factor of the relaxation time ν_0 and the anisotropy energy K. T_B is the point where $\nu_0 > 0$.

4.5 nm and 6.0 nm ferrofluid is compatible with this analysis. A lowered K and T_B for the 6.0 nm aged ferrofluid when compared to the 6.0 nm as-received ferrofluid is also consistent with stronger interparticle interactions, in agreement with our χ_{ac} measurements.

The temperature at which superparamagnetic relaxation began to occur, i.e. when $\nu_0 > 0$, established T_B for the Mössbauer spectra and is listed in Table 4.4 for the various samples. Comparison of these values with our χ_{ac} data, shown in Fig. 4.10, clearly demonstrates that T_B derived from our model of the Mössbauer spectra is fully consistent with other probes of magnetic relaxation. Effects of interparticle

interactions are again evident with the lowered value of T_B for the aged 6.0 nm ferrofluid compared to the as-received 6.0 nm ferrofluid[3].

Since $\nu_0 \propto 1/VM_s$[64], and M_s has been shown to exhibit a weak temperature dependence[4, 65], the often used assumption of a constant ν_0[65] is not strictly valid. We therefore treated ν_0 as a fitted parameter, however, ν_0 remained reasonably constant for a given sample across the range of temperatures, as shown in Fig. 4.15. A lower ν_0 for the 4.5 nm ferrofluid compared with the 6.0 nm ferrofluid is consistent with an increased M_s for smaller particles[60]. The slight reduction in ν_0 for the 6.0 nm ferrofluid on aging is consistent with an increase in M_s with interparticle interactions[50][60].
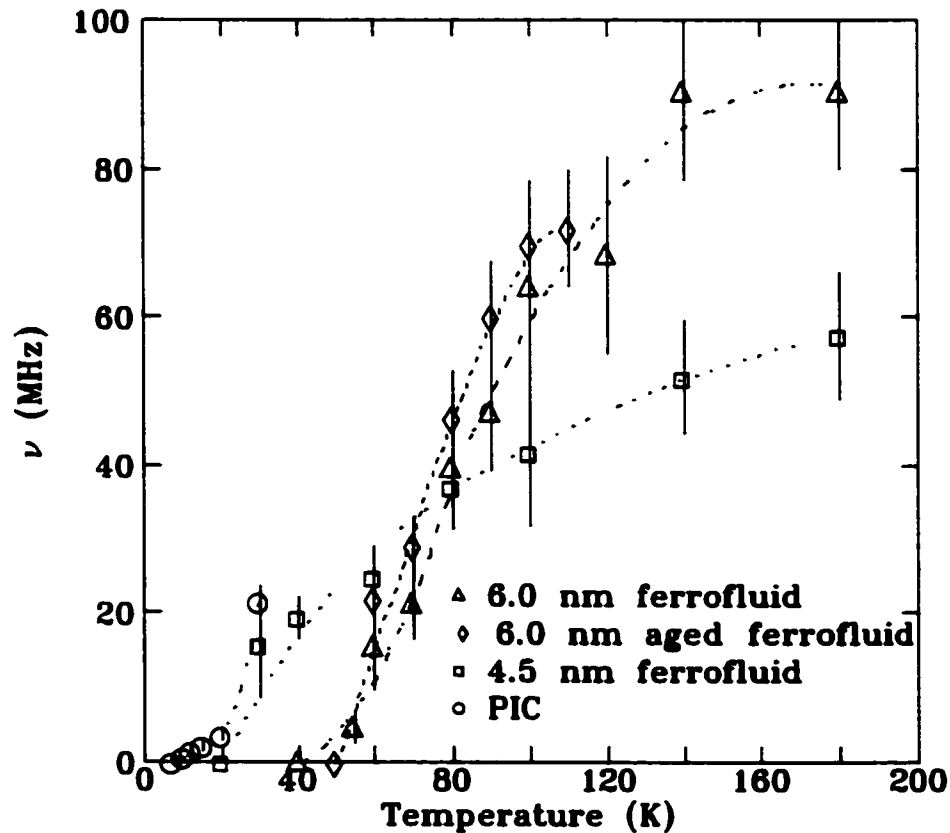
Figure 4.16: 180° moment flip relaxation rates determined from the many state model (normalized with respect to the log-normal size distribution). The expected gradual increase of flip rate with temperature for a superparamagnetic system is present.

100

The average moment flip rates for the spectra are plotted as a function of temperature in Fig. 4.16. The usual decrease of ν with temperature is observed, typical of magnetic relaxation. An increase of ν with stronger interparticle interactions between the 6.0 as-received and 6.0 aged ferrofluid is consistent with previous magnetization and χ_{ac} studies[4, 46].

The multi-level transmission Mössbauer spectra model indicates that at intermediate temperatures around T_B, superparamagnetic moment flips are present in the fine particle systems. The particles that have superparamagnetic moments should provide the SEDM spectral signature of magnetic relaxation that we were looking for (but did not see due to the static magnetism) in the $Fe_{65}Ni_{35}$ alloy. The temperatures at which the absorption sextet is well resolved in the transmission Mössbauer spectra has been established. At these temperatures it is possible to drive a specific energy transition, and SEDM spectra can be collected.

4.2.1 Selective excitation double Mössbauer studies

SEDM spectroscopy was used to study spin dynamics in the 4.5 nm and 6.0 nm Fe_3O_4 ferrofluids. The left-most line in the spectrum was pumped as it has the largest absorption cross-section, thus maximizing the signal and reducing collection times. Typical counting times were 20 days and data are shown in Figs. 4.17 and 4.18 for the 4.5 nm and 6.0 nm ferrofluids, respectively.

With the left-most line (line #1, $m_g = -\frac{1}{2} \rightarrow m_e = -\frac{3}{2}$ transition) driven, the $m_e = -\frac{3}{2}$ sublevel was selectively populated. In a static magnetic environment, the radiation is re-emitted when the excited Mössbauer nucleus decays, to the $m_g = -\frac{1}{2}$ ground state. This has been confirmed with α-Fe, a-$Fe_{80}B_{20}$, and $Fe_{65}Ni_{35}$. The low temperature transmission Mössbauer spectra of the ferrofluids (e.g. 12 K and 20 K in Figs. 4.11 and 4.12) fit with the multi-level model were consistent with static disorder. The 20 K SEDM spectra of the ferrofluids (Figs. 4.17 and 4.18) are consistent with the analysis of the low temperature transmission Mössbauer spectra. A single line in
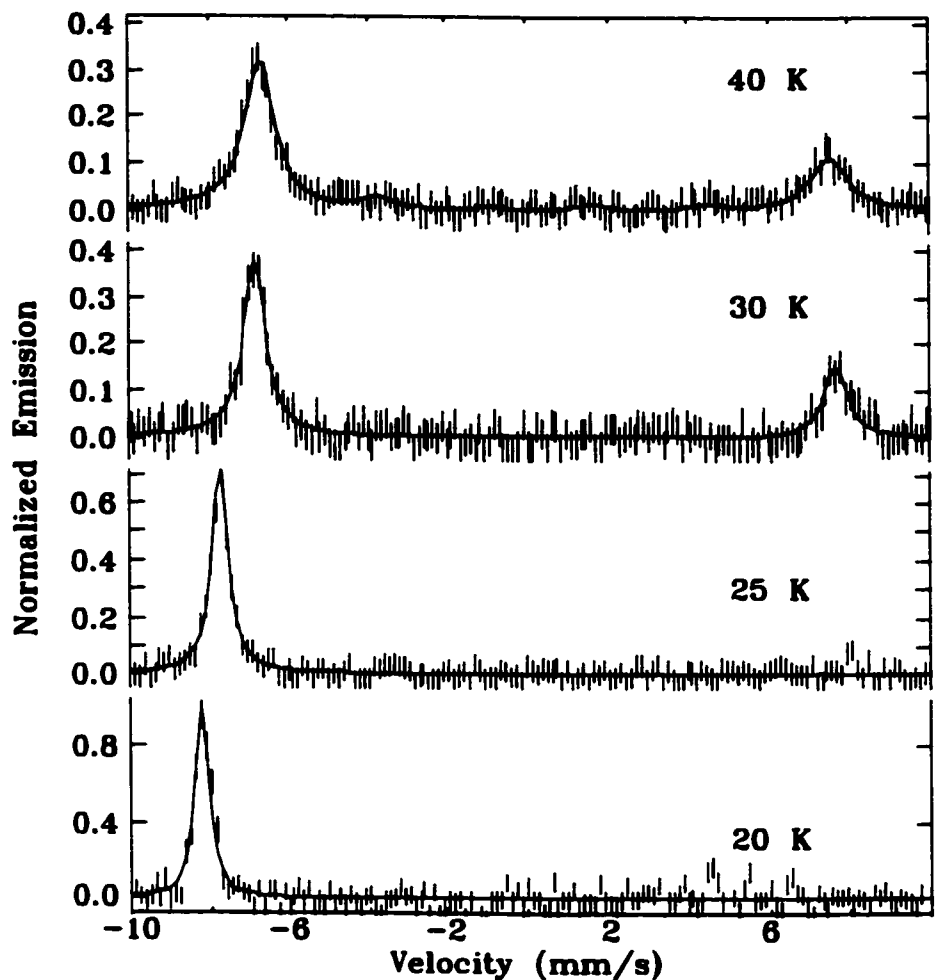
Figure 4.17: SEDM spectra of a 4.5 nm Fe_3O_4 ferrofluid. At each temperature, the pump energy was centered on the line at the left. The appearance of the peak at positive velocities indicates the onset of superparamagnetic moment reversals.

the SEDM spectra, at the pump energy, with a linewidth that is greater than that for α-Fe (Fig. 4.19 and 4.20) is the signature of static disorder, as we have measured in a-$Fe_{80}B_{20}$.

Collective magnetic excitations, which according to the multi-level transmission Mössbauer spectra model, occur at temperatures below T_B, affect the SEDM spectra of the ferrofluids in a new way. A further increase of linewidth for the observed line #1 transition occurs in Figs. 4.17 and 4.18, as shown in the fit results in Figs. 4.19 and 4.20. This linewidth broadening happens above 25 K for the 4.5 nm ferrofluid
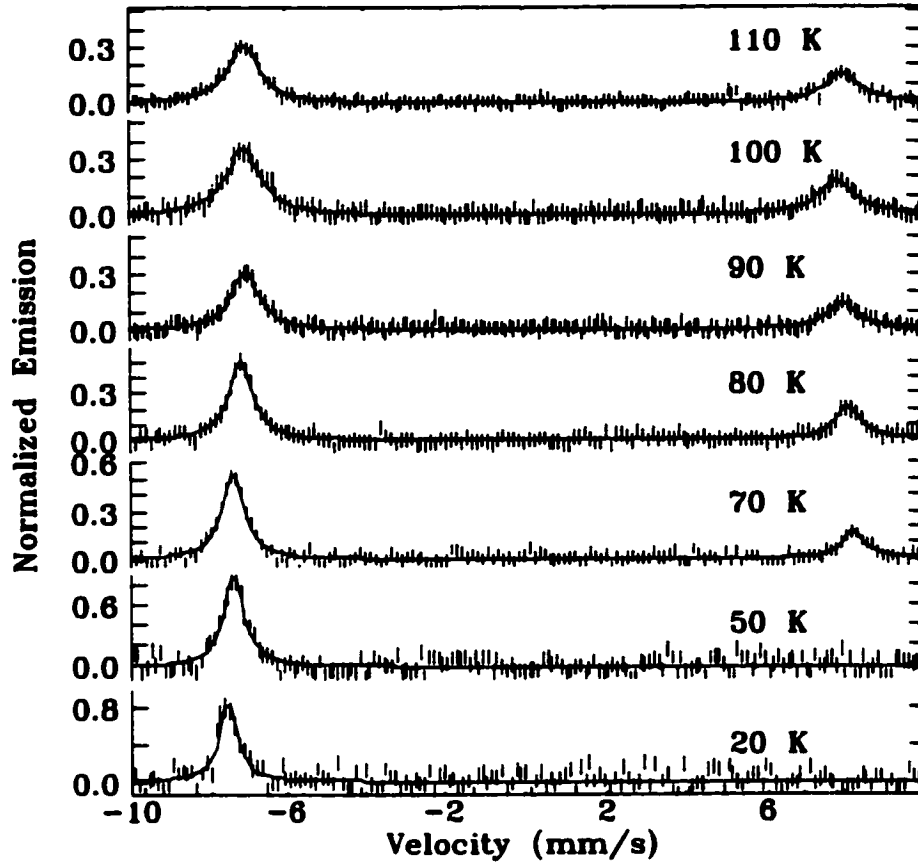
Figure 4.18: SEDM spectra of a 6.0 nm Fe_3O_4 ferrofluid. At each temperature, the pump energy was centered on the line at the left. The appearance of the peak at positive velocities indicates the onset of superparamagnetic moment reversals.

and 30 K in the 6.0 nm ferrofluid. If the line broadening of the spectrum at each temperature (where only line #1 is present) is treated as occurring simply from static disorder (i.e. using Eqn. 3.16), fitted linewidths of $\Gamma = 0.20 \pm 0.01$ mm/s for the 4.5 nm ferrofluid, and $\Gamma = 0.215 \pm 0.005$ mm/s for the 6.0 nm ferrofluid, result. This is in striking conflict with the $\Gamma = 0.165 \pm 0.002$ mm/s of the $a\text{-}Fe_{80}B_{20}$ alloy and $\Gamma = 0.167 \pm 0.005$ mm/s for the $Fe_{65}Ni_{35}$ alloy which were completely characterized by a distribution of hyperfine fields. The fitted Γ's of the ferrofluids, assuming static disorder, are much too large to simply describe the lifetime of the Mössbauer nucleus excited state and the CED linewidth. These results are consistent with Mørup's description of collective excitations[1], where motional narrowing creates an effective
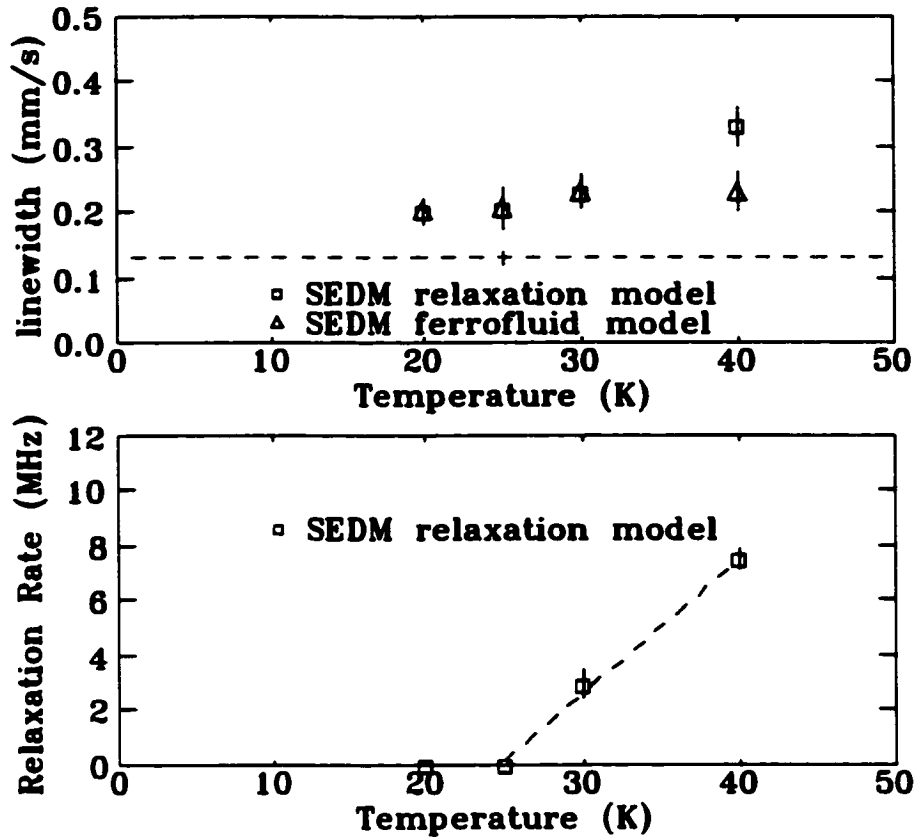
Figure 4.19: Results of fits to the data using two SEDM models. The dashed line shows the linewidths obtained by SEDM on α-Fe. Relaxation rates show the onset of superparamagnetic spin-flips above $T_B=27\pm2$ K for the 4.5 nm ferrofluid.

time-independent hyperfine field. Collective excitations are the most likely candidate for the observed line broadening that cannot be fitted assuming a simple static distribution of hyperfine fields. These are the first *model-independent* observations of collective excitations.

Superparamagnetic spin-flips have the most dramatic effect: for the 4.5 nm ferrofluid (Fig. 4.17) a new line is clearly present at 30 K, and for the 6.0 nm ferrofluid (Fig. 4.18) at 70 K a new line is distinct in the SEDM spectrum. These lines at $\sim +8$ mm/s, are due to the $m_e = +\frac{3}{2} \rightarrow m_g = +\frac{1}{2}$ (line #6) transition, and are present even though we have explicitly populated only the $m_e = -\frac{3}{2}$ excited state. This is possible because when a spin flip occurs in a particle in which we have pumped a nucleus into the $m_e = -\frac{3}{2}$ excited state, the field within that particle reverses,
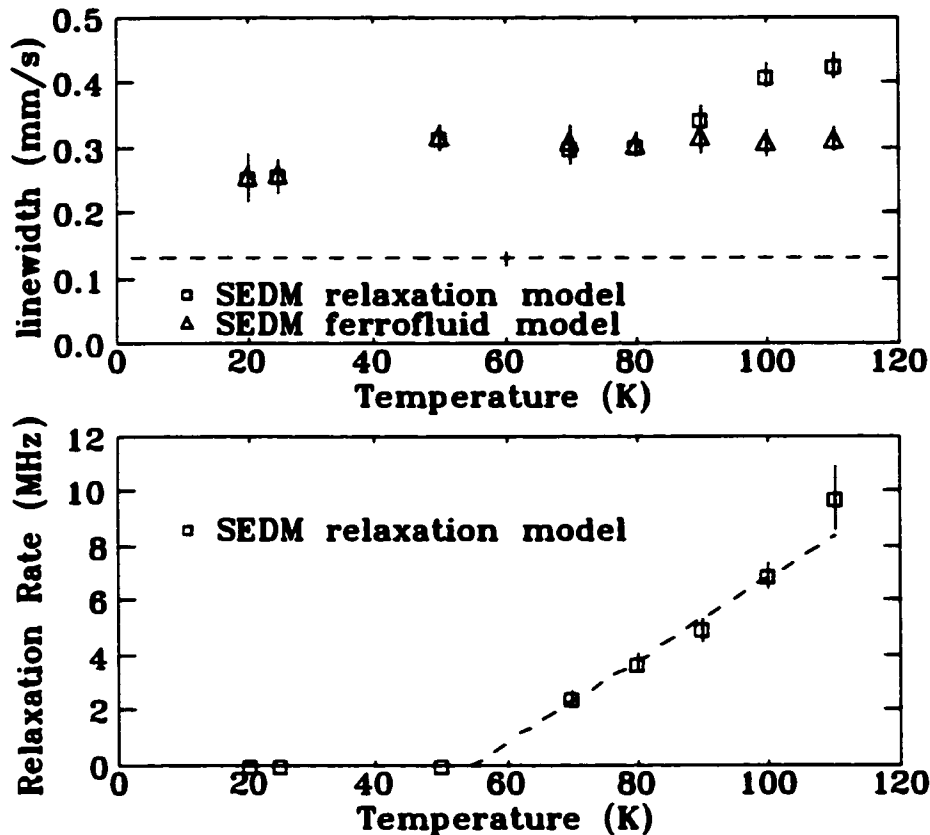
Figure 4.20: Results of fits to the data using two SEDM models. The dashed line shows the linewidths obtained by SEDM on α-Fe. Relaxation rates show the onset of superparamagnetic spin-flips above $T_B=54\pm3$ K for the 6.0 nm ferrofluid.

the projection of I_e onto that field changes sign, and the populated state becomes $m_e = +\frac{3}{2}$. This state then decays to give the line at $\sim +8$ mm/s. The observation of a *sharp* line at $\sim +8$ mm/s indicates that the moment reversal is instantaneous on the timescale of the SEDM measurement. The intensity ratio of the lines at ~ -8 mm/s and $\sim +8$ mm/s is related to the probability that a spin flip occurs during the lifetime of the excited state and thus is a direct indication of the rate at which spin flips are occurring. We must emphasize that no amount of *static* disorder can lead to the appearance of line #6 in the spectra. It can *only* be caused by magnetization reversals.

The superparamagnetic spin flips occur with increasing frequency above T_B. Blocking temperatures of $T_B = 27\pm2$ K for the 4.5 nm ferrofluid and $T_B = 54\pm3$ K for the

6.0 nm ferrofluid are extrapolated from linear fits to the SEDM relaxation rates using Eqn. 3.21. These T_B's are in excellent agreement with transmission Mössbauer and frequency dependent χ_{ac} extrapolations of T_B (Fig. 4.10). However, the continued increase in linewidth as the relaxation rate increases indicates that our model is too simple. A correct description of the superparamagnetic processes should involve no linewidth variations.

A distribution of relaxation rates for each moment size was used in the multi-level relaxation model to fit the ferrofluid transmission Mössbauer spectra (Sec. 4.2). Since the transmission experiments are sensitive to moment flips that are about or above the Larmor frequency and SEDM is sensitive to moment flip that are about or below the Larmor frequency, relaxation rates from the transmission Mössbauer spectra multi-level model within the time scale of the SEDM measurement can be used to fit the SEDM spectra. These fits are shown in Figs. 4.19 and 4.20, and a more consistent linewidth results.

SEDM spectroscopy on the 4.5 nm and 6.0 nm Fe_3O_4 ferrofluids has provided the spectral signature of moment flips that we have been searching for. The lineshape for $180°$ moment flips predicted by our SEDM model in Eqn. 3.21 has been experimentally verified. Fits to the SEDM ferrofluid spectra provide the first *model-independent* measurements of relaxation rates of single domain particles, and the first model-independent measurement of collective excitation has been made. Agreement between SEDM relaxation rates and transmission Mössbauer spectra multi-level fits further support our model in Sec. 3.1.

Additional insight into the spin dynamics of magnetic fine particle systems is possible using a different probe of the time-independent and time-dependent hyperfine interactions. Such an experimental probe is provided by zero-field muon spin relaxation (ZF-μSR). With a measuring time that overlaps the Mössbauer effect (Fig. 1.8), comparison, for example, between relaxation rates extrapolated using the multi-level transmission Mössbauer spectra model and ZF-μSR results, can be made.

106
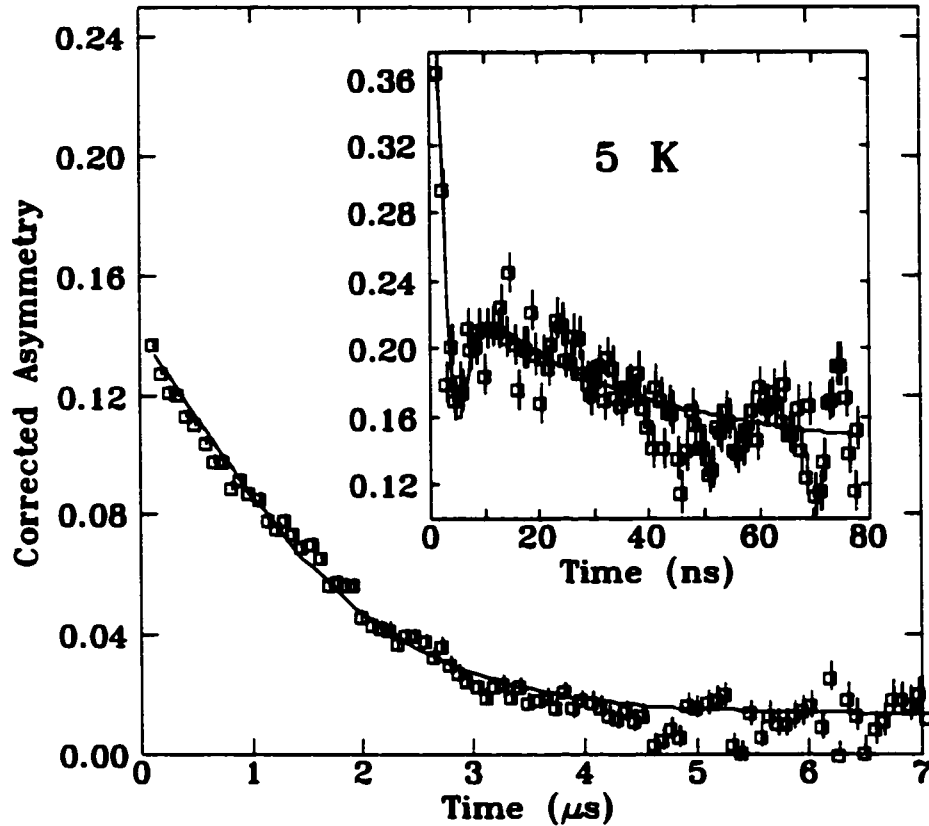
Figure 4.21: Typical μSR spectra for PIC at 5 K. Inset shows the early time region of the data where the static K-T minimum with fast relaxation is observed. Solid lines are fits to functions described in the text.

4.2.2 Muon spin relaxation studies

Spin dynamics were examined with ZF-μSR in the ferritin analogue, an akaganéite (β-Fe^{+3}O(OH)) based polysaccharide-iron complex (PIC) called Niferex[49] With a blocking temperature which was below the lowest temperature available with our SEDM scattering closed cycle refrigeration system, the transmission Mössbauer spectra analysis of the PIC with the multi-level model, had not been tested. Moreover, since the PIC was a powder, not a messy oil-based sample, no special sample holder was necessary.

Typical μSR spectra for PIC are shown in Fig. 4.21. Magnetic fluctuations couple to the muon spin and cause an exponential decay of the observed polarization. The

inset shows that this exponential decay changes character at early times. A characteristic K-T minimum is observed, indicating the presence of static magnetic order. As PIC is a synthetic complex of akaganéite with a carbohydrate shell, and has an iron content of approximately 50%[58] by weight, it is plausible to expect one contribution from the carbohydrate shell and another approximately equal contribution to be due to the akaganéite. Muon depolarization from the static moments in the core will result in a K-T lineshape. Stray field effects from the antiferromagnetic core should be negligible, so the diamagnetic carbohydrate shell will have a small internal field and muon depolarization from the shell should exhibit a temperature independent relaxation.

We have fitted the PIC μSR spectra with the following lineshape:

$$A = A_0\{\zeta G_d(\lambda_1) \times G_s(\Delta) + (1 - \zeta)G_d(\lambda_2)\} \tag{4.1}$$

where G_s and G_d are given in Eqn. 3.46, with A_0 the initial instrumental detector asymmetry, and ζ the fraction of the two spectral components. Examining Fig. 4.21, we see that this accurately models the spectral lineshape. A fitted $\zeta = 0.53\pm0.03$ is in agreement with the weight ratio of the ferric and carbohydrate components of PIC. Fit results are shown in Fig. 4.22. At the lowest temperatures, a large Δ indicates blocked magnetic moments of the larger particles in the PIC. At 10 K, Δ begins to decrease as these moments begin to unblock from thermal fluctuations that cause the average static moment to decrease[80]. Above 10 K, a larger fraction of moments begin to unblock until, by 20 K the small Δ indicates that all but the largest particles have unblocked.

Spin dynamics at temperatures below 10 K consist of the particles in the PIC undergoing collective excitations. These collective excitations result in the small values of $\lambda_1 \sim 40$ MHz. As the muon is sensitive to a wider range of measuring frequencies, collective excitations that appear motionally narrowed during the ~ 10 MHz measuring frequency of the Mössbauer effect will exhibit dynamic behavior with μSR. This behavior is due to the muons fluctuating along with the nearby moments undergoing
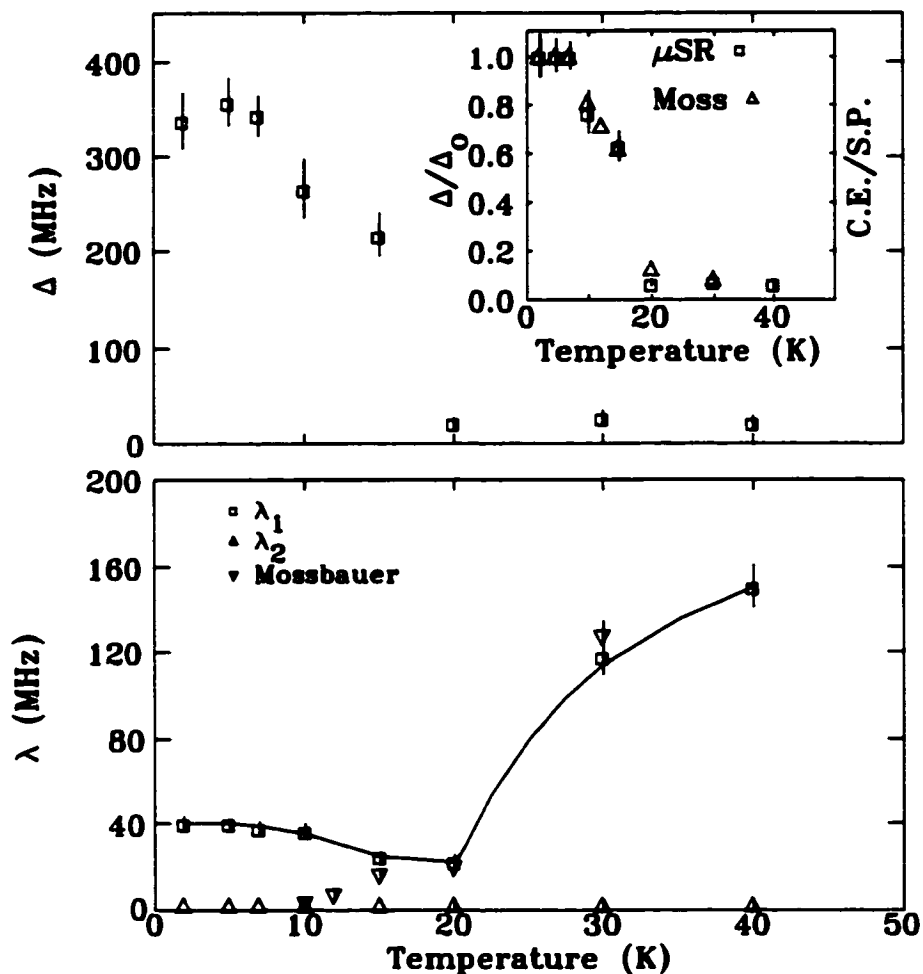
Figure 4.22: Temperature dependence of the static (Δ) and dynamic (λ) relaxation rates in PIC. The decrease in Δ and increase in λ indicate when moments begin to unblock at T_B. Notice the similar ratio of moments undergoing collective excitations (C.E.) and superparamagnetism (S.P.) from the Mössbauer model and μSR (Δ/Δ_0) results (inset to top plot) and agreement of relaxation rates from the μSR (□) and transmission Mössbauer fits (△). The solid line is a guide to the eye.

collective excitations. The trend is direct confirmation of Mørup's collective excitation model which assumes that the moment fluctuations are faster than the Mössbauer effect measuring frequency[1]. The effective range of hyperfine fields which was indicated by line broadening in the SEDM results on the 4.5 nm and 6.0 nm Fe_3O_4 ferrofluid samples, that could not be fitted assuming simple static disorder, is also evidence of collective excitations. These ZF-μSR results offer additional, indepen-
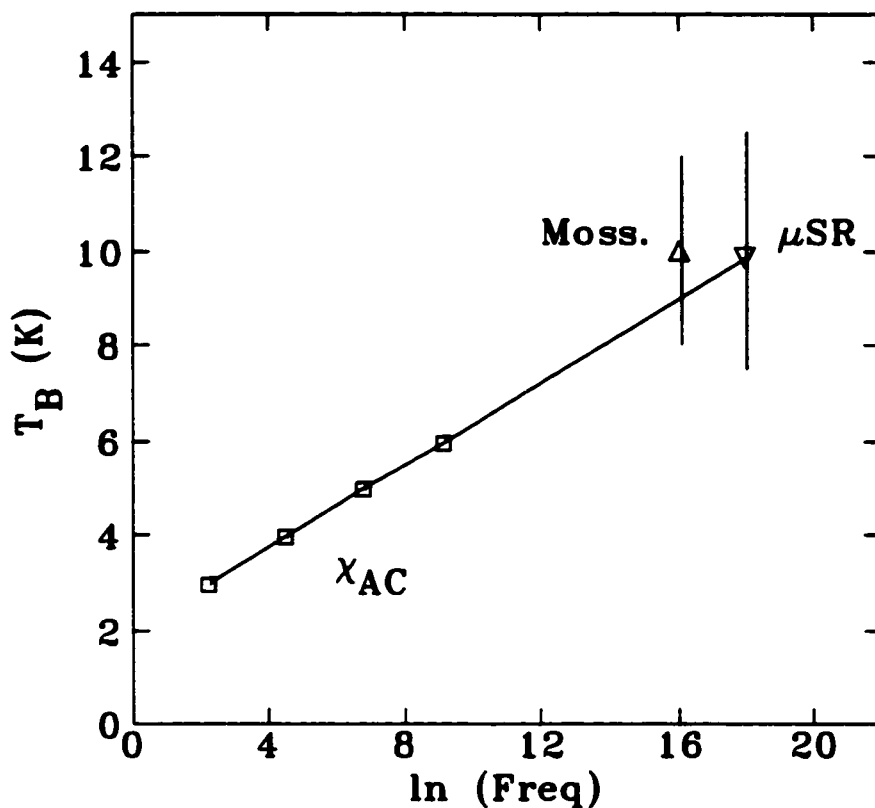
Figure 4.23: Plots of T_B versus measurement frequency for the ZF-μSR , χ_{ac} measurements and Mössbauer multi-level model.

dent, confirmation of the presence of collective excitations in moments which are at temperatures below T_B.

When particles begin to unblock at 10 K, a small decrease in the measured relaxation rate of the iron particles occurs. As the number of particles that are undergoing superparamagnetic spin flips increases with temperature, the fraction of the depolarization from the superparamagnetic moments becomes larger than the component from moments that are undergoing collective excitations. At $\sim$ 15 K, more moments are undergoing slow superparamagnetic relaxation then collective excitations, and a small decrease in λ_1 occurs. As more moments become superparamagnetic, λ_1 increases dramatically. The fitted relaxation rates are in good agreement with those used to fit the transmission Mössbauer spectra (Fig. 4.22). The ratio of moments undergoing collective excitations and those that are superparamagnetic in the particle distribution determined from the μSR data (Δ/Δ_0 where $\Delta_0 = \Delta$ extrapolated to 0

K) and transmission Mössbauer model are in good agreement (see inset to Fig. 4.22).

To compare blocking temperatures between χ_{ac}, transmission Mössbauer and μSR results it is necessary to establish the measuring time of the muon when moments begin to unblock. First we must assume some sort of formulation for the time-dependent perturbations of muons. The simplest description is given by Fermi's Golden Rule[80]

$$W \simeq (\gamma_\mu B_{hf})^2 J(\omega) \qquad (4.2)$$

where W is the transition probability between two spin states (remember the muon is a spin $\frac{1}{2}$ particle) and $\omega = \gamma_\mu B_{hf} = \Delta/2\pi$. We assume that the spectral density of muon fluctuations, $J(\omega)$, follows a simple Lorentzian form, i.e.

$$J(\omega) = \frac{\tau_m/\pi}{1 + \omega^2 \tau_m^2} \qquad (4.3)$$

where τ_m is the measuring time of the muon. Since the dynamic range accessible to μSR measurements is centered roughly on the inverse muon lifetime, $0.01 < \lambda < 100\mu s^{-1}$, and depends on the magnitude of the local field, we need to know what the corresponding window of relaxation times is. As we are using $G_d(t)$ of Eqn. 3.46, the fast fluctuation limit (e.g. where the full dynamic Kubo-Toyabe model is *not* needed to describe μSR spectra) is appropriate, and we have[80]

$$\tau_m = \frac{\lambda}{(\Delta/(2\pi))^2} \qquad (4.4)$$

For the PIC, $\tau_m = 1.3 \pm 0.3 \times 10^{-8}$ s at 10 K. This calculated τ_m and $T_B = 10 \pm 2.5$ K are in excellent agreement with T_B extrapolated from frequency dependent χ_{ac} results and our multi-level transmission Mössbauer model, shown in Fig. 4.23.

Finally, the carbohydrate coating of the PIC results in a slow temperature independent relaxation with $\lambda_2 = 0.58 \pm 0.02$ MHz, which we believe to be consistent with slow dipole moment fluctuations of muons in this coating.

These ZF-μSR results have provided further confirmation of the multi-level model of transmission Mössbauer spectra for fine particle systems. The ratios of static to

111

dynamic moments in the PIC derived from the transmission Mössbauer spectra multi-level fits and the μSR fits are in excellent agreement, more evidence that our description of magnetic behavior is correct. Superparamagnetic relaxation rates determined with μSR are in excellent agreement with transmission Mössbauer spectroscopy fits. Further, model independent, confirmation of collective excitations has been provided with μSR. The blocking temperature extrapolated with μSR, in agreement with our χ_{ac} and multi-level transmission Mössbauer fits, is further evidence that the equal area criteria of T_B for transmission Mössbauer spectra (which indicated a $T_B = 60 \pm 5$ K) is a remarkably poor measure of T_B. This study of magnetic fine particle systems is distinguished by the consistent analysis of static and dynamic magnetic behavior using different experimental techniques.

4.3   Frustrated Magnets

We have examined systems which posses only static magnetic disorder or dynamic magnetic disorder. Our next investigation of a disordered magnet will center on a system that contains, simultaneously, both time-independent and time-dependent disorder. Static and dynamic disorder occur in partially frustrated magnetic systems. Exchange frustration occurs when the magnetic moments in a material experience conflicting interactions[20] due to the presence of both ferromagnetic and antiferromagnetic exchange interactions. A ferromagnet posses simple ferromagnetic interactions between magnetic moments. When a certain amount of antiferromagnetic interactions are randomly introduced into a ferromagnetic system so that the average interaction is zero (a state called complete frustration) the system becomes a spin-glass. A spin-glass is characterized by random orientations of spins (zero magnetization) and very slow dynamics. If a material contains both ferromagnetic and antiferromagnetic interactions, but the bias is towards ferromagnetic interactions, the systems shows a complicated magnetic behavior which sits between that of a ferromagnet and spin-glass.

Partially frustrated magnets undergo a transition at T_C which marks the onset of long-range ferromagnetic order from the high-temperature paramagnetic state. This transition is readily observable with transmission Mössbauer and μSR spectroscopy. A second transition at T_{xy} denotes the freezing of the transverse degrees of freedom of magnetic moments. This transverse spin freezing is easily measured with ZF-μSR, however, although the effects on the average moment can be measured with transmission Mössbauer spectroscopy[22], a direct measure of the time-dependent effects of the spin freezing on the hyperfine interactions is only possible with SEDM. Now that we know how to identify static and dynamic magnetic behavior using transmission Mössbauer, SEDM and ZF-μSR spectroscopy, we apply these techniques to the a-Fe_xZr_{100-x} frustrated magnet system that simultaneously contains both time-independent and time-dependent magnetic phenomena.

Spin dynamics were studied in the a-Fe_xZr_{100-x} system with μSR and SEDM spectroscopy. Samples were prepared as 1–2 mm wide meter-length ribbons. Appropriate amounts of pure elements were arc melted under Ti-gettered argon and then melt spun in 40 kPa helium with a wheel speed of 55 m/s. Sample compositions were checked by electron microprobe and found to be $\sim$ 0.1 atomic % Fe-rich of nominal composition in all cases. Cu K_α x-ray diffraction on a powder diffractometer, and room temperature Mössbauer spectroscopy were used to confirm the absence of crystalline contamination. Basic characterization was carried out on a commercial extraction magnetometer and T_C was found to be consistent with standard values [23].

The μSR data in Fig. 4.24 of $Fe_{91.5}Zr_{8.5}$ illustrate a primary strength of μSR: both static and dynamic magnetic effects can be observed simultaneously and are sufficiently well separated in the spectra so as to be readily distinguished with reliability. In Fig. 4.24 the static K-T contribution is confined to the first 20 ns of the data while the dynamic decay is spread over the remaining 5 μs.

Since the a-Fe_x-Zr_{100-x} system is both structurally disordered (i.e. glassy) and magnetically disordered as a result of exchange frustration, a distribution of local fields is expected. As a result, the functional form described by Eqn. 3.46 was used
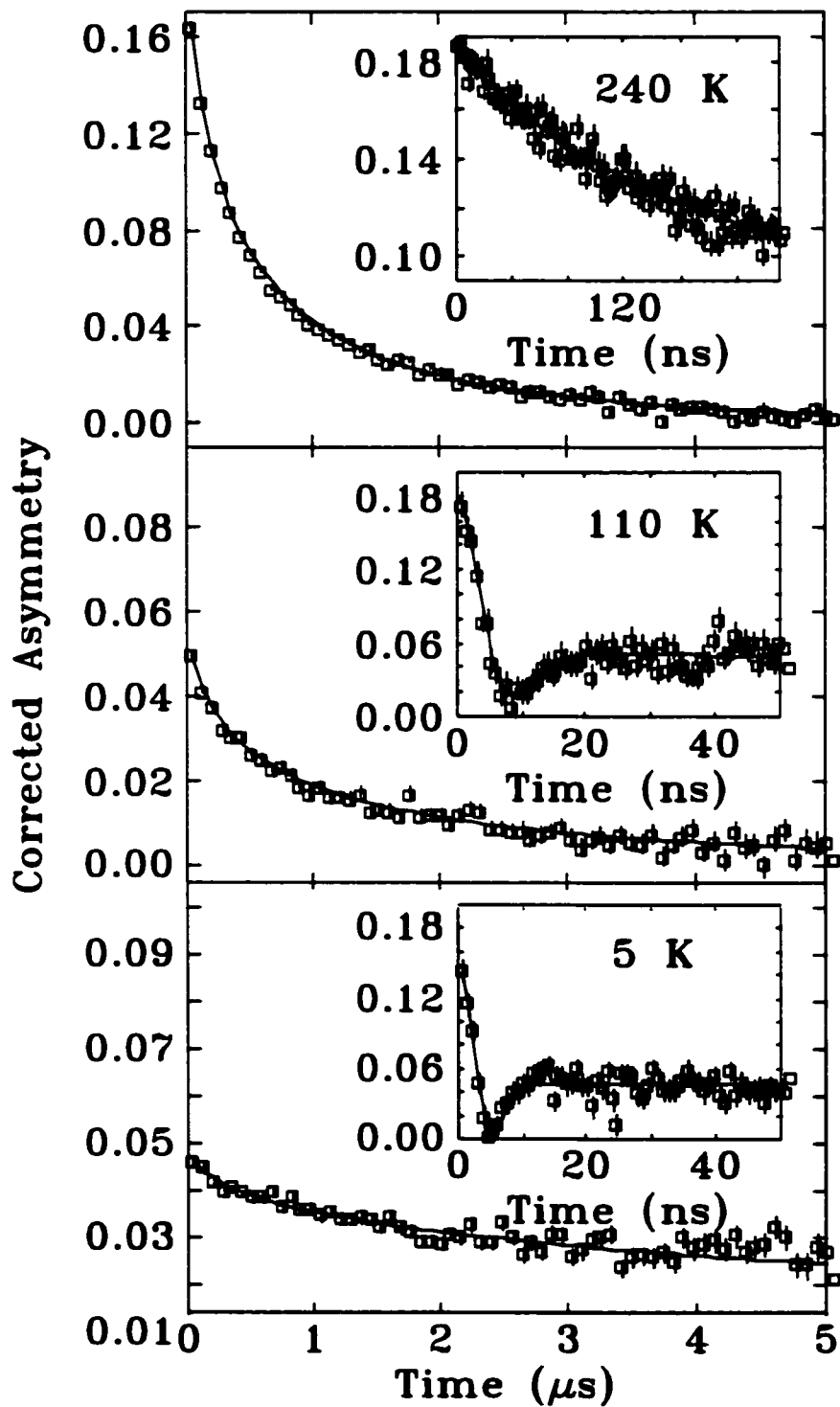
Figure 4.24: Typical μSR spectra for a-Fe$_{91.5}$Zr$_{8.5}$ at 240 K (above T$_C$), 110 K (below T$_C$ but above T$_{xy}$) and 5 K (below T$_{xy}$). Insets show the early time region of the data where, for T<T$_C$, the static K-T minimum is observed. Solid lines are fits to functions described in the text.

114

to describe the depolarization of muons in the samples.

To fit the static (early time channels) component of the μSR spectra, at T_C, $\alpha = 1$ was used to describe the Lorentzian K-T functional form of the spectra. Within 30 K of T_C, a Gaussian distribution of local fields, with $\alpha = 2$, described the spectra. This variation of α around T_C indicates a change in the local moment distribution when the collinear static order is established below T_C. The dynamic decay exhibited in the later time channels of the spectra were consistently fitted with $G_d(t)$ of Eqn. 3.46, an exponential decay of the asymmetry.

Fits of the dynamic relaxation rates (λ) are shown for each alloy in Fig. 4.25. λ as a function of temperature clearly shows the evolution of the system from a ferromagnetic at $x = 89$ to a spin-glass at $x = 93$. T_C is denoted by a clear cusp in $\lambda(T)$ that moves down in temperature with increasing frustration. Simultaneously, a broad feature at lower temperatures develops when $x \geq 90$. This peak grows in amplitude and moves to higher temperatures with increasing frustration (x), with the peak at T_C merging with this lower temperature feature as the system becomes a spin-glass at $x = 93$. These results are in perfect agreement with both qualitative descriptions of transverse spin freezing[22], and numerical simulations ([21], Fig. 1.7), where a broad noncritical fluctuation peak at T_{xy} as the transverse spin components order is predicted.

The behavior of Δ as a function of temperature in Fig. 4.26 also show the progression from ferromagnet to spin-glass. For $90 \geq x \geq 92$ where transverse spin freezing occurs, there is a break in the slope at which the lower temperature peak in $\lambda(T)$ happens. Most importantly, Δ increases with cooling through T_{xy}, indicating local order must grow as transverse components of the spins freeze. This is another clear sign that transverse spin freezing is happening. The existence of local ferromagnetic order has been confirmed with neutron depolarization[86, 87] studies that show long range ferromagnetic order is not lost below T_{xy}.

Transition temperatures derived from $\lambda(T)$ and $\Delta(T)$ are shown in Fig. 4.27. The agreement between the static and dynamic μSR results and χ_{ac} data confirms that

115
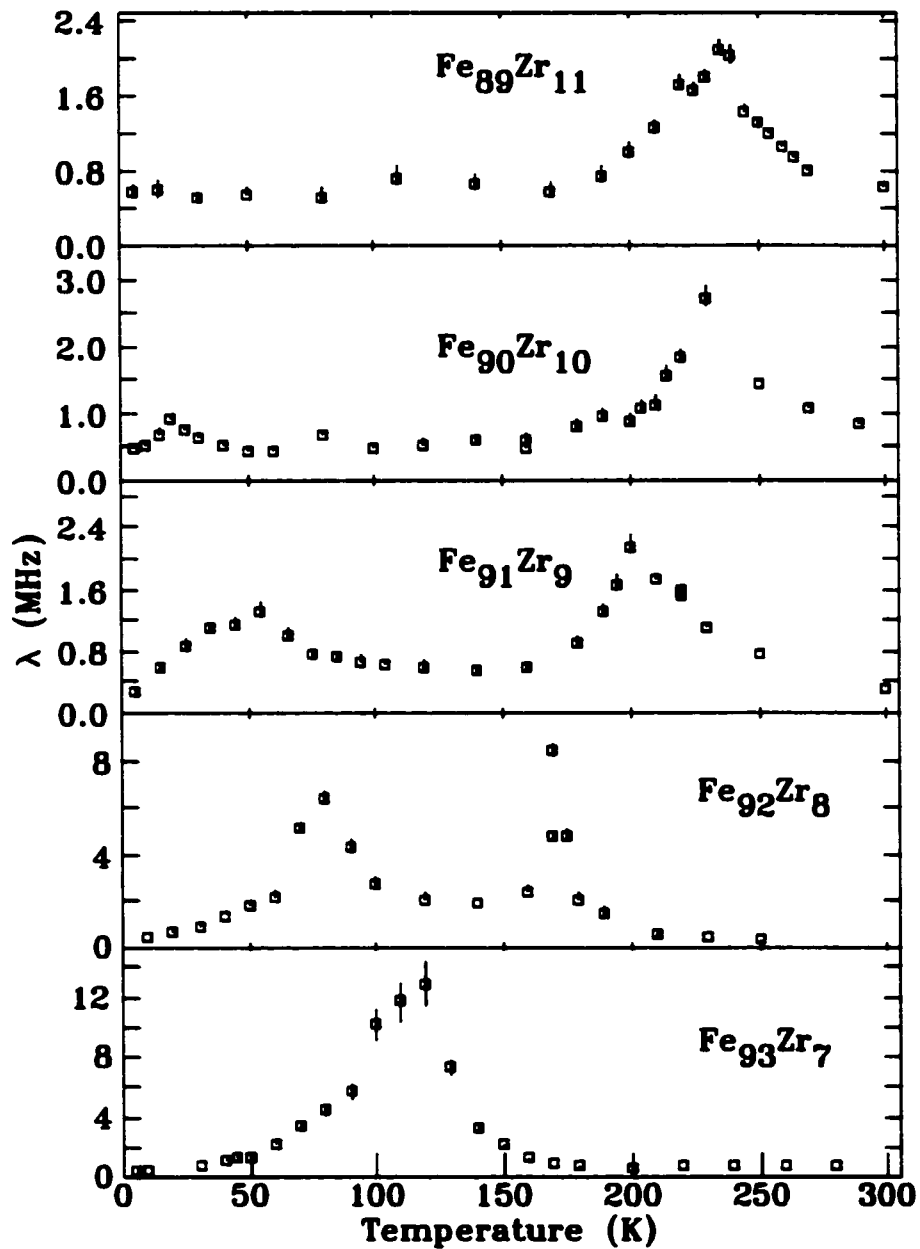
Figure 4.25: Temperature dependence of the dynamic relaxation rate (λ) showing the high temperature cusp at T_C merging with the lower temperature feature of T_{xy} with increasing frustration.
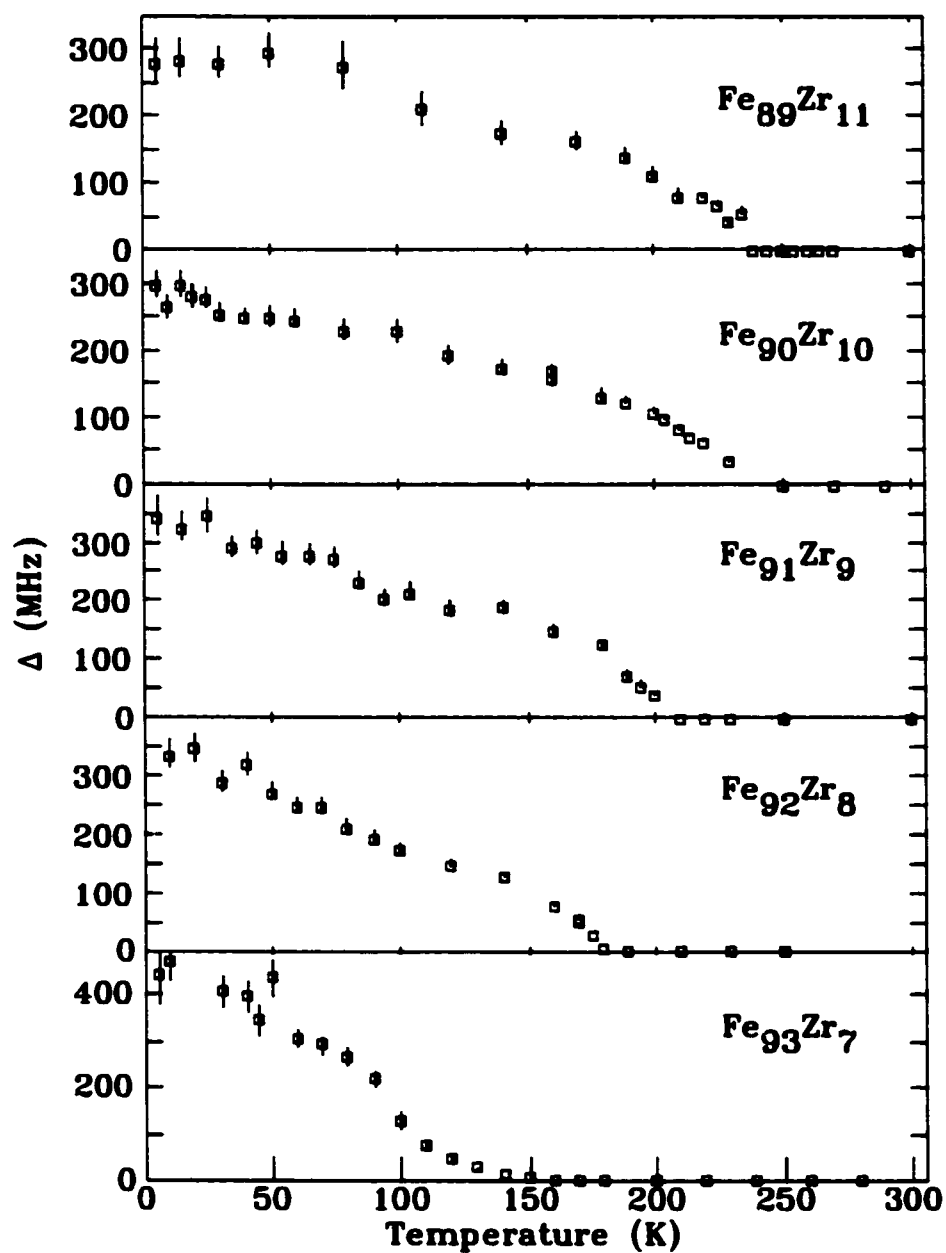
Figure 4.26: Temperature dependence of the static relaxation rate, Δ, showing the steady reduction in ordering temperature with increasing frustration and exhibiting the effects of transverse spin freezing for $90 \geq x \geq 92$.

117
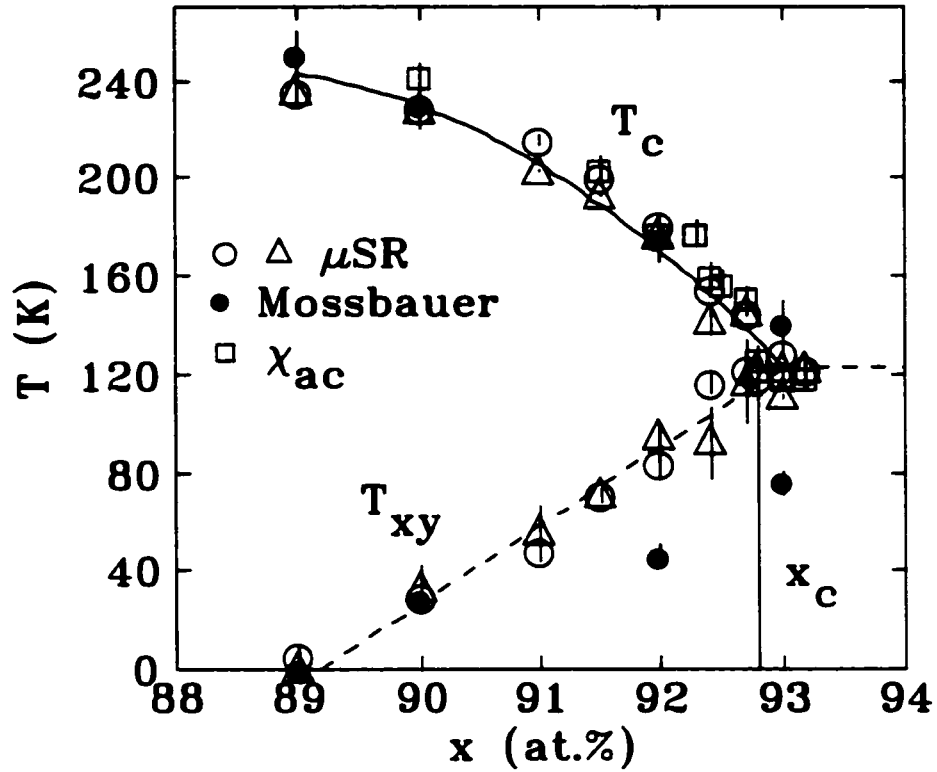
Figure 4.27: Magnetic phase diagram for a-Fe_xZr_{100-x} showing T_C and T_{xy} deduced from μSR data. $\circ$ denote values derived from the peak in λ while $\triangle$ reflects the values derived from fitting $\Delta(T)$[23]. T_C derived from χ_{ac} results are marked by $\square$. The solid symbols represent values derived from applied-field Mössbauer spectroscopy[22].

the onset of order at T_C is being detected by the muon precession signal. $\lambda(T)$ and $\Delta(T)$ both yield the same value for T_{xy}[23], showing that the lower fluctuation peak is associated with changes in the static order, as predicted by numerical simulations[21]. In all cases however, T_{xy} is much more easily defined by the peak in λ that from a change in the decay of $\Delta(T)$. This underlines the necessity of using a technique that is simultaneously sensitive to both static and dynamic moment behavior.

Examining Fig. 4.27, comparison of applied-field transmission Mössbauer results[22] with ZF-μSR data, reveals that the applied-field results are suppressed in temperature with increasing frustration. This gap grows with increasing frustration. Onset of spin freezing is clearly discernible in the Mössbauer data, so it is unlikely that this T_{xy} difference is due to misinterpretation of Mössbauer results. This gap grows

larger with increasing frustration, the effect becoming most severe in the system at the critical concentration of $x = 93$ (where T_C and T_{xy} merge in the μSR data) with the applied-field Mössbauer data showing a 40% decrease in T_{xy} with respect to the ZF-μSR result. This trend exhibits a suppression of transverse spin freezing with an applied field and has been confirmed with longitudinal field μSR measurements on $Fe_{92}Zr_8$[88].

The ZF-μSR results indicate a clear moment fluctuation peak at T_{xy}. Transmission Mössbauer spectra do not provide clear evidence of these spin fluctuations as the lineshape is dominated by the collinear, static disorder that begins below T_C[22] (Fig. 4.28). With this static disorder, and the left-right symmetry of a transmission Mössbauer spectrum, discerning the effects of magnetic fluctuations is problematic. Now that the mark of spin flips on a SEDM spectra have been measured, as well as the effects of static disorder, we can collect SEDM spectra of the a-Fe_xZr_{100-x} system at temperatures (demonstrated by the ZF-μSR results) where transverse spin freezing occurs.

The a-$Fe_{92}Zr_8$ sample exhibited the most distinct fluctuation curve around T_{xy} (Fig. 4.25) and was was studied with SEDM spectroscopy to examine spin dynamics from spin freezing. Typical counting times were 14 days with the 2 GBq source and the spectra are shown in Fig. 4.29.

The static disorder in the a-$Fe_{92}Zr_8$ sample leads to broadened absorption lines, shown in the low temperature transmission spectra of Fig. 4.28, and is correctly described by an asymmetric distribution of hyperfine fields, $P(B_{hf})$. If the constant velocity drive is set to an energy corresponding to the leftmost line in the 20 K spectrum, then the $m_g = -\frac{1}{2} \rightarrow m_e = -\frac{3}{2}$ (line #1) transition is driven and the $m_e = -\frac{3}{2}$ excited state in the sample is populated. The selection rules will allow only a single transition from this state into the $m_g = -\frac{1}{2}$ state to happen, and the excited nucleus will return to the ground state with the same energy as the pump, resulting in a single line at the pump energy. The static disorder leads to the re-emitted radiation being a convolution between source linewidth and hyperfine field distribution[32, 33].

119
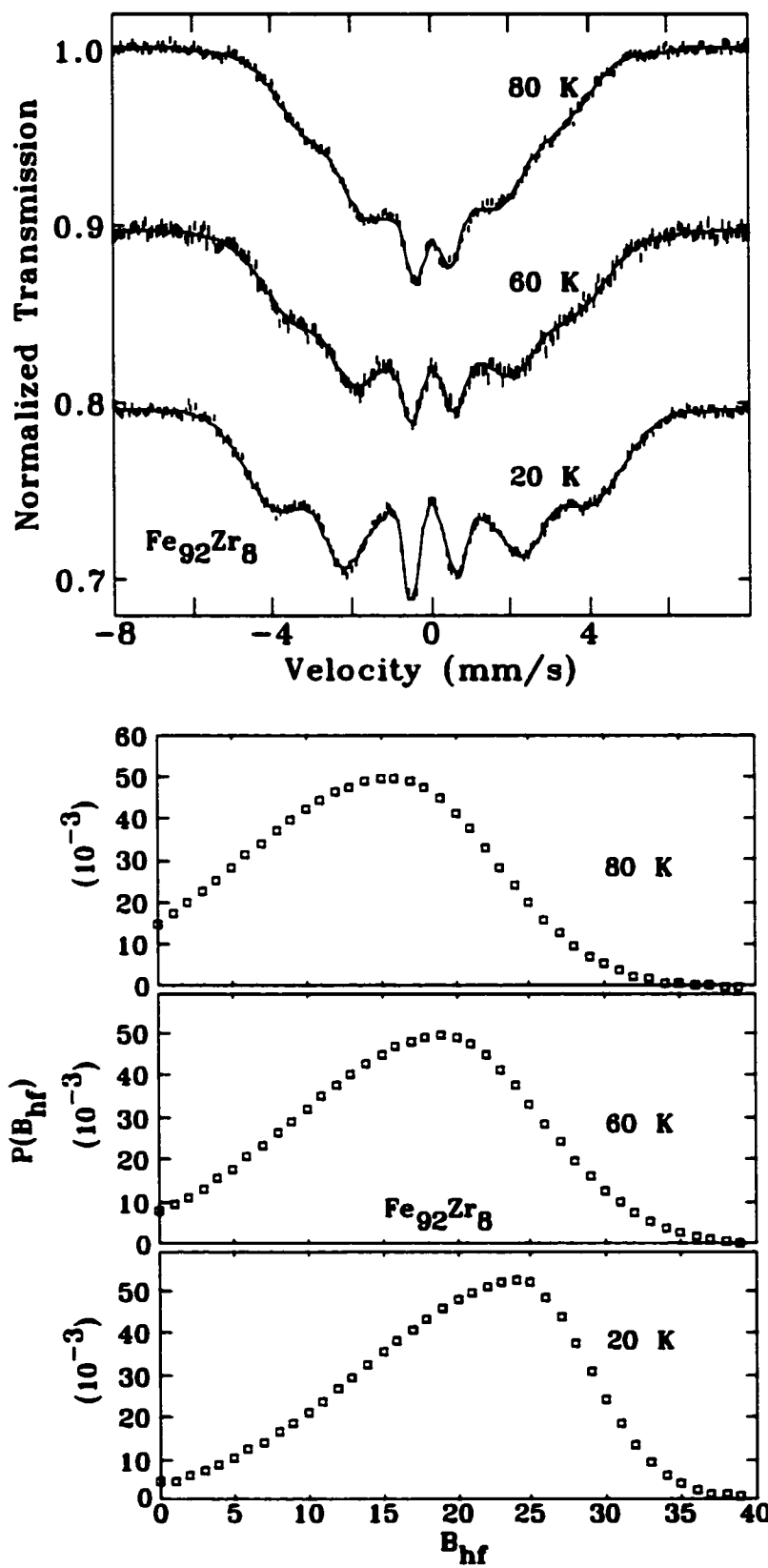
Figure 4.28: Transmission spectra of $Fe_{92}Zr_8$ fit using an asymmetric Gaussian $P(B_{hf})$ hyperfine field distribution.

120

0.2
0.0
100 K

0.2
0.0
90 K

0.2
0.0
80 K

0.2
0.0
70 K

0.2
0.0
60 K

0.2
0.0
20 K

Normalized Emission

−6   −4   −2   0   2   4

Velocity (mm/s)
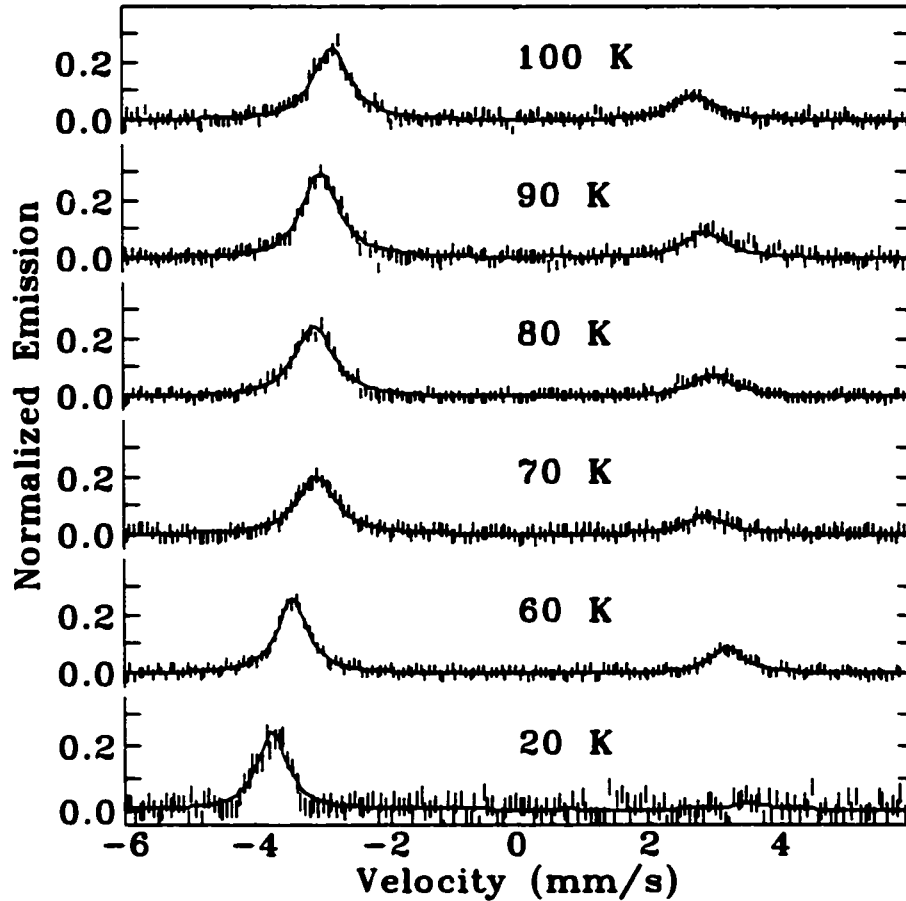
Figure 4.29: SEDM spectra of $Fe_{92}Zr_8$. At each temperature the pump energy was centered on the line at the left. The appearance of the peak at positive velocities indicates the onset of moment reversals.

This is entirely consistent with our SEDM measurements of a-$Fe_{80}B_{20}$ and $Fe_{65}Ni_{35}$ that were correctly described with a $P(B_{hf})$ measured from transmission Mössbauer spectra. At 20 K, the SEDM spectrum shows no indications of magnetic relaxation, and is properly fit using Eqn. 3.16 with $P(B_{hf})$ from the transmission Mössbauer fits (Fig. 4.28). SEDM is not sensitive to dynamic magnetic effects at 20 K, unlike ZF-μSR that measures a small relaxation rate for a-$Fe_{92}Zr_8$ (Fig. 4.25) at 20 K due to the muon's wider range of measuring times (Fig. 1.8).

At 60 K, where moment fluctuations from transverse spin freezing are indicated in the ZF-μSR results (Fig. 4.25), onset of magnetic fluctuations clearly impacts the SEDM spectra (Fig. 4.29). A new line at $\sim$ +3 mm/s is clearly present at 60 K.

121
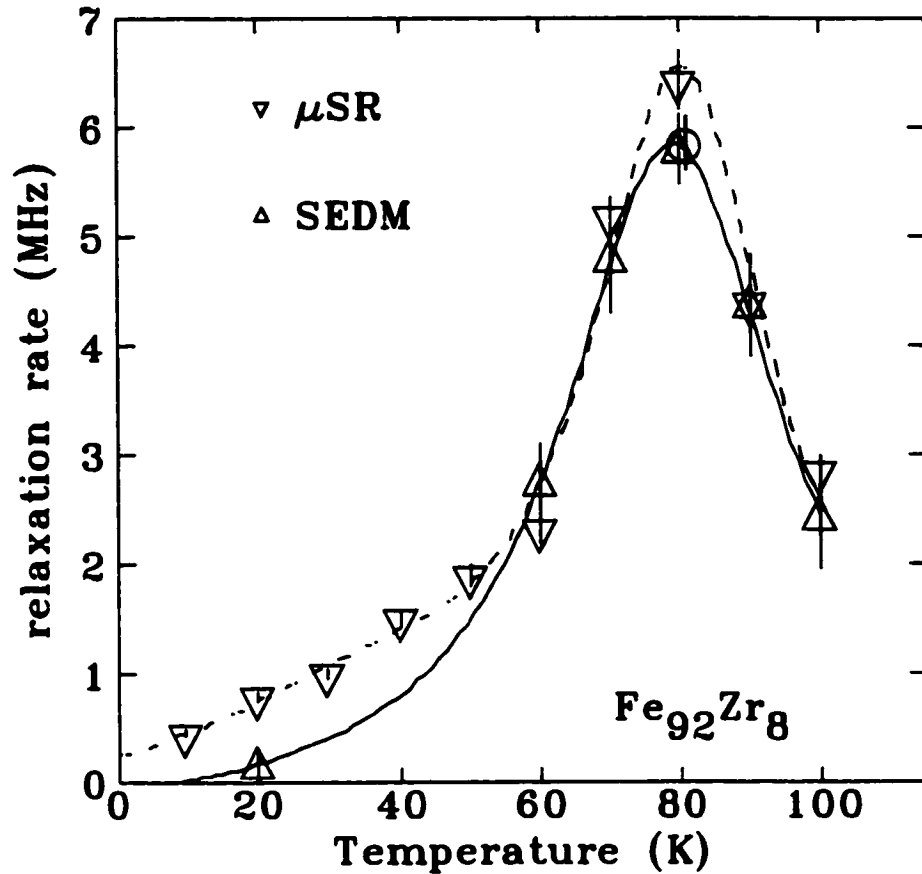
Figure 4.30: Results of fits to the data using a SEDM model that incorporates both magnetic relaxation effects and a distribution of hyperfine fields from static disorder. Relaxation rates show the sample fluctuation peak associated with T_{xy} as μSR data. Solid line shows the Gaussian trend of the SEDM relaxation rate with temperature while the dashed line shows similar Gaussian behavior of the fluctuation rate with temperature measured by μSR. SEDM data driving line #1 denoted by $\triangle$ and driving line #2 data by $\bigcirc$.

This line is due to the $m_e = +\frac{3}{2} \rightarrow m_g = +\frac{1}{2}$ transition, even though only the $m_e = -\frac{3}{2}$ excited state was populated. The angular momentum vector describing the precession of the Mössbauer nucleus in it's initially populated $m_e = -\frac{3}{2}$ excited state changes sign during the Larmor precession of the nucleus and decays via the $m_e = +\frac{3}{2} \rightarrow m_g = +\frac{1}{2}$ transition. This transition results in line #6 at $\sim +3$ mm/s. No amount of *static* disorder can lead to the appearance of the additional line (line #6). The appearance of the additional line is in perfect agreement with the SEDM results of the Fe_3O_4 ferrofluids, where moment flips from superparamagnetic relax-

ation was identified by the appearance of the new line. The relative linewidths and intensities of lines #1 and #6 are, for the a-$Fe_{92}Zr_8$, a measure of the convolution of the probability of a moment reversal and the distribution of hyperfine fields. This is a new condition for SEDM relaxation measurements, as magnetism in the Fe_3O_4 ferrofluids were completely dynamic in nature.

We are able to fit the a-$Fe_{92}Zr_8$ SEDM spectra by using the model described by Eqn. 3.21. The distribution of hyperfine fields ($P(B_{hf})$), due to the collinear mag-
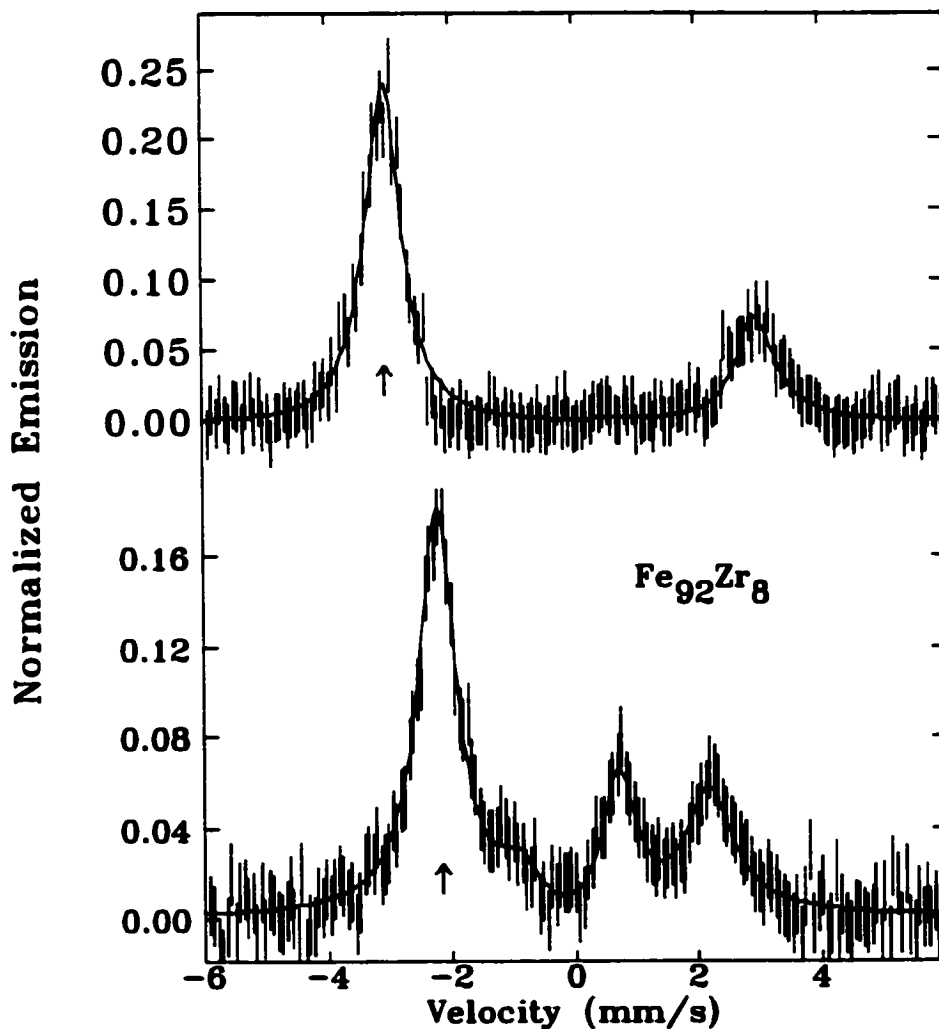
Figure 4.31: SEDM spectra of the $Fe_{92}Zr_8$ sample at 80 K when line #1 is pumped (top) and line #2 is pumped (bottom). Pump energies denoted by ↑.

netic order established at temperatures below T_C, is measured from the transmission Mössbauer spectra (Fig. 4.28). Combined with this $P(B_{hf})$, a two-level magnetic relaxation model characterized the SEDM spectra. Results of fits to the data are shown in Fig. 4.30. With the source radiation and detector linewidth characterized (Sec. 2.2), fitted linewidths of 0.10±0.01 mm/s are consistent with the lifetime of the excited state of the Mössbauer nucleus. Relaxation rates are in excellent agreement with fluctuation rates determined from μSR measurements[23] and display the same peak due to transverse spin freezing as T_{xy} is approached and then passed in temperature.

Further confirmation of 180° moment flips due to the transverse spin freezing is possible by examining another transition is the a-Fe$_{92}$Zr$_8$ sample. With the next largest nuclear cross-section, driving the line #2 transition ($m_g = -\frac{1}{2} \to m_e = -\frac{1}{2}$) offers the best possible signal for the collection time. In a static magnetic field, pumping a Mössbauer nucleus into the $m_e = -\frac{1}{2}$ excited state results in a decay into the $m_g = -\frac{1}{2}$ and $m_g = +\frac{1}{2}$ ground states: lines #2 and #4 appear in a SEDM spectrum when line #2 has been driven. This situation has been measured in α-Fe (Fig. 2.18) and a-Fe$_{80}$B$_{20}$ (Fig. 4.2). Examining the SEDM spectrum of a-Fe$_{92}$Zr$_8$ in Fig. 4.31 when line #2 is driven, we see that lines #2 and #4 appear. However, from moment flips, lines #3 and #5 show as well. A reversal of the magnetization direction during the $m_e = -\frac{1}{2}$ excited state populates the $m_e = +\frac{1}{2}$ excited state, and decays into the $m_g = +\frac{1}{2}$ and $m_g = -\frac{1}{2}$ ground states. The fitted relaxation rate of this SEDM spectrum is in excellent agreement with the ZF-μSR and previous SEDM results.

ZF-μSR has provided clear evidence of two magnetic transitions in iron-rich a-Fe-Zr alloys. These two transitions are observed in both the dynamic (λ) and static (Δ) behavior of the muon depolarization. Results are in perfect agreement with the description of the ordering in terms of a ferromagnetic phase transition followed by transverse spin freezing and the moment fluctuation peak predicted by numerical simulations at T_{xy} has been observed. These SEDM results on the a-Fe$_{92}$Zr$_8$ system

124

provide clear evidence of the ability of SEDM to explicitly separate static and dynamic magnetic effects. The ZF-μSR results indicated the existence of both types of disorder, and SEDM spectra are completely characterized by a model which incorporates the static disorder with a $P(B_{hf})$ measured from transmission Mössbauer spectra and a two-level relaxation model. Our SEDM results are in excellent agreement with the ZF-μSR data. The SEDM spectra track the fluctuation rate temperature dependence measured with ZF-μSR. Additionally, for the first time, the effects of transverse spin freezing on the moments have been explicitly measured: transverse spin freezing causes moments to undergo 180° flips. A possible origin could be that transverse spin fluctuations create an effective RF-magnetic field which causes the moment reversals[89]. Furthermore, the SEDM data on a-$Fe_{92}Zr_8$ provides more evidence that magnetic relaxation, if present, would have been detected with SEDM in the chemically disordered $Fe_{65}Ni_{35}$ alloy since transmission Mössbauer spectra of both materials are well described with a distribution of hyperfine fields.

Chapter 5

Conclusions

The zero-field experimental techniques of transmission Mössbauer, selective excitation double Mössbauer, and muon spin relaxation spectroscopy, have been used to distinguish the effects of static and dynamic magnetic disorder. The spectral signatures from static disorder, dynamic disorder, and both forms of magnetic disorder have been established using these different techniques. Comparisons between these experimental methods that have different time-sensitivities has provided a consistent picture of the magnetism. The following are the primary achievements:

- We have constructed a selective excitation double Mössbauer (SEDM) spectrometer using standard transmission Mössbauer equipment and a vibration-free, drive mounted conversion electron detector (CED). The instrument provides easy tuning to the excitation energy of a nuclear sublevel in a sample for the constant velocity drive. Radiation shielding and collimation are of simple construction and have been readily customized for different experimental conditions. The SEDM equipment has performed flawlessly for month-long runs, establishing its long-term stability. A 1000-[16] to 5000-fold[17] improvement in effective counting time when compared to previous experimental configurations means that SEDM need no longer be a fringe technique.

- SEDM spectroscopy has been used to distinguish static and dynamic contribution to the spectral broadening observed in transmission Mössbauer spectra.

126

- Measurements of a-$Fe_{80}B_{20}$ provide a clear example of the effects of static disorder on transmission and SEDM spectra.

- An inhomogeneous distribution of hyperfine fields yields an accurate description of both a-$Fe_{80}B_{20}$ transmission and SEDM spectra.

- The influence of chemical broadening in $Fe_{65}Ni_{35}$ can be easily detected with SEDM spectroscopy, and is fully consistent with transmission data.

- SEDM spectra of $Fe_{65}Ni_{35}$ provide the first conclusive evidence that chemical disorder is responsible for the line shapes of transmission spectra on Fe-Ni Invar alloys.

- Comparison of static and dynamic fits to both transmission and SEDM spectra of $Fe_{65}Ni_{35}$ at temperatures up to $0.99T_C$ allow us to rule out relaxation as a significant source of spectral broadening in this system.

- Any time-dependent effects in $Fe_{65}Ni_{35}$ which may be present are slower than 0 ± 0.1 MHz and make a negligible contribution to the spectral form. These results rule out any possible magnetic relaxation at temperatures up to and including those where relaxation is most likely to occur, at T_C. This description is fully consistent with previous interpretations of Fe-Ni Invar transmission spectra in terms of chemical disorder alone.

- A model of magnetic single-domain fine particle systems has been developed that correctly predicts the behavior of transmission Mössbauer spectra over the complete range of temperatures.

  - Applying this model to two ferrofluids and a polysaccharide iron complex, we are able to extract consistent values of K (in the expected range of 10^4 J/m^3), determine the moment rotation rates from angles in the interval of $0°$ to $180°$ (allowing us to compare our results with those of simpler two-level models and collective excitations) and assess the blocking temperature, T_B.

– Analysis of the transmission Mössbauer spectra is in agreement with χ_{ac} (T_B) and SEDM (ν) results. For temperatures higher than T_B, relaxation rates used to describe the spectra fall in the typical time region of $\tau = 10^{-8} - 10^{-9}$ s.

– The trends exhibited for T_B, K, ν_0 and ν due to interparticle interactions and differing particle sizes and surroundings are in agreement with previous experimental and theoretical work. Specifically, we have measured a decreased K, T_B and ν_0, as well as an increased 180° moment flip rate (ν), in an aged Fe_3O_4 ferrofluid due to an increase in interparticle interactions.

• Substantial improvements to SEDM methodology have allowed us to characterize the defining magnetic phenomena of a fine particle system.

– At the lowest temperatures, moments are frozen along their easy axes and the material is easily described by a distribution of static magnetic fields from, for example, chemical disorder and dipole interactions.

– Collective excitations appear at higher temperatures and lead to significant temperature-dependent line broadening, which exceeds that predicted by a static hyperfine field distribution.

– Clear evidence of moments undergoing a transition from collective excitations to superparamagnetism is given by the SEDM spectra. The additional line is the first unequivocal evidence that moments are undergoing simple 180° spin flips and that no other moment orientation process is responsible for the superparamagnetic behavior of these particles. Furthermore, the sharp lines indicate that the reversal is abrupt.

– Relaxation frequencies exhibit a gradual increase with temperature and are in agreement with those used in our multi-level transmission Mössbauer spectra model.

– Relaxation rates were measured directly without appealing to models of magnetic excitations (for the first time), and are not influenced by particle

size distributions.

- Zero-field muon spin relaxation has been used to examine a magnetic fine particle system.

  - Static moments, collective excitations and superparamagnetic relaxation rates have been clearly distinguished in the presence of a distribution of particle sizes.

  - The first direct measurement of collective excitation has indicated that the fluctuation frequency is consistent with Mørup's model.

  - The blocking temperature extrapolated from the ZF-μSR results is in excellent agreement with transmission Mössbauer fit results and χ_{ac} data. Superparamagnetic relaxation rates are in agreement with those used in our multi-level transmission Mössbauer spectra model, confirming the validity of this description.

- Muon spin relaxation provides clear evidence of two, and only two, magnetic transitions in iron-rich a-Fe-Zr alloys.

  - The two transitions are observed in both the dynamic and static behavior of the muon polarization decay.

  - The results are in perfect agreement with the description of the ordering in terms of a ferromagnetic phase transition followed by transverse spin freezing.

  - We have confirmed the peak in the fluctuations at T_{xy} predicted by numerical simulations.

- SEDM spectra of $Fe_{92}Zr_8$ have been collected at temperatures where the second fluctuation peak at T_{xy} was observed with μSR.

  - SEDM fluctuation rates are in excellent agreement with μSR data.

- The fluctuations associated with transverse spin freezing around T_{xy} cause moments to undergo a 180° change in their magnetization direction.

- The SEDM lineshape description that incorporates static ferromagnetic disorder (established from transmission Mössbauer spectra fits) with dynamic moment behavior properly describes the SEDM spectra.

- The a-Fe-Zr and Fe-Ni alloys are both disordered alloys, and the SEDM results on $Fe_{92}Zr_8$ is further evidence that magnetic relaxation in the $Fe_{65}Ni_{35}$ system, if present, would have been explicitly measured with SEDM.

Directions for future work

As is usually the case during the course of scientific investigation, many questions arose which would further advance understanding of the experimental methods used and systems studied. In the following, we offer a short list of possible projects:

- Examine the so-called quantum tunneling of magnetization in ferritin[90] and the macromolecule Fe_8[91] with SEDM. In these systems, at low temperatures (below 1 K) resonant quantum tunneling of the magnetization occurs, resulting in a 180° moment flip. This moment flip is supposed to occur at temperatures well below which superparamagnetism can happen. With the same spectral signature as shown by the Fe_3O_4 ferrofluid at high temperatures, SEDM would unambiguously measure the existence of these moment flips at these very low temperatures.

- A radio-frequency SEDM spectrometer should be constructed. This would allow transitions between nuclear levels (like a nuclear magnetic resonance experiment) to occur with known frequency in a sample which would normally exhibit a static magnetic environment (e.g. α-Fe).

- Use applied-field SEDM to study the effects of an external field on the relaxation rates and line intensities of SEDM spectra. A Fe_3O_4 ferrofluid would be an ideal

sample. The effects of biasing the effective potential well that the moments reside in could be directly measured. Both zero-field cooled and field cooled experiments should be done.

- Use transmission Mössbauer spectroscopy to examine ferrofluids with different concentrations and determine how weaker and stronger interparticle interactions change T_B, K and ν.

- Study magnetic fine particle systems with different particle size distributions in an attempt to decouple the particle interactions effects from the distribution. Design a fine particle system which has a single effective particle size. Establish how T_B, K and ν are affected.

- Examine patterned thin-films with conversion electron Mössbauer spectroscopy and μSR. These films would have a single moment size (e.g. patterned iron pillars on a substrate) and the superparamagnetism could be examined as a function of particle interactions (e.g. different pillar separations and geometries).

- Map out the complete phase diagram of a-Fe_xZr_{100-x} with longitudinal field μSR so as to determined the field dependence of T_{xy}. For example, the applied-field transmission Mössbauer work on a-Fe_xZr_{100-x}[22] shows a T_{xy} transition for $Fe_{93}Zr_7$ which is not seen with ZF-μSR.

- Continue the Monte Carlo work describing the moment fluctuation behavior of a frustrated Heisenberg ferromagnet for applied fields.

Bibliography

[1] S. Mørup, J. Magn. Magn. Mater. **37**, 39 (1983).

[2] M. Blume and J.A. Tjon, Phys. Rev. **165**, 446 (1968).

[3] E. Tronc, P. Prené, J.P. Jolivet, F. D'Orazio, F. Lucari, D. Fiorani, M. Godinho, R. Cherkaoui, M. Nogues. J.L. Dormann, Hyperfine Interact. **95**, 129 (1995).

[4] J.L. Dormann, D. Fiorani and E. Tronc, in "*Advances in Chemical Physics*", **XCVIII**, eds. I. Prigogine and Stuart A. Rice (John Wiley & Sons, Inc.), 283 (1997).

[5] F. Bødker, M. Hansen, C.B. Koch, K. Lefmann and S. Mørup, Phys. Rev. B, **61**, 6826 (2000).

[6] B. Ganguly, F.E. Huggins, K.R.P.M. Rao, G.P. Huffman, J. Catalysis **142**, 552 (1993).

[7] N.M.K. Reid, D.P.E. Dickson, D.H. Jones, Hyperfine Interact. **56**, 1487 (1990).

[8] A. Tari, J. Popplewell, S.W. Charles, D. St.P. Bunbruy, K.M. Alves, J. Appl. Phys. **54**, 3351 (1983).

[9] Y. Nakamura, IEEE Transaction on Magnetics, **12**, No.4, 278 (1976).

[10] C.E. Guillaume, Compt. Rend., **125**, 235 (1897).

[11] Jürgen Hesse and Eckhard Hagen, Hyperfine Interact. **28**, 475 (1986).

[12] M.R. Gallas and J. A. H. da Jornada, J. Phys.: Condens. Matter **3**, 155 (1991).

[13] H.R. Rechenberg, Hyperfine Interact. **54**, 683 (1990).

[14] D.G. Rancourt, H.H.A. Smit and R.C. Thiel, J. Magn. Magn. Mater. **66**, 121 (1987).

[15] A.N. Artem'ev, G.V. Smirnov and E.P. Stepanov, Soviet Physics JETP **27**, 547 (1968).

[16] Neil D. Heiman and J.C. Walker, Phys. Rev. **184**, 281 (1969).

[17] Bohdan Balko and Gilbert R. Hoy, Phys. Rev. B **10**, 36 (1974).

[18] J.J. Bara, Phys. Stat. Sol. A **63**, 119 (1981).

[19] J. van Lierop and D.H. Ryan, submitted to Review of Scientific Instruments.

[20] D.H. Ryan in *Recent Progress in Random Magnets* edited by D.H. Ryan, (World Scientific Publishers, Singapore, 1992).

[21] J.R. Thomson, Hong Guo, D.H. Ryan, M.J. Zuckermann and Martin Grant, Phys. Rev. B., **45**, 3129 (1992).

[22] Hong Ren and D.H. Ryan, Phys. Rev. B, **51**, 15 886 (1995).

[23] D.H. Ryan, J.M. Cadogan and J. van Lierop, Phys. Rev. B., **61**, 6816 (2000).

[24] N.N. Greenwood and T.C. Gibb in *Mössbauer Spectroscopy*, Chapman and Hall Ltd, London, 1971.

[25] P. Gütlich, L. Rainer and A. Trautwein in *Mössbauer Spectrosopy and Transition Metal Chemistry*, Springer-Verlag, Berlin, 1978.

133

[26] Wissenschaftliche Elektronic GMBH, Pilotystr 3 D-8130 Starnberg, West Germany.

[27] Reuter-Stokes, P.O. Box 10901, Pittsburgh, PA 15236.

[28] EG&G ORTEC, 100 Midland Road, Oak Ridge, TN 37830.

[29] Canberra Industries, Inc., One State Street, Meriden, CT 06450.

[30] S. Bocquet, R.J. Pollard and J.D. Cashion, Hyp. Int. **58**, 2503 (1990).

[31] D.C. Price and A.M. Stewart, Hyp. Int. **42**, 1157 (1988).

[32] J. van Lierop and D.H. Ryan, J. Appl. Phys. **85**, 4518 (1999).

[33] J. van Lierop and D.H. Ryan, Phys. Rev. Lett. **85**, 3021 (2000).

[34] Ferrofluidics Corporation, 40 Simon Street Nashua, N.H., U.S.A., 03061.

[35] V.G. Semenov, S.M. Irkaev, Y.N. Maltsev, Nucl. Instrum. Meth. Phys. Res. B, **95**, 253 (1995).

[36] J.G. Mullen and J. Stevenson, Nuclear Instum. and Meth. **153**, 77 (1978).

[37] L.X. Liao, D.H. Ryan, Z. Altounian, Rev. Sci. Instrum., **64**, 679 (1993).

[38] J.J. Spijkerman, Mössbauer Effect Methodology, **7**, 85 (1971).

[39] A.P. Kuprin and A.A. Novakova, Nucl. Instrum. Meth. Phys. Res. B., **62**, 493 (1992).

[40] Supplied by NEN/DuPont, North Billerica, MA. Cat. No. NER-512.

[41] E.B. Karlsson in *Solid State Phenomena*, Clarendon Press, Oxford, 1995.

[42] P. Dalmas de Réotier and A. Yaouanc, J. Phys.: Condens. Matter **9**, 9113-9166 (1997).

[43] W. Künidg, Nucl. Instr. and Meth., **48**, 219 (1967).

134

[44] B. Window, J. Phys. E4, 401 (1971).

[45] L. Cianchi, P. Moretti, M. Mancini and G. Spine, Rep. Prog. Phys. **49**, 1243 (1986).

[46] M.F. Hansen, S. Mørup, J. Mag. Mag. Mat. **184**, 262 (1998).

[47] D.H. Jones, K.K.P. Srivastava, Phys. Rev. B **34**, 7542 (1986).

[48] W.T. Coffey, P.J. Cregg, D.S.F. Crothers, J.T. Waldron, A.W. Wickstead, J. Magn. Magn. Mater. **131**, L301 (1994).

[49] Schwarz Pharma, Inc. Milwaukee, W.I., U.S.A., 53201.

[50] D.H. Jones, K.K.P. Srivastava, J. Magn. Magn. Mater. **78**, 320 (1989).

[51] D.B. Lambrick, S.R. Hoon, N. Mason, M. Kilner, IEEE Transactions of Magnetics, **24**, no. 2, pt. 2., 1647 (1988).

[52] N.Y. Ayoub, R.Y. Abdelal, R.W. Chantrell, J. Popplewell, K. O'Grady, J. Magn. Magn. Mater. **79**, 81 (1989).

[53] C. Johansson, M. Hanson, M.S. Pedersen. S. Mørup, J. Magn. Magn. Mater., **173**, 5 (1997).

[54] R.A. Sack, Molec. Phys. **1**, 163 (1958).

[55] P.W. Anderson, J. Phys. Soc. Japan **9**, 316 (1954).

[56] Bohdan Balko, Phys. Rev. B **33**, 7421 (1986).

[57] C.G. Granqvist and R.A. Buhrman, J. Appl. Phys. **47**, 2200 (1976).

[58] M-E. Y. Mohie-Eldin, R.B. Frankel, L. Gunther and G.C. Papaefthymiou, Hyperfine Interact., **96**, 111 (1995).

[59] J. van Lierop and D.H. Ryan, J. Appl. Phys. **87**, 6277 (2000).

[60] J.L. Dormann, F. D'Orazio, F. Lucari, E. Tronc, P. Prené, J.P. Jolivet, D. Fiorani, R. Cherkaoui and M. Noguès, Phys. Rev. B., **53**, 14291 (1996).

[61] J.-O. Andersson, C. Djurbert, T. Jonsson, P. Svedlindh and P. Nordblad, Phys. Rev. B., **56**, 13983 (1997).

[62] M.J. Clauser and M. Blume, Phys. Rev. B., **3**, 583 (1971).

[63] M. Blanco-Mantecón and K. O'Grady, J. Magn. Magn. Mater. **203**, 50 (1999).

[64] W.T. Coffey, D.S.F. Crothers, Yu. P. Kalmykov, E.S. Massawe and J.T. Waldron, Phys. Rev. E, **49**, 1869 (1994).

[65] J.L. Dormann, L. Spinu, E. Tronc, J.P. Jolivet, F. Lucari, F. D'Orazio and D. Fiorani, J. Magn. Magn. Mater. **183**, L255 (1998).

[66] T. Jonsson, P. Nordblad and P. Svedlindh, Phys. Rev. B, **57**, 497 (1998).

[67] A. Paupolis in *Probability, Random Variables, and Stochastic Processes*, McGraw-Hill, New York, 1965.

[68] R. Kubo and T. Toyabe, *Magnetic Resonance and Relaxation*, edited by R. Blinck, North-Holland, Amsterdam, p.810 (1967).

[69] R.S. Hayano, Y.J. Uemura, J. Imazato, N. Nishida, T. Yamazaki and R. Kubo, Phys. Rev. B, **20**, 850 (1979).

[70] R. Kubo, J. Phys. Soc. Jpn. **9**, 935 (1954).

[71] B. Davies and B. Martin, J. Comp. Phys., **33**, 1 (1979).

[72] W. T. Weeks, J. Assoc. Comp. Mach., **13**, 419 (1966).

[73] G.B. Rybicki, Computers in Physics, Mar/Apr, 85 (1989).

[74] Y.J. Uemura, Solid State Comm. **36**, 369 (1980).

[75] R. Kubo, Hyperfine Interact., **8**, 731 (1981).

[76] D.R. Noakes, J.H. Brewer, D.R. Harshman, E.J. Ansaldo, C.Y. Huang, Phys. Rev. B., **35**, 6597 (1987).

[77] E.F. Wassermann, in "*Ferromagnetic Materials*", **V**, eds. K.H.J. Buschow and E.P. Wohlfarth (North-Holland, Amsterdam), 240 (1990).

[78] Schwarz Pharma Inc., Milwaukee WI, 53201, U.S.A.

[79] R. Kubo and T. Toyabe, in *Magnetic Resonance and Relaxation* edited by R. Blinc, (North-Holland, Amsterdam, 1967), p. 810.

[80] S.F.J. Cox in *Muon Science* edited by S.L. Lee, S.H. Kilcoyne and R. Cywinski, (Scottish Universities Summer School in Physics & Institute of Physics Publishing, Bristol and Philadelphia, 1999), p.265.

[81] J. van Lierop and D.H. Ryan, J. Appl. Phys. **87**, 6277 (2000).

[82] J. van Lierop and D.H. Ryan, accepted by Phys. Rev. B.

[83] J. van Lierop, D.H. Ryan, M.E. Pumarol and M. Roseman, confernece paper for the 8th joint MMM-Intermag Conference. San Antonio, Texas, Jan. 7-11, 2001.

[84] D.G. Rancourt and J.Y. Ping, Nuclear Instruments and Meth., **B58**, 85 (1991).

[85] H.Ma, H.P. Kunkel, G. Williams and D.H. Ryan, J. Appl. Phys., **67**, 5964 (1990).

[86] D.H. Ryan, J.M. Cadogan and S.J. Kennedy, J. Appl. Phys, **79**, 6161 (1996).

[87] D.H. Ryan, Zin Tun and J.M Cadogan, J. Magn. Magn. Mater. **177-81**, 57 (1998).

[88] D.H. Ryan, J. van Lierop, M. Pumarol and M. Roseman, submitted to Physical Review Letters.

[89] M. Munowith and A. Pines, Science, **233**, 525 (1986).

[90] Tjeda et al., Phys. Rev. Lett., **79**, 1754 (1997).

[91] W. Wernsdorfer, A. Caneschi, R. Sessoli, D. Gatteschi, A. Corina, V. Villar and C. Paulsen, Phys. Rev. Lett. **84**, 2965 (2000).

[92] Jess H. Brewer in *Encyclopedia of Applied Physics*, **11**, 23 (VCH Publishers, Inc., 1994).